UNIVERSITY OF CALGARY

Interpretive PP and PS Joint Inversion

by

Hongbo Zhang

A THESIS SUBMITTED TO THE FACULTY OF GRADUATE

STUDIES IN PARTIAL FULFILMENT OF THE REQUIREMENTS

FOR THE DEGREE OF MASTER OF SCIENCE

DEPARTMENT OF GEOLOGY AND GEOPHYSICS

CALGARY, ALBERTA

JUNE, 2003

UNIVERSITY OF CALGARY

FACULTY OF GRADUATE STUDIES

The undersigned certify that they have read, and recommend to the Faculty of Graduate Studies for acceptance, a thesis entitled "Interpretive PP and PS Joint Inversion" submitted by Hongbo Zhang in partial fulfillment of the requirements for the degree of Master of Science.

Gary F. Margrave

Supervisor, Dr. Gary F. Margrave,
Department of Geology and Geophysics

R.J. Brown

Co-Supervisor, Dr. R. James Brown,
Department of Geology and Geophysics

L.R. Lines

Dr. Laurence R. Lines,
Department of Geology and Geophysics

L. Bos

Dr. Len Bos,
Department of Mathematics and Statistics

July 25, 2003

ABSTRACT

The method of joint PP-PS inversion has recently been developed and tested on the 3-D Blackfoot seismic data set. This thesis shows the application of this method on 3C-2D seismic data from Pikes Peak oil field. The inversion was accomplished with a newly installed inversion module in ProMAX. Ten datasets that were carefully prestack processed, migrated and correlated, together with the RMS amplitude values and a background velocity model, were input into the joint PP-PS AVO inversion module in ProMAX. Four attributes were determined: fractional compressional-impedance contrast $\Delta I/I$, fractional shear-impedance contrast $\Delta J/J$, fractional $\lambda\rho$ contrast $\Delta(\lambda\rho)/\lambda\rho$ and fractional λ/μ contrast $\Delta(\lambda/\mu)/(\lambda/\mu)$.

Good correlation of these parameters from seismic inversion and those calculated from well logs shows that joint PP-PS AVO inversion can be used to indicate anomalous lithology and pore-fluid changes in the subsurface. Therefore it should be helpful in detecting hydrocarbons using 2-D multicomponent seismic data.

ACKNOWLEDGEMENTS

I would like to extend my deepest thanks and gratitude to my supervisor, Dr. Gary F. Margrave, and my co-supervisor, Dr. R. James Brown, for providing guidance and support throughout the course of this research. I wish to thank the CREWES Project sponsor companies and representatives for providing financial assistance and useful discussions regarding this research. Sincere thanks to Saskatchewan Energy and Mines for providing the well completion data in wells at Pikes Peak oil field. I wish to thank the CREWES Project directors, staff and students for their friendship, assistance and helpful insight into this research. Finally, I would like to extend my sincere gratitude to the following people: Dave Henley, Hanxing Lu, Colin Potter, and Steven Hinds, without whose help, this thesis wouldn't be as great!

TABLE OF CONTENTS

LIST OF FIGURES

LIST OF TABLES

CHAPTER 1

INTRODUCTION

1.1 Thesis organization

This thesis consists of five chapters. In chapter 1 certain detailed background material is introduced concerning elastic rock-property estimates and their link with lithology and pore-fluid content according to the changes in the amplitude versus offset (AVO). In detail, AVO is the amplitude variation with offset (Sheriff, 1991). Methods of estimating AVO effects using both P-wave and converted-wave seismic data have been greatly improved by scientists during the last 20 years. Chapter 2 introduces the derivation and the physical and mathematical bases of the joint PP-PS AVO inversion method that was developed by Stewart (1990), Larsen (1999) and Margrave et al. (2001). The brief implementation of this method on a 2-D dataset is also introduced.

In chapter 3, the important steps of preparing the 2-D seismic data for joint PP-PS AVO inversion are demonstrated. Each critical parameter for the joint inversion is derived in each step while possible problems and the corresponding solutions in each step are discussed. And in chapter 4, results of correlation between joint PP-PS AVO inversion and direct computation from well logs are shown. Comparison of joint inversion and P-wave-only inversion shows that the joint inversion is more powerful in extracting lithological and pore-fluid parameters from seismic data and more helpful in detecting hydrocarbons.

1.2 Introduction

On the basis of the profound development of P-wave exploration, the potential benefit of incorporating multicomponent seismic data has been more and more widely recognized. This emerging idea has set a new trend in the petroleum exploration industry and has been one of the important subjects of conferences and workshops throughout the world since the mid-1980s. The primary goal of this study is to apply the joint PP-PS AVO inversion method to a 2-D three-component seismic dataset so that its applicability and sensitivity on multicomponent seismic data can be tested. The results of this study will also show what advantages there are in performing PP and PS AVO analysis jointly over performing them separately.

1.2.1 Background

As we know, P-wave velocity (V_P or α), S-wave velocity (V_S or β) and density (ρ) can be used to describe the lithology and pore-fluid properties in a given rock. Koefoed (1955) first pointed out the practical possibilities of using amplitude-variation-with-offset (AVO) analysis as an indicator of V_P/V_S variations. Pickett (1963) found that variation in V_P/V_S could differentiate sandstones, limestones and dolomites. Domenico (1977) further observed that V_P and V_S were higher for clean sandstones than shaly sandstones. Further developing the relationship between lithology and Poisson's ratio introduced by Koefoed (1955) and the Aki and Richards (1980) approximation of the Zoeppritz equations, Shuey (1985) further linearized the Zoeppritz equations. The coefficients of Shuey's approximation form the basis of AVO measurement and various weighted stacking procedures. At about the same time, the "fluid factor" concept was introduced by Smith and Gidlow (1987) to highlight gas-bearing sandstones. Hilterman (1989) derived another convenient approximation in which one could think of a near-offset stack as imaging P-wave impedance contrasts, and the far-offset stack as imaging Poisson's-ratio contrasts.

The development of AVO analysis has encouraged the need for true-amplitude seismic processing. According to Castagna and Backus (1993), when attempting to select an appropriate data processing scheme for AVO analysis, the processor must carefully balance two competing objectives: (1) noise suppression and isolation of the reflectivity of the event of interest, and (2) not biasing or otherwise corrupting the reflectivity variation with offset. This tradeoff usually leads to the selection of a basic but robust processing scheme (for example, Ostrander, 1984; Chiburis, 1984). Ferre et al. (1999)

improved the intercept and gradient computation in the presence of noise and outlier contamination. This approach leads to a global improvement of the standard AVO methodology. A new approach to improving AVO analysis in the presence of dip is demonstrated by Ramos et al. (1999). This approach is called true-amplitude DMO (dip moveout). The main advantage of true-amplitude DMO compared to more traditional methods lies in its ability to perform a better compensation of geometrical-spreading losses with offset.

Of primary importance to the goal of true-amplitude recovery is the use of true-amplitude seismic migration. Gray (1997) pointed out that the interpretation of AVO using unmigrated records was commonly hindered by the effects of CDP (common-depth-point) smear, incorrectly specified geometrical spreading loss, source-receiver directivity, as well as other factors. Thus, it is possible to correct some of these problems by analyzing common-reflection-point gathers after careful prestack migration; and a true-amplitude migration should be a method of removing amplitude and phase distortions to produce angle-dependent reflection coefficients in a lossless and elastic earth model. Other authors such as Schneider and Krey (1985), and Krajewski et al. (1993) have also discussed true-amplitude migration methods.

By far, gas-sand detection is the most promising application of AVO analysis. The characteristically low V_P/V_S of gas sands should allow their differentiation from other low-impedance layers, such as coals and porous brine sands (Castagna and Backus, 1993). Rutherford and Williams (1989) defined three distinct classes of gas-sand AVO anomalies. Wright (1986), Thomsen (1990) and Castagna and Backus (1993) also noticed that the rigidity modulus, μ, provides more physical insight. Fatti et al. (1994) employed a technique called Geostack (Smith and Gidlow, 1987) in the detection of gas in sandstone reservoirs. The fluid factor (Smith and Gidlow, 1987) is defined as:

$$\Delta F = R_P - 1.16 \frac{W}{V} R_S \tag{1.1}$$

where R_P = zero-offset P-wave reflection coefficient,

$W =$ average S-wave velocity,

V = average P-wave velocity,

R_S = zero-offset S-wave reflection coefficient.

Stewart et al. (1995) discussed the potential usefulness of the Lamé parameters (λ and μ) in better differentiating rock properties. And Goodway et al. (1997) applied this observation in their study and showed λ, μ and λ/μ were more sensitive to changes in rock properties than V_P, V_S and V_P/V_S.

1.2.2 P-wave AVO methods

Lithological evaluation first became viable in the 1960s with the development of multioffset recording in seismic acquisition. Early techniques of lithology evaluation utilized zero-offset and poststack inversion methods (Lindseth, 1979). These methods along with "bright-spot" analysis techniques gave a very simple model of the seismic response. Then Ostrander (1982) proposed a technique using prestack seismic amplitudes to extract information about lithology and pore fluids. Ostrander (1984) found that variations in Poisson's ratio have a strong connection with the nature of the variation in reflection coefficient with angle of incidence; and that analysis of seismic reflection amplitude versus offset can in many cases distinguish between gas-related amplitude anomalies and other types of amplitude anomalies. Shuey (1985) developed a gradient-intercept method that measured reflectivity at zero offset, intermediate offset and far offset. The initial model assumes no contrast in Poisson's ratio and thus a fixed V_P/V_S.

Smith and Gidlow (1987) developed a method to estimate fractional changes in compressional and shear velocities using least-squares inversion to apply a set of model-based weights in an offset-dependent manner. This method does not assume a fixed background V_P/V_S, but does need a smoothed background model independent of the estimates of the fractional parameters, each of which is a difference between the velocities of two layers divided by the average velocity of the same two layers. "Reconnaissance methods" (Hampson and Russell, 1990) include methods such as limited-offset stacking and gradient-intercept methods. Fatti et al. (1994) further improved upon the "Geostack" method (Smith and Gidlow, 1987) by incorporating density changes instead of using an empirical relationship between compressional velocity and density of Gardner et al. (1974).

Macdonald et al. (1987) and Russell (1988) discussed the generalized linear inversion method (GLI) and applied it to invert the Zoeppritz equations (Zoeppritz, 1919) directly. The GLI method does not rely upon approximations to the Zoeppritz equations. In general, P-wave AVO has been used in combining with GLI and varied rates of success have been achieved. Meanwhile, de Haas and Berkhout (1989), and Van Rijssen and Herman (1991) showed that the addition of multicomponent seismic data could significantly improve the estimates of elastic parameters.

1.2.3 Converted-wave seismology

When a compressional wave incident upon an interface at non-zero offset, it is partitioned into transmitted and reflected P and S waves. Ricker and Lynn (1950) were among the first to observe the potential benefits of converted-wave seismology. As a result of new developments in acquisition and processing technology, the use of converted-wave (P-S) data has increased in recent years. The use of P-S seismic data enhances confidence in the interpretation and rock property estimates by providing additional imaging constraints. What's more, due to the use of 3-component receivers, P-S seismic data can be obtained at relatively low cost. Waters (1992) suggested that significant converted-wave energy is available using standard acquisition techniques. Stewart and Lawton (1996) observed that the incorporated P-S seismic data provided another section with independent properties (e.g., velocity, multiples, tuning), helped to image interfaces with low P-wave reflectivity contrast (e.g., imaging through gas chimneys), assisted P-P interpretation via long wavelength V_P/V_S values and additional sections, augmented conventional AVO analysis, investigated anisotropy and fractures, and calibrated P-wave bright spots.

On the basis of a previous weighted-stacking method utilizing P-P seismic data only (Smith and Gidlow, 1987) and its extension by Stewart (1990), Larsen (1999) developed a method to simultaneously invert P-P and P-S pre-stack seismic data to extract estimates of compressional and shear impedance values. Initial results show there is a general improvement using both types of data: events appear more coherent and signal-to-noise appears to have increased.

1.3 Thesis objective

The goal of this thesis is to compute estimates of elastic parameters from the simultaneous inversion of 2-D P-P and P-S seismic data using the inversion method further developed by Larsen (1999). The author created the practical procedure of how to prepare the 2-D seismic data for this joint inversion and executed the joint inversion module in ProMAX for the first time. It is hoped that the joint inversion will improve the signal-to-noise ratio, and thus the accuracy of impedance inversion by incorporating a simultaneous inversion method rather than a P-P inversion method alone.

1.4 Data used

The preparation procedure for the simultaneous P-P and P-S AVO inversion and the execution of this method were evaluated using the following datasets.

1.4.1 Pikes Peak 3C-2D data

On March 1-2, 2000, the Consortium for Research in Elastic Wave Exploration Seismology (CREWES) at the University of Calgary, with financial assistance from AOSTRA and Husky Energy Inc., recorded a high-resolution 3C-2D seismic survey at the Husky-owned Pikes Peak heavy-oil field. The Pikes Peak field is located approximately 40 km east of the town of Lloydminter, Alberta/Saskatchewan as shown in figure 1.1.

The survey involved the acquisition of a 3.8-km 3C-2D reflection profile that consisted of a combination of conventional vertical-geophone arrays, single microphones and single 3-C geophones. The source interval employed was 20 m. However, the receiver interval used for the vertical-geophone arrays and single microphones was 20 m, whereas the single 3-C geophones used a 10-m receiver interval.

There were, in total, 191 source points which consisted of two 25,000-kg Hemi 44 vibrators spaced over 10 m. There were 4 sweeps per source point with no move-up between sweeps. A 16-s sweep consisting of two segments was used: 1) 0.375 s, 8-25 Hz

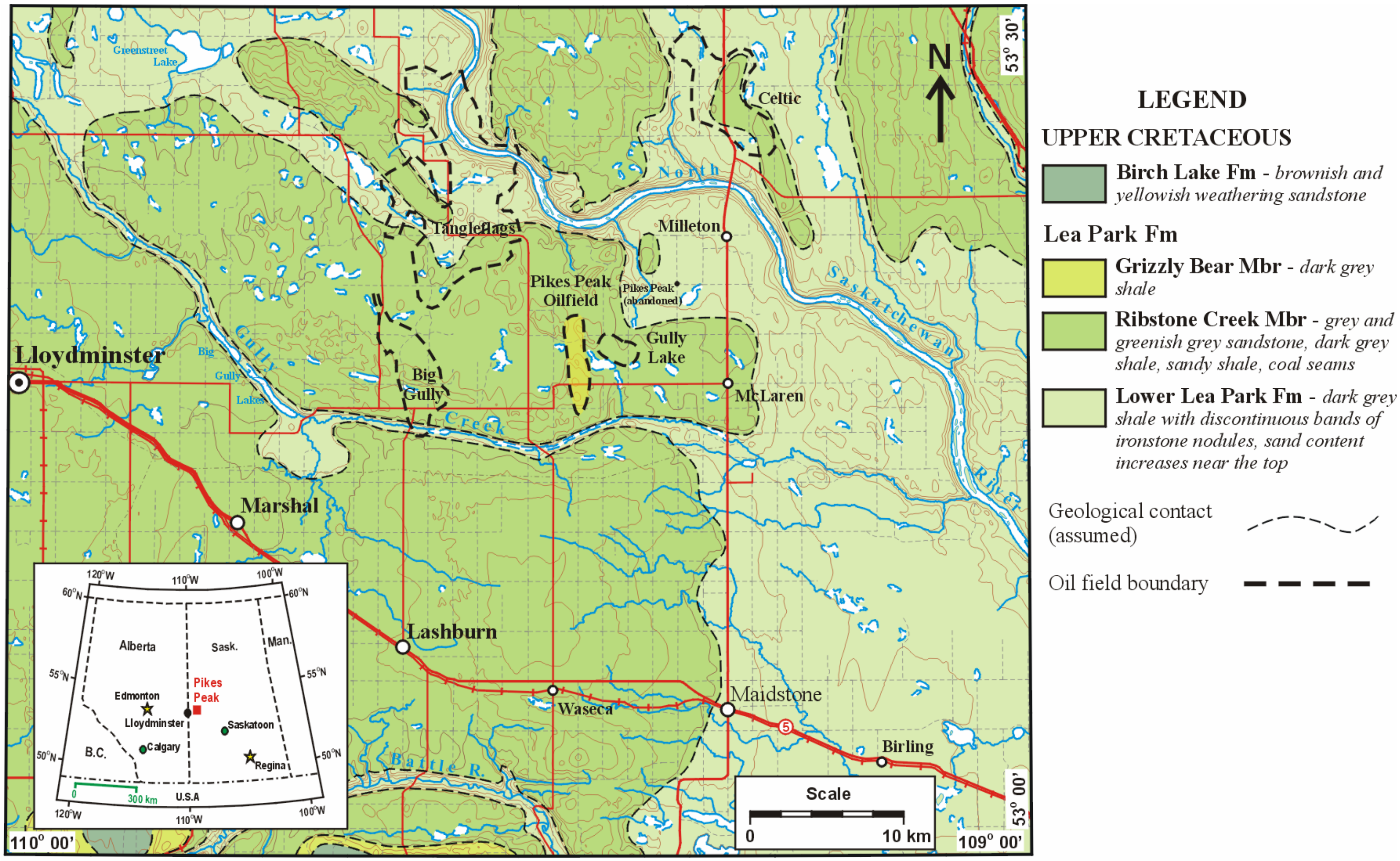

Figure 1.1: Location map of the Pikes Peak oil field (Unit descriptions and geological contacts modified from Geological Survey of Canada Map 490A, scale 1:253,440).

linear and 2) 15.625 s, 25-150 Hz nonlinear (0.2 dB/Hz). A 0.2-s taper length was used for both the start and end of the sweep. The uncorrelated data were recorded for each of the four sweeps per source point.

The primary objectives of this seismic survey were: 1) to acquire and process high-resolution Vibroseis data over a steam-driven heavy-oil field; 2) to suppress surface waves via a dual-sensor approach; 3) to perform AVO analysis on Vibroseis data acquired over a steam-driven heavy-oil field, 4) examine Vibroseis correlation vs deconvolution, and 5) to repeat acquisition over a previous 1991 2-D seismic line to observe possible 4-D effects.

1.4.2 Synthetic data

The synthetic P-P and P-S data of chapter 3 were generated using a multioffset synthetic seismogram (Lawton and Howell, 1992; Margrave and Foltinek, 1995) and blocked models of depth versus V_P, V_S and ρ. These models were then raytraced for P-P and P-S incidence, reflection and transmission angles, and amplitudes were calculated using the Zoeppritz equations. The resulting P-P and P-S offset gathers were then used to obtain the expected normalized amplitude values at each offset range. The stacked P-P and P-S sections were matched to these values representing the stacked response over these offsets.

1.5 Hardware and software used

The software that carries out the simultaneous PP-PS inversion is a module called joint P-P and P-S AVO inversion in ProMAX updated and documented by Mr. David Henley. Software packages SYNTH and LOGEDIT in MATLAB were used to create the synthetic seismograms. Well Editor, GeoGraphix, Model Builder, CorelDraw and Corel PHOTO-PAINT were also used in the course of this research and the composition of this thesis.

The work presented in this thesis was created on a Sun Microsystems network operated by the CREWES Project of the Department of Geology and Geophysics at the University of Calgary. The majority of the programming was done in MATLAB programming language. This includes the direct computation of impedance and pore-fluid parameters from well logs and the correlation of the simultaneous inversion and well-log computation. A number of other MATLAB-based programs coded by Dr. Gary Margrave of the University of Calgary were also utilized in this research. Synthetic data were generated using SYNTH, a seismic modeling package originally developed by Dr. Ed Krebes and Dr. Don Lawton of the University of Calgary, and later coded in MATLAB by Dr. Gary Margrave and Mr. Darren Foltinek also of the University of Calgary. Hampson-Russell Geoview was used to edit the well logs to derive the background velocity in depth for the joint inversion.

1.6 Previous work

Larsen (1999) tested the accuracy of the first-order P-S Zoeppritz-equation approximations and developed the complete derivation of a least-squares, linearized simultaneous-inversion method for all single-mode conversions at a given interface (P-P, P-S, S-P and S-S modes). The simultaneous-inversion method is based upon a previous weighted stacking method utilizing P-P seismic data only (Smith and Gidlow, 1987) and its extension by Stewart (1990). The two-parameter linearized, simultaneous-inversion method is the basis of the work carried out in the current thesis. The two parameters are the fractional compressional- and shear- impedance contrasts. Larsen (1999) examined the weighting behavior of the two-parameter linearized, simultaneous-inversion method and compared the behavior to a standard method utilizing P-P seismic data only. He also tested the simultaneous-inversion accuracy and compared it to the same standard P-P method. After comparing the performance of the simultaneous inversion to the standard P-P inversion in the presence of noisy data and applying the simultaneous-inversion method to the 3C-3D Blackfoot dataset, Larsen (1999) concluded that the two-parameter simultaneous weighted-stacking method was significantly more accurate than the P-P weighted-stacking method in the presence of random noise.

CHAPTER 2

METHODOLOGY

2.1 Introduction

The technique of joint PP-PS weighted stacking is used in the inversion study for this thesis. Stewart (1990) developed this method and Larsen et al. (1998), Larsen (1999) and Margrave et al. (2001) provided its first practical applications. The method requires migrated common-image-point (CIP) gathers for both P-P and P-S reflections. These are then summed into a weighted stack, where the weights are derived from a smoothed background velocity model, to estimate fractional P and S impedance. The resulting sets of stacked sections are estimates of changes in P-wave impedance ($\Delta I/I$) and S-wave impedance ($\Delta J/J$). From these weighted stacks, such useful elastic parameters as $\Delta(\lambda\rho)/\lambda\rho$ and $\Delta(\lambda/\mu)/(\lambda/\mu)$ can be derived. For the mathematical basis of this method, I refer to Larsen (1999).

2.2 Simultaneous linearized P-P and P-S inversion

Smith and Gidlow (1987) outline a least-squares, weighted-stacking procedure incorporating P-P seismic data to extract compressional and shear velocities. This method utilizes NMO-corrected prestack P-P seismic data. Ferguson (1996) describes a similar method to derive estimates of shear velocity directly from an NMO-corrected common-conversion-point (CCP) gather. Both methods utilize a background velocity-depth model to compute incidence, reflection and transmission angles. The primary disadvantage of the P-S method is the need for an additional background $\Delta\rho/\rho$ density model. A true simultaneous method first given by Stewart (1990) outlines a procedure that incorporates both P-P and P-S seismic gathers in a joint P-P and P-S inversion. The following inherent advantages of this method over either the P-P or P-S stand-alone methods were summarized by Larsen (1999).

1. A larger amount of data (i.e. P-P and P-S datasets) is incorporated into each estimate of $\Delta I/I$ and $\Delta J/J$. This has the potential to improve signal-to-noise ratio and thus accuracy for each estimate.
2. Shear-impedance estimates are improved, since P-S reflectivity is generally more dependent upon shear-impedance contrast than P-P acoustic-impedance contrast.
3. A joint interpretation of P-P and P-S seismic data is involved, which has other benefits such as long-wavelength estimates of V_P/V_S from T_S/T_P ratios.
4. Elastic-parameter estimates are improved in areas where P-P reflectivity contrasts are weak or noisy due to acquisition or geologic conditions.
5. A simultaneous inversion results in different sets of weights for the P-P and P-S datasets, which may give improved signal-to-noise ratio.

2.3 Physical basis

The physical basis for the method is embodied in the first-order Zoeppritz-equation approximations for plane-wave reflection and transmission coefficients. The approximations are made under the assumptions that two solid half-spaces are welded at an elastic interface, that there are only small relative changes in elastic parameters, and that the average P- and S-wave angles of incidence and transmission across the interface do not approach a critical angle or 90° (Aki and Richards, 1980). The plane-wave assumption is one that can cause inaccurate estimation of near-offset data. These linearized approximations for P-P and P-S reflection coefficients, R_{PP} and R_{PS}, are

$$R_{PP}(\theta)=\frac{1}{2}\left(1-4\frac{\beta^2}{\alpha^2}\mathbf{sin}^2\theta\right)\frac{\Delta\rho}{\rho}+\frac{1}{2\,\mathbf{cos}^2\theta}\frac{\Delta\alpha}{\alpha}-\frac{4\beta^2}{\alpha^2}\mathbf{sin}^2\theta\frac{\Delta\beta}{\beta} \tag{2.1}$$

$$R_{PS}(\theta,\varphi)=\frac{-\alpha\,\mathbf{tan}\,\varphi}{2\beta}(A-B) \tag{2.2}$$

$$A = \left(1 - \frac{2\beta^2}{\alpha^2}\mathbf{sin}^2\theta + \frac{2\beta}{\alpha}\mathbf{cos}\,\theta\,\mathbf{cos}\,\varphi\right)\frac{\Delta\rho}{\rho} \tag{2.3}$$

$$B = \left(\frac{4\beta^2}{\alpha^2}\mathbf{sin}^2\theta - \frac{4\beta}{\alpha}\mathbf{cos}\,\theta\,\mathbf{cos}\,\varphi\right)\frac{\Delta\beta}{\beta} \tag{2.4}$$

where α, β, ρ are the average P-wave, S-wave and density values across an interface, $\Delta\alpha$, $\Delta\beta$, $\Delta\rho$ are the P-wave, S-wave and density contrasts across an interface, θ is the average of the P-wave angle of incidence and transmission across the interface, and φ is the average of the shear-wave angle of reflection and transmission across the interface.

2.4 Implementation

The implementation of this method can be generalized as follows. Firstly, the 3C-2D seismic data were acquired and processed to obtain high-quality, true relative-amplitude pre-stack seismic data volumes. Because of the simple geologic structure, rather than performing a full pre-stack migration, these volumes were NMO-corrected and stacked into limited-offset volumes that could be poststack migrated. Five such limited-offset, migrated sections were created for both P-P and P-S reflections. Because true-amplitude recovery in the regular processing is not perfect, synthetic seismograms for each reflection type were used to restore the regional behavior of reflectivity over the depth range above the zone of interest with offset. These were constructed from well logs by raytracing for the traveltimes and using the Zoeppritz equations for the reflection-amplitude-calculations. They were then band-limited to the recovered signal band of the data. Then the expected RMS amplitude for each offset range was calculated from the P-P and P-S synthetic seismograms. Each limited-offset migrated data volume was then rescaled by a constant factor to have the same RMS amplitude as the corresponding synthetic seismogram.

Secondly, offset ranges were chosen to create limited-offset stacked sections so that the amount of data needed for AVO analysis would be decreased and both the speed of calculation and the signal-to-noise ratio would be increased. Since migration was also applied to the stacked sections, the quality of imaging was greatly improved. Thirdly, P-P and P-S reflection events were correlated in depth by comparing them to the synthetic seismograms. The data were then shifted to a common datum, just above the zone of interest, to restore the original depositional environment and reduce the errors in the inversion. Finally, each offset data volume was weighted and they were summed together to estimate fractional P or S impedance contrast as follows.

The fractional P-wave and S-wave impedance contrast formulae are:

$$\frac{\Delta I}{I} = \sum_{k=1}^{N} \left[W_{PP,I}\left(\theta_{PP,k}, \varphi_{PP,k}\right) R_{PP}\left(\theta_{PP,k}\right) + W_{PS,I}\left(\theta_{PS,k}, \varphi_{PS,k}\right) \right] \tag{2.5}$$

and

$$\frac{\Delta J}{J} = \sum_{k=1}^{N} \left[W_{PP,J}\left(\theta_{PP,k}, \varphi_{PP,k}\right) R_{PP}\left(\theta_{PP,k}\right) + W_{PS,J}\left(\theta_{PS,k}, \varphi_{PS,k}\right) R_{PS}\left(\theta_{PS,k}\right) \right] \tag{2.6}$$

where $\theta_{PP,k}$ is the average of P-wave angle of incidence and reflection; $\varphi_{PP,k}$ is P-wave angle of transmission; $\theta_{PS,k}$ is the average S-wave angle of reflection; $\varphi_{PS,k}$ is the average S-wave angle of transmission. $W_{PP,I}$, $W_{PS,I}$, $W_{PP,J}$ and $W_{PS,J}$ represent the weights for P-P and P-S limited-offset stacks; R_{PP} and R_{PS} are respectively the observed P-P and P-S reflectivities, and $\frac{\Delta I}{I}$ and $\frac{\Delta J}{J}$ represent the fractional P-wave and S-wave impedance contrast to be estimated as shown in figure 2.1.

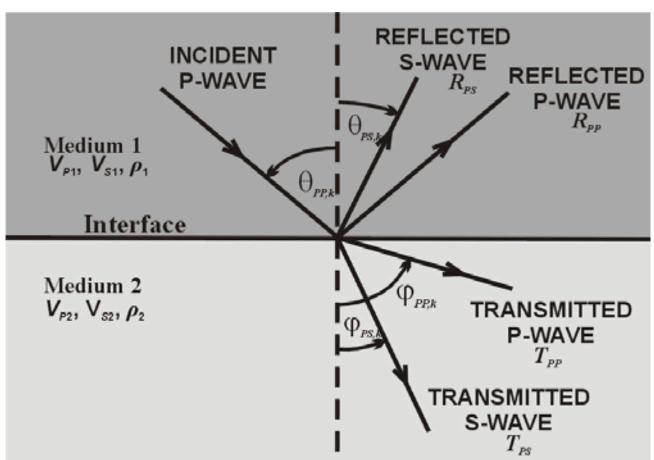

Figure 2.1: Physical basis of the first-order Zoeppritz-equation approximations for plane-wave reflection and transmission coefficients.

The sum includes both P-P and P-S data; the weights are functions of the average incidence and reflection angles for smooth P-wave and S-wave velocity-depth models. Raytracing is used to determine the incidence, reflection and transmission angles. The formulae for the weights are edited from Larsen (1999) and shown in equations (2.7) to (2.14).

$$W_{PP,I} = \frac{\sum_{i=1}^{N} A_i \left[\sum_{j=1}^{N} \left(B_j^{\,2} + D_j^{\,2} \right) \right] - \sum_{i=1}^{N} B_i \left[\sum_{j=1}^{N} \left(A_j B_j + C_j D_j \right) \right]}{\sum_{i=1}^{N} \left(A_i^2 + C_i^{\,2} \right) \left[\sum_{j=1}^{N} B_j^{\,2} + D_j^{\,2} \right] - \left[\sum_{i=1}^{N} \left(A_i B_i + C_i D_i \right) \right]^2} \tag{2.7}$$

$$W_{PS,I} = \frac{\sum_{i=1}^{N} C_i \left[\sum_{j=1}^{N} \left(B_j^{\,2} + D_j^{\,2} \right) \right] - \sum_{i=1}^{N} D_i \left[\sum_{j=1}^{N} \left(A_j B_j + C_j D_j \right) \right]}{\sum_{i=1}^{N} \left(A_i^2 + C_i^{\,2} \right) \left[\sum_{j=1}^{N} \left(B_j^{\,2} + D_j^{\,2} \right) \right] - \left[\sum_{i=1}^{N} \left(A_i B_i + C_i D_i \right) \right]^2} \tag{2.8}$$

$$W_{PP,J} = \frac{\sum_{i=1}^{N} B_i \left[\sum_{j=1}^{N} \left(A_j^{\,2} + C_j^{\,2} \right) \right] - \sum_{i=1}^{N} A_i \left[\sum_{j=1}^{N} \left(A_j B_j + C_j D_j \right) \right]}{\sum_{i=1}^{N} \left(A_i^2 + C_i^{\,2} \right) \left[\sum_{j=1}^{N} \left(B_j^{\,2} + D_j^{\,2} \right) \right] - \left[\sum_{i=1}^{N} \left(A_i B_i + C_i D_i \right) \right]^2} \tag{2.9}$$

$$W_{PS,J} = \frac{\sum_{i=1}^{N} D_i \left[\sum_{j=1}^{N} \left(A_j^{\,2} + C_j^{\,2} \right) \right] - \sum_{i=1}^{N} C_i \left[\sum_{j=1}^{N} \left(A_j B_j + C_j D_j \right) \right]}{\sum_{i=1}^{N} \left(A_i^2 + C_i^{\,2} \right) \left[\sum_{j=1}^{N} \left(B_j^{\,2} + D_j^{\,2} \right) \right] - \left[\sum_{i=1}^{N} \left(A_i B_i + C_i D_i \right) \right]^2} \tag{2.10}$$

$$A_i(\theta_k) = \frac{1 + \mathbf{tan}^2\, \theta_k}{2} \tag{2.11}$$

$$B_i(\theta_k) = -4 \frac{\beta^2}{\alpha^2} \mathbf{sin}^2\, \theta_k \tag{2.12}$$

$$C_i(\theta_k,\varphi_k)=\frac{-\alpha\,\mathbf{tan}\,\varphi_k}{10\beta}\left(1+2\,\mathbf{sin}^2\varphi_k-2\frac{\beta}{\alpha}\mathbf{cos}\,\theta_k\,\mathbf{cos}\,\varphi_k\right) \tag{2.13}$$

$$D_i(\theta_k,\varphi_k)=\frac{\alpha\,\mathbf{tan}\,\varphi_k}{\beta}\left(2\,\mathbf{sin}^2\varphi_k-2\frac{\beta}{\alpha}\mathbf{cos}\,\theta_k\,\mathbf{cos}\,\varphi_k\right) \tag{2.14}$$

N is the number of offset bins for creating limited-offset stacked sections; θ_k is the average of the P-wave angles of incidence, $\theta_{PP,k}$, and transmission, $\varphi_{PP,k}$, across the interface. φ_k is the average of the shear-wave angle of reflection, $\theta_{PS,k}$, and transmission, $\varphi_{PS,k}$, across the interface.

Once $\Delta I/I$ and $\Delta J/J$ are weighted and inverted as shown in equations (2.5) and (2.6), the attributes $\Delta(\lambda\rho)/\lambda\rho$ and $\Delta(\lambda/\mu)/(\lambda/\mu)$ can be expressed in terms of $\Delta I/I$ and $\Delta J/J$ as given by equations (2.15) and (2.16) (Larsen, 1999).

Fractional $\lambda\rho$ contrast: $$\frac{\Delta(\lambda\rho)}{\lambda\rho}=\frac{2}{\alpha^2-2\beta^2}\left(\alpha^2\frac{\Delta I}{I}-2\beta^2\frac{\Delta J}{J}\right) \tag{2.15}$$

Fractional λ/μ contrast: $$\frac{\Delta(\lambda/\mu)}{\lambda/\mu}=\frac{2\alpha^2}{\alpha^2-2\beta^2}\left(\frac{\Delta I}{I}-\frac{\Delta J}{J}\right) \tag{2.16}$$

where α and β are the average P-wave and S-wave velocities across the interface, $I=\rho\alpha$, and $J=\rho\beta$.

2.5 Comparison of weighting behavior as a function of offset

According to equations (2.3) and (2.4), for the case of a P-P inversion only, $W_{PS,I}$ and $W_{PS,J}$ should both be zero. In the case of this study, each set of weights was calculated assuming a range of offset from 0 to 2000 m in intervals of 40 m with a reflector depth at 1500 m. The behavior of these weights for P-P alone and PP-PS simultaneously as a function of offset is shown in figures 2.3 to 2.5 for the elastic constants given in figure 2.2.

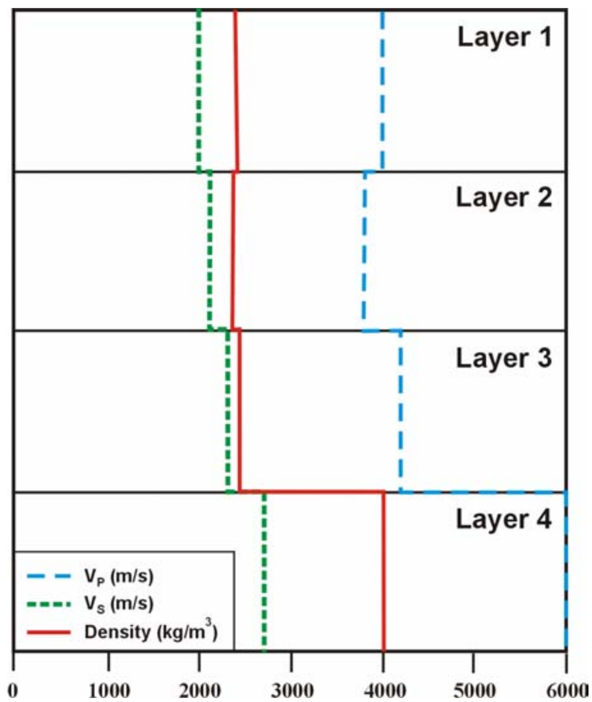

Figure 2.2: V_P, V_S and density values for a 4-layer earth model. Depths are not included since a full range of incidence angles is assumed at each interface (adapted from Larsen 1999).

Several key observations are made from these figures. The magnitudes of the weights for the simultaneous P-P and P-S inversion method are lower than for the P-P only inversion, which might be due to the more even weighting behavior using the simultaneous inversion method and the increased data fold. As expected, the weights for the P-S datasets are zeros at zero offset. The weights for $\Delta I/I$ and $\Delta J/J$ in P-P inversion often change signs with increasing offset. This effect tends to cancel the middle offsets and weight the near and far offsets more heavily. This explains why the near and far offsets of a given P-P offset gather are differentiated in the analysis of AVO anomalies. For P-P inversion only, the fold of the overall $\Delta I/I$ section is lower since mainly only the near and far offsets are included in the weighted stack. This could worsen the signal-to-noise ratio of the $\Delta I/I$ and $\Delta J/J$ stacks.

The weighting of the P-P dataset for the $\Delta I/I$ stack applies each offset more evenly using the simultaneous inversion method than PP-only inversion. This effect, in

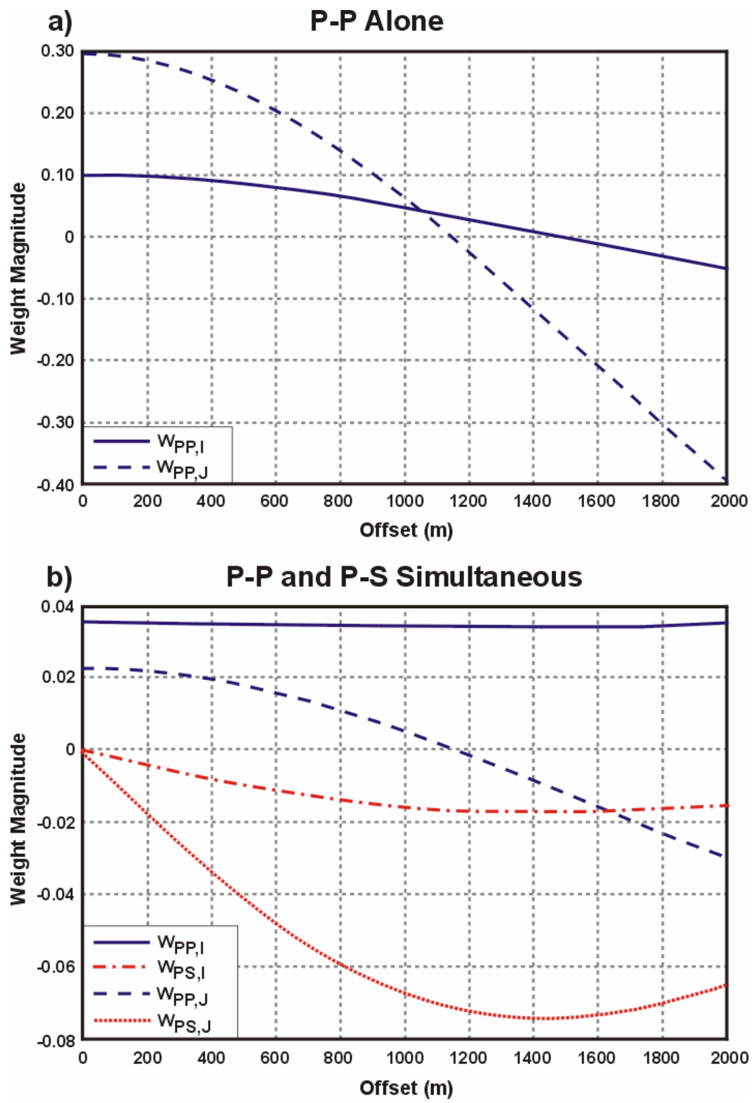

Figure 2.3: Weights applied to R_{PP} at the 1-2 interface in the case of a) P-P data only. Weights applied to R_{PP} and R_{PS} at the 1-2 interface in the case of b) both P-P and P-S data (adapted from Larsen, 1999).

addition to doubling the data fold for each $\Delta I/I$ stack, leads to an improvement in thesignal-to-noise ratio of the $\Delta I/I$ inversion result. Figure 2.3 to 2.5 also show that the weights $W_{PS,I}$ are generally smaller in absolute value than the weights $W_{PP,I}$. Since R_{PP} is usually larger in magnitude than R_{PS} and R_{PP} is weighted more, the effect that the weight $W_{PS,I}$ has on the estimate of $\Delta I/I$ is relatively small.

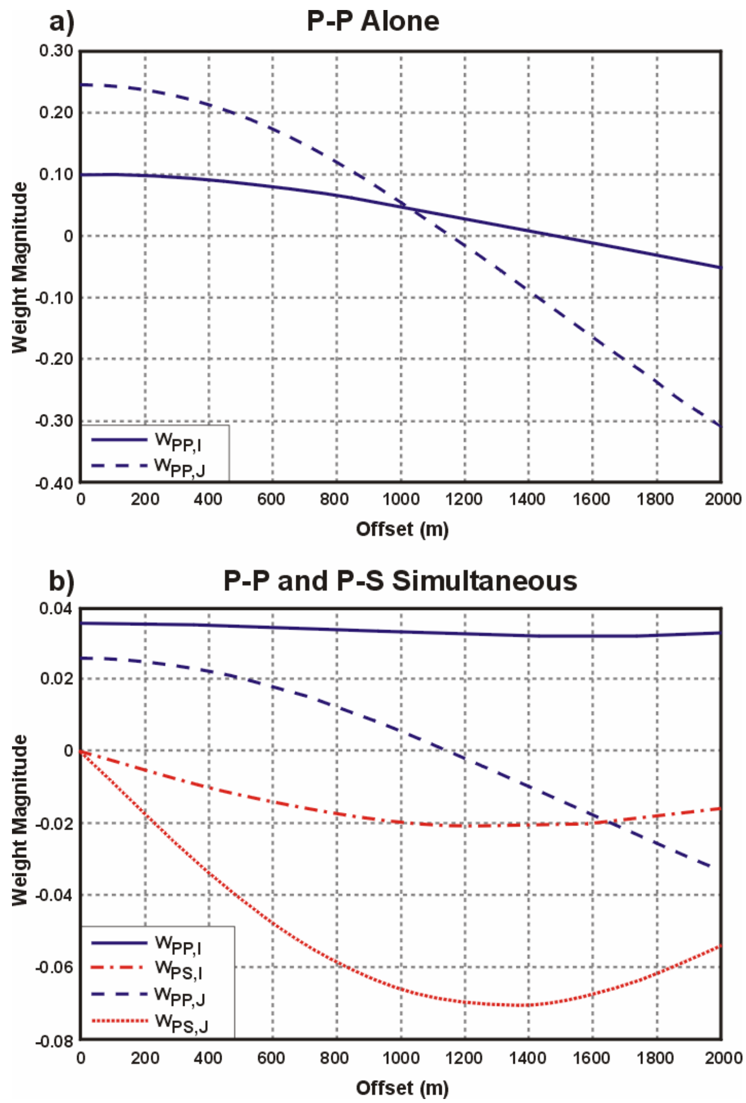

Figure 2.4: Weights applied to R_{PP} at the 2-3 interface in the case of a) P-P data only. Weights applied to R_{PP} and R_{PS} at the 2-3 interface in the case of b) both P-P and P-S data (adapted from Larsen 1999).

The absolute values of the weights $W_{PS,J}$ are generally larger than those of the weights $W_{PP,J}$. This demonstrates that the changes in $\Delta J/J$ are dependent more on R_{PS} compared with R_{PP}. It is also observed that the weights $W_{PP,J}$ tend to change sign with increasing offset in both PP-only and simultaneous-inversion methods. But the weights $W_{PS,J}$ are often at their maximum magnitude in the medium-offset range and the low

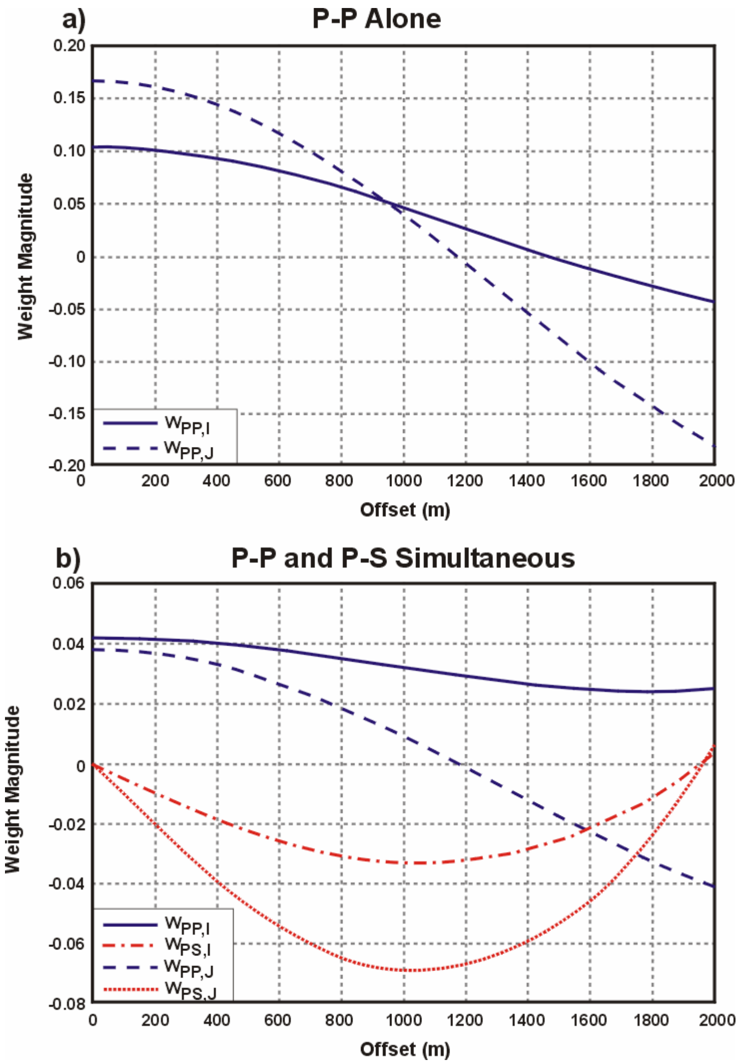

Figure 2.5: Weights applied to R_{PP} at the 3-4 interface in the case of a) P-P data only. Weights applied to R_{PP} and R_{PS} at the 3-4 interface in the case of b) both P-P and P-S data (adapted from Larsen 1999).

weights $W_{PP,J}$ are thus compensated in the medium-offset range by virtue of the R_{PS} dataset being weighted more heavily.

2.6 Simultaneous inversion accuracy

There are three major possible sources for errors mentioned by Larsen (1999) that may affect the accuracy of the results from applying simultaneous inversion. They are matrix-inversion error, Zoeppritz-equation approximation error and the presence of noise.

In the presence of the first two kinds of errors, Larsen (1999) concluded that the results of inversion for the same set of observed elastic-parameter contrasts are comparable. Errors can be quite large if the elastic contrasts are large and the assumptions made in both the P-P and P-S Zoeppritz-equation approximations are violated. As a result, both inversion methods should be used with caution where large incidence angles and large changes in elastic parameters are expected.

In realistic cases where noise is present, Larsen (1999) found that the simultaneous-inversion method is more accurate than the P-P inversion method. This difference is most noticeable where signal-to-noise ratio is at a minimum. Even with a large amount of noise in the P-S dataset, all estimates of $\Delta I/I$, $\Delta J/J$ and $\Delta\rho/\rho$ (fractional density contrast) are more accurate using simultaneous inversion. Since shear impedance affects P-P and P-S reflection amplitude most strongly at far offsets, the inversion for the $\Delta J/J$ stack relies most heavily upon far-offset contribution. On the other hand, it is compressional impedance that affects P-P reflection amplitude most strongly at near offsets and thus it is more accurate as it is more consistent with the assumptions made in the Zoeppritz-equation approximations.

2.7 Chapter summary

The Zoeppritz-equation approximations for P-P and P-S reflectivity were modified to appear as functions of compressional and shear impedance values in Larsen (1999). The physical basis, mathematical basis and advantages of the two-parameter joint PP-PS AVO inversion were then introduced according to Stewart (1990) and Larsen (1999). These two parameters are fractional compressional- and shear-impedance contrasts. The fractional $\lambda\rho$ and λ/μ contrasts can also be derived from the impedance contrasts. The implementation of the two-parameter joint inversion on the Pikes Peak 3C-2D dataset was generalized on the basis of the joint-inversion theory. Next, a four-layer earth model and the behavior of the weights for the joint inversion and P-P stand-alone inversion were adapted from Larsen (1999) and compared. Comparison of the weighting behavior and inversion accuracy indicates that joint inversion is theoretically superior to P-P stand-alone inversion.

CHAPTER 3

PREPARING INPUT DATA FOR JOINT PP-PS AVO INVERSION

3.1 Introduction

Chapter 2 outlined a least-squares, linearized, simultaneous inversion method in which the band-limited P-P and P-S seismic data can be inverted to provide similarly band-limited estimates of fractional acoustic and shear impedance. In this chapter, the simultaneous inversion method is applied to a previously acquired and processed 3C-2D dataset. This procedure is composed of several steps. The first is to acquire and process the 3C-2D seismic data to obtain high quality, true-amplitude pre-stack seismic data volumes. The second is to correlate P-P and P-S reflection events in depth or traveltime. The last step is to weight each limited-offset data volume by a set of model-based weights and compute the weighted reflectivity stacks resulting in band-limited estimates of fractional compressional and shear reflectivity.

3.2 Pikes Peak geological overview

Pikes Peak oil field has been owned and operated by Husky Energy Ltd since 1981 and over 35 million barrels have been produced (Watson et al., 2001). Steam-drive technology has been used to enhance recovery. The principle of steam drive is to reduce the effective viscosity of the oil and increase the mobility in the reservoir by injecting high-temperature and -pressure steam.

Sediments of the Mannville Gp overlie a pre-Cretaceous unconformity developed on gently southwesterly dipping Paleozoic strata. Post-Mannville tilting to the southwest has enhanced the structural dip on the subcropping Paleozoic strata in the Lloydminster area (Orr et al., 1977). Dissolution of deep Devonian salt units around the flanks of the field set up the combination structural and stratigraphic trap (Van Hulten, 1984).

The two major producing reservoirs in the Pikes Peak field are the General Petroleum Fm and the Waseca Fm. This study discusses only the Waseca oil sands that are located in the Lower Cretaceous Mannville Group and about 480 m below the surface of Earth.

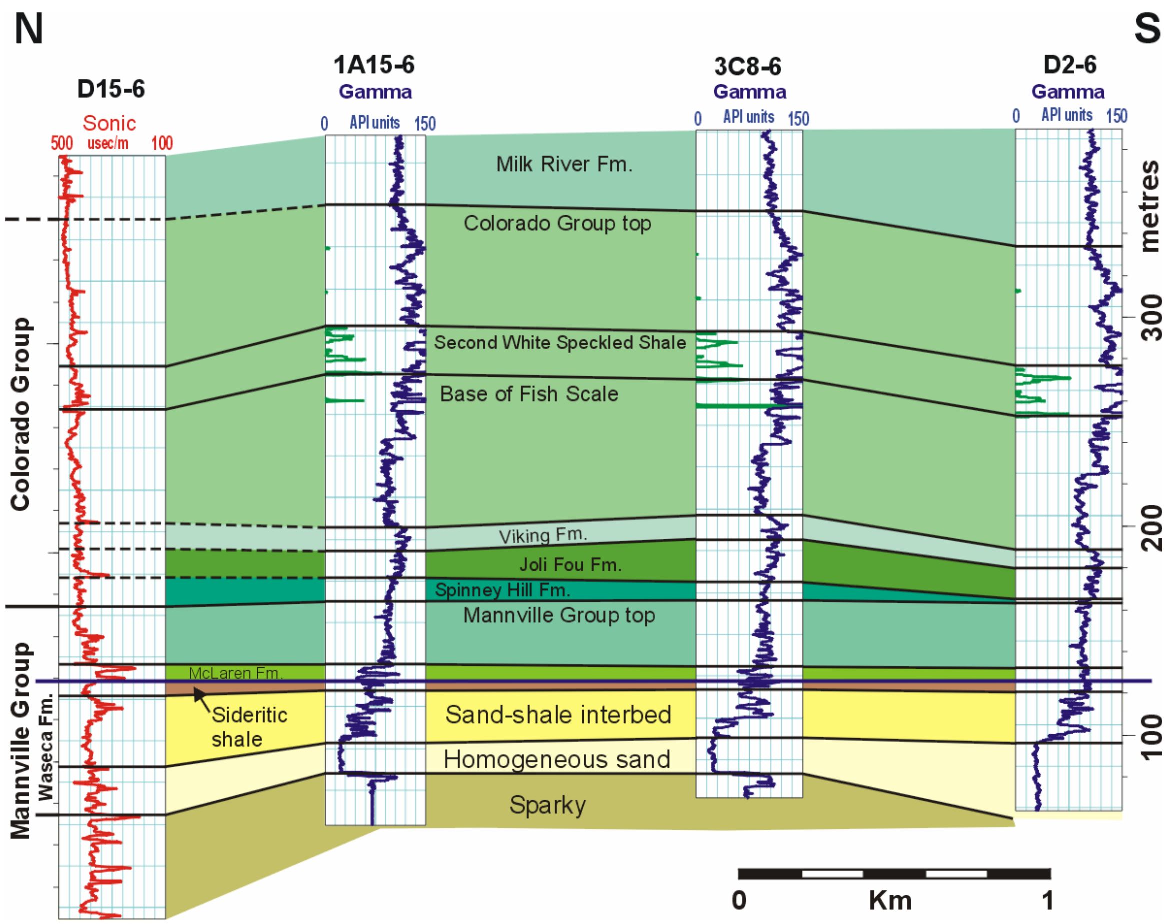

Figure 3.1: Well-log cross-section illustrating the Lower Cretaceous stratigraphy (edited from Leckie et al. 1994) (flattened at the top of the Waseca Fm). Van Hulten (1984) interpreted a channel sequence previously within the Waseca Fm and I have refined this classification.

In figure 3.1, which is composed of the four wells along the seismic line from north to south, the coal and sideritic shale at the top of the Waseca Fm form the perfect seal for the hydrocarbon in shale/sand interbed and homogeneous sand units (Van Hulten,

1984) in the middle and lower Waseca. The up-fining depositional sequences demonstrate typical channel facies. The main producing zone within the Waseca Fm is the homogeneous sand unit. It ranges between 5 and 30 m of net pay within the field (Van Hulten, 1984). The coal at the top of the Sparky forms a horizon that is resistive to channel erosion.

3.3 Seismic processing

Several steps must be taken prior to applying the simultaneous weighted-stacking procedure. After the seismic data were acquired, I processed the 3C-2D data in a true-amplitude manner. I paid careful attention to maintaining the correct phase and polarity of the processed seismic gathers.

Among the three geophone components, the energy from seismic reflections is mainly received by the vertical and radial components. So only the vertical- and radial-component data were processed and used in this project. The data were originally processed by Matrix Geoservices Ltd and reprocessed by the author (figure 3.2).

3.3.1 Noise problem and solution

While the seismic data were being acquired, pump jacks for hydrocarbon production were running constantly. The noise from pump jacks shows up in both the vertical- and radial-component data, as we can see in figure 3.3. Because of the higher frequencies (2-150 Hz) of the vertical-component data, the pump-jack noise does not dominate the stacked P-P section. In comparison, the radial-component has lower frequencies (2-60 Hz) and the pump-jack noise would dominate the P-S stacked section. This is why an *f-k* filter was applied to the radial component (figure 3.4).

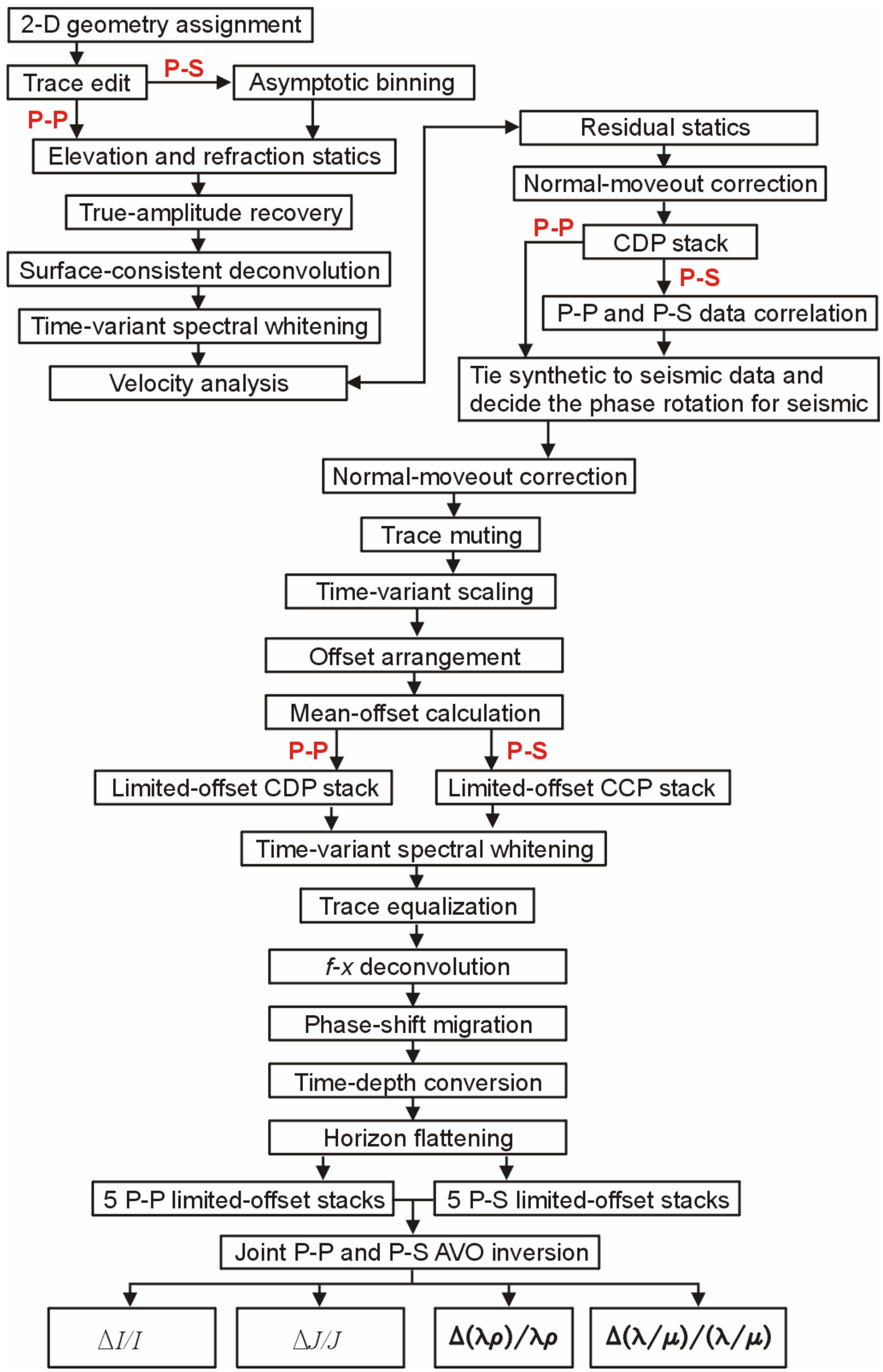

Figure 3.2: Workflow for data preparation and joint PP-PS AVO inversion.

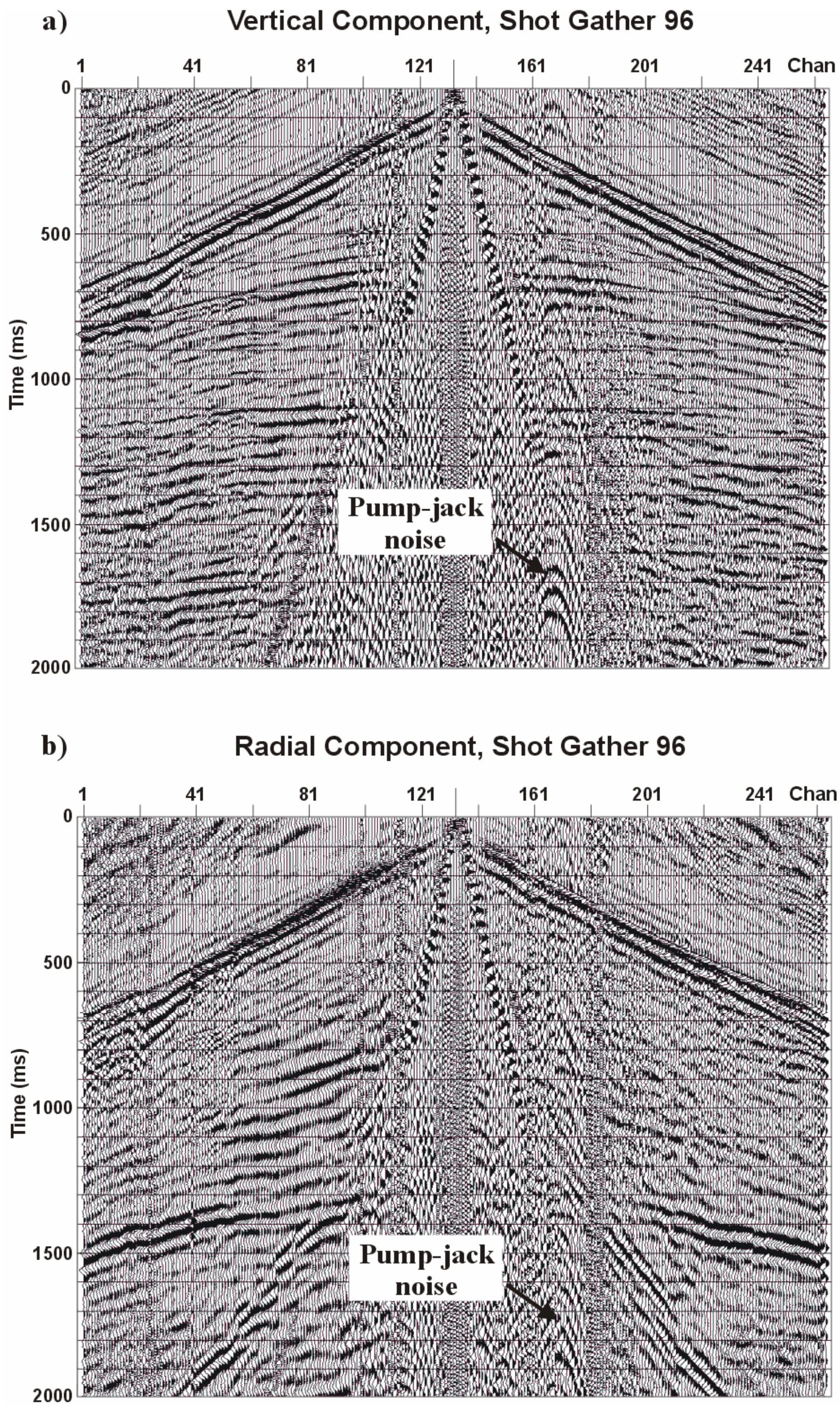

Figure 3.3: a) Shot gather 96, vertical component and b) radial component; both with automatic gain correction (AGC window 500 ms). Notice that the frequencies of the vertical component are higher than those of the radial component.

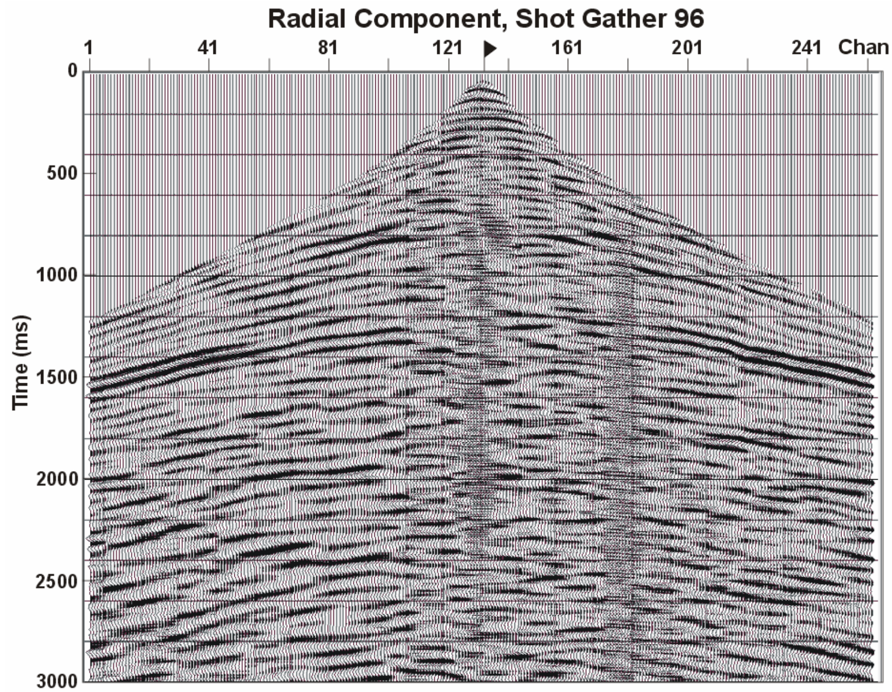

Figure 3.4: Shot gather 96 in the radial component after application of *f-k* filter and trace muting. Most of the pump-jack noise and ground roll are eliminated.

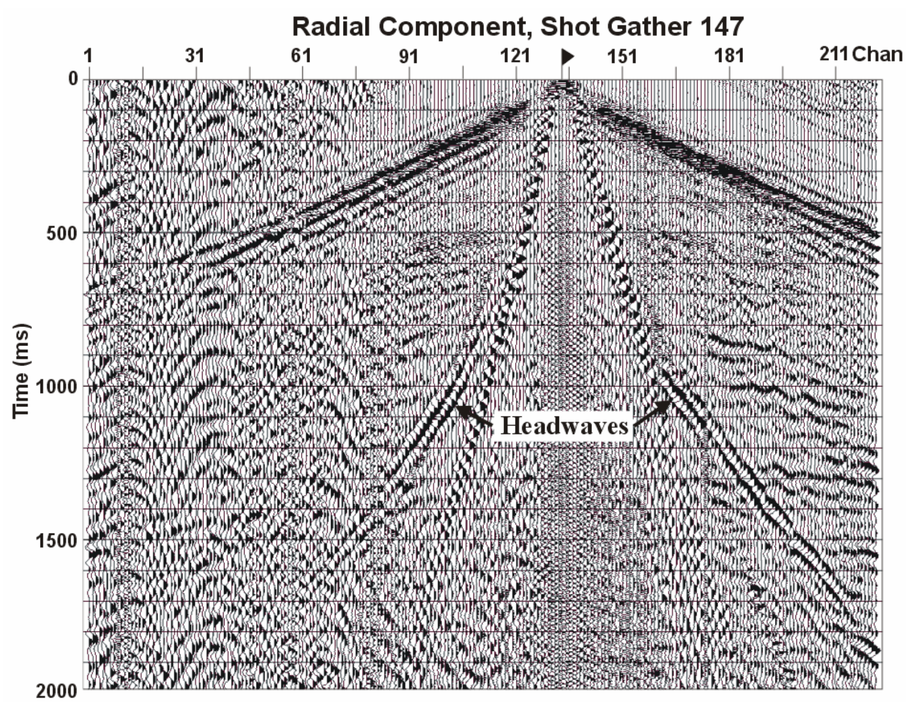

Figure 3.5: Shot gather 147 in the radial component shows strong shear head waves that can be picked for statics calculation.

3.3.2 Statics correction

Source gathers of the radial-component data exhibited a strong shear head wave that could be confidently picked as shown in figure 3.5. The traveltime picks of the refracted shear wave were then used directly to compute the S-wave receiver statics. Combining these S-wave receiver statics with the P-wave source statics provided the P-S refraction-statics solution. Because the refracted shear wave was prevalent on the radial component data, it demonstrates that, in this case, the Vibroseis source generates significant shear-wave energy. The statics correction of radial-component data used in the inversion was done by Matrix Geoservices Ltd. Matrix paid careful attention to the large receiver statics present in the radial-component dataset. I also created the common-receiver stack (figure 3.6) so that reflectors with small lateral depth variations were corrected. After that, residual source and receiver statics were calculated and eliminated.

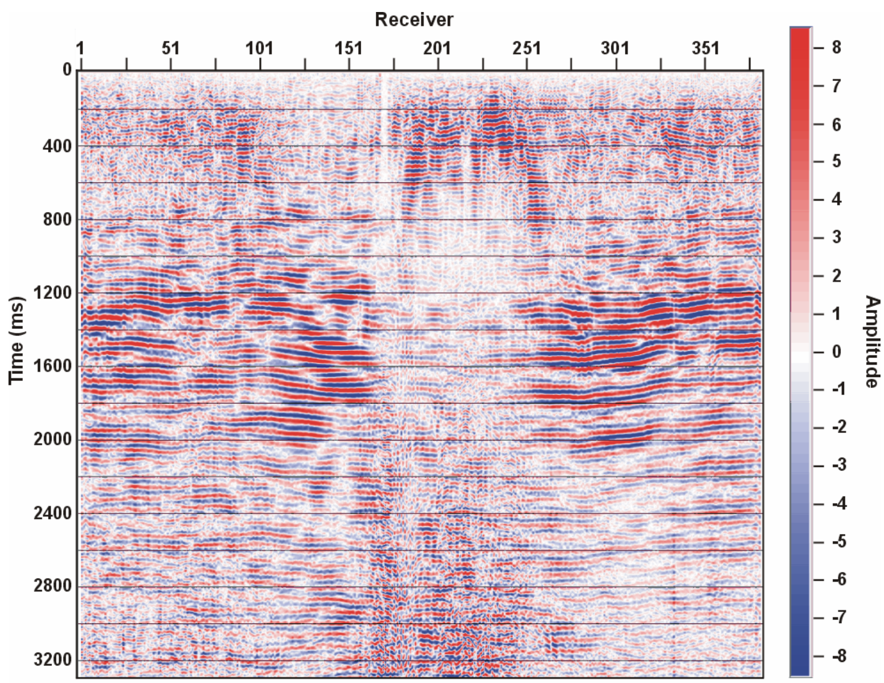

Figure 3.6: A common-receiver stack created to correct small lateral changes in the displayed depths of the events.

3.3.3 Creating limited-offset stacked traces

Conventional P-P and P-S data processing flows (from trace editing to stacking) were developed using established methods. The starting point for P-P data preparation requires gathers of traces sorted by CDP and absolute offset (*aoffset* by ProMAX), while the P-S processing requires data gathers of traces mapped to CCP (common conversion point) and sorted by CCP and absolute offset. Any CDP gathers not having corresponding CCP gathers may be discarded, and vice versa, since there should be a one-to-one correspondence between CDP and CCP numbers.

However, to retain information about the variation of reflectivity with offset, each dataset was segmented into five limited-offset stacks. For the P-P data, the *aoffset* range from 0 to 759 m was divided into five overlapping bins that were 253 m wide, while for the P-S data, 284-m bins were used from 0 to 852 m. By using P-P reflection traces from several offset ranges and P-S traces also from several offset ranges, not only can P-P impedance and P-S impedance be computed, but additional rock parameters as well. The offset ranges for the P-P and P-S datasets for reflections from the top of the production zone, i.e. the Waseca Fm, are given in table 3.1.

P-P *aoffset* RANGE	P-S *aoffset* RANGE	NAMING CONVENTION
0-253	0-284	NEAR
126.5-379.5	142-426	NEAR-MID
253-506	284-568	MID
379.5-632.5	426-710	MID-FAR
506-759	568-852	FAR

Table 3.1: Offset ranges used to construct limited-offset stacks at the depth of the Waseca Fm.

Usually, the more overlapping limited-offset bins are created, the higher resolution the result of the inversion will have because more detailed amplitude variation with offset will be included in the limited-offset stacked sections. But for the Pikes Peak data, if the entire offset range corresponding to the zone of interest is divided into more than five or six bins, the zone of interest can't be completely imaged in the far-offset stacked sections. That is why I created five overlapping limited-offset bins. In order to obtain overlapping offset bins with the same interval, the number of limited-offset bins has to be odd, not even. The offset ranges of the P-S offset bins are slightly larger than those of the corresponding P-P offset bins because for the seismic reflection received by each geophone, the displacement of asymptotic binning points from certain shot for P-S data is commonly greater than that of common depth points for P-P data.

A flow to create either P-P or P-S limited-offset common image point gathers with mean offset computed and stored in trace headers is shown below. (It is assumed that P-P and P-S data are processed separately at this stage). As can be seen, the flow consists of input of either the P-P or P-S dataset, NMO correction, trace muting and a cascade of conditional loops, each of which accepts only traces having absolute offsets within the limits specified in the *if* statement. Within each loop, a sort operation first orders the traces by absolute offset and forms new ensembles. Next, a new operation '***Mean offset***' (Henley et al., 2002) computes the mean offset for each ensemble and creates a new trace header, *meanoff*', in which to post the value. Each limited-offset ensemble is then written out to a disk file as the last operation in the loop.

```
Disk Data Input  (the P-P or P-S CDP gathers obtained from
                     prestack processing)
Normal Moveout   (apply normal moveout correction so that
          traces can be stacked later in limited offset ranges)
Trace Muting     (eliminate the critical angles)
IF     (test for aoffset between XMIN1 and XMAX1)
Inline Sort  (sort over CDP and aoffset to create
               Limited-offset CDP ensembles)
Mean Offset  (compute mean offset, place it in new meanoff
 trace header; header DS_SEQNO is also set to user parameter)
Disk Data Output (the limited-offset P-P or P-S common-image-
                    point gathers, with proper headers)
ENDIF
IF    (test for aoffset between XMAX1 and XMAX2)
      Inline Sort
      Mean Offset
```

Disk Data Output

ENDIF

etc.

The product of this flow is one file per conditional loop, each containing the decimated CDP or CCP gathers whose individual trace offsets fall within the corresponding offset range and whose traces all contain a new trace header set to the mean offset for each decimated gather. CDP and CCP gathers are shown in figure 3.7.

3.3.4 Creating limited-offset stacked sections

A flow to stack the limited-offset CDP/CCP gathers, and move the *meanoff* to the *aoffset* trace header is shown below. The flow consists of a short sequence of operations.

Disk Data Input (first set of limited-offset CDP/CCP gathers created by the previous flow for either P-P or P-S traces)

CDP/CCP Stack (stack all input traces by CDP/CCP)

Phase Shift Migration (or other suitable post-stack migration methods)

Time-Depth Conversion (convert traces from time to depth domain)

Trace Header Math (set *aoffset* = *meanoff*)

Disk Data Output (limited-offset CDP/CCP stacked traces, in depth, for first offset range, with *aoffset* containing the Mean Offset for each input CDP/CCP gather)

Disk Data Input (the next set of limited-offset CDP/CCP gathers created by the previous flow for either P-P or P-S traces)

CDP/CCP Stack (stack all input traces by CDP/CCP)

Phase Shift Migration (or other post-stack migration methods)

Time-Depth Conversion (convert traces from time to depth domain)

Trace Header Math (set *aoffset* = *meanoff*)

Disk Data Output (limited-offset CDP/CCP stack traces, in depth, for the second offset range, with *aoffset* containing the *meanoff* for each input CDP/CCP gather)

etc.

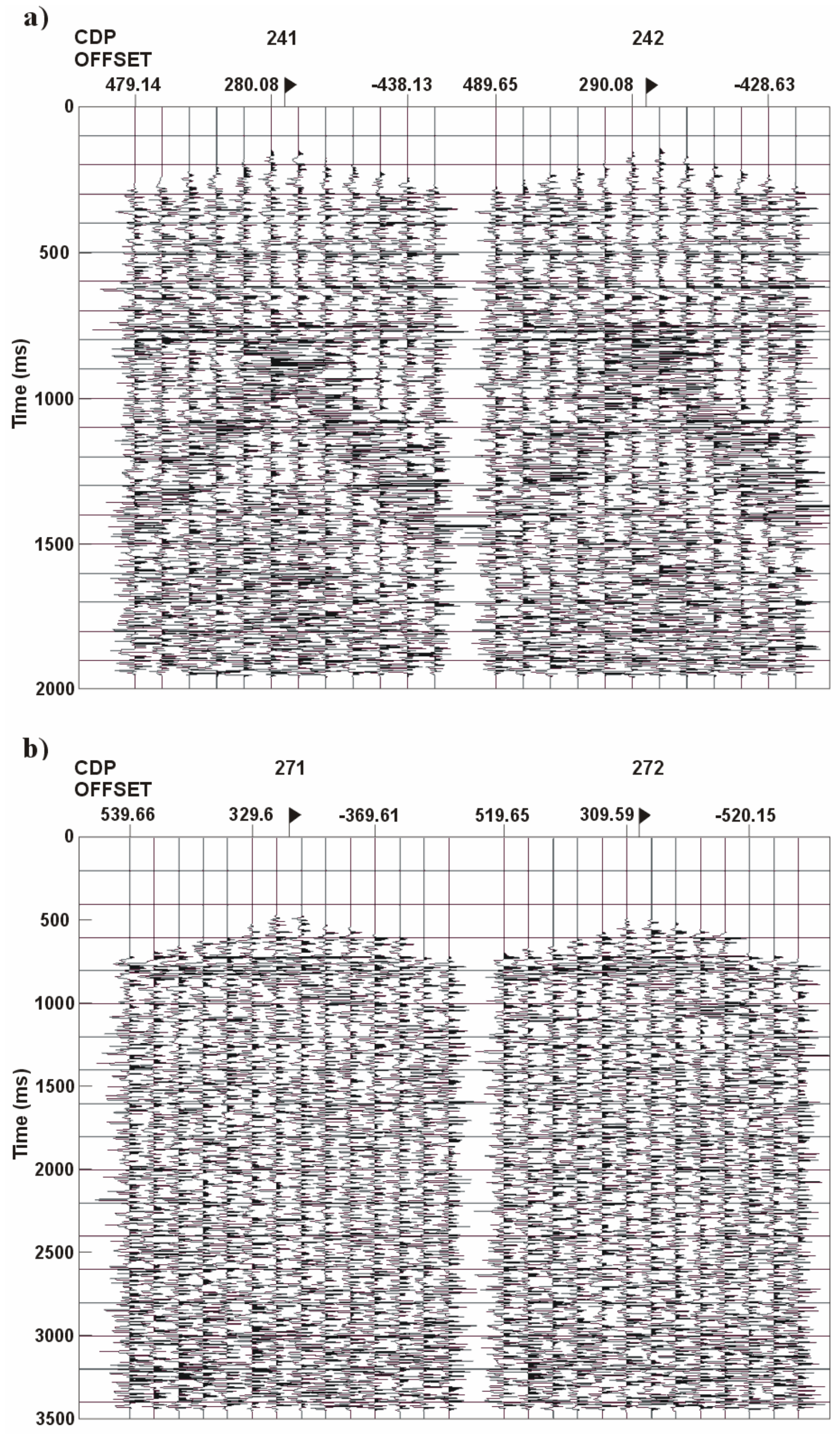

Figure 3.7: a) Vertical-component CDP gathers 241 and 242 within mid-offset range.
b) Radial-component CCP gathers 271 and 272 within mid-offset range.

In each sequence, the corresponding limited-offset ensembles are stacked by CDP (or CCP), then post-stack time migrated using phase-shift migration, and at last time-depth convertion is performed. The last step before output of each file of migrated limited-offset stacked traces is to replace the *aoffset* header with the *meanoff* header for later use by the joint-inversion algorithm. In general, each file of limited offset CDP or CCP gathers is stacked, migrated, and depth-converted, and the mean-offset value posted to the absolute-offset trace-header before outputing the resulting limited-offset P-P or P-S stacked traces as a new file. For CCP stack, the module ***Converted-wave Stack*** in ProMAX was employed. The P-P and P-S data are correlated to calculate the V_P/V_S ratios required in the converted-wave stacking.

After stack, the ten 2-D data volumes were taken through an event-enhancement process of time-variant spectral whitening (TVSW), special prediction (*f-x*), and then into P-P or P-S poststack time-migration. P-P and P-S limited-offset stacked sections are shown in figure 3.8.

It should be emphasized that this flow is not the only possible one for reducing the limited-offset ensembles to migrated, depth-converted limited-offset stacked traces. Other sequences can certainly be constructed, depending upon data quality and the interpretation objectives. Post-stack time migration and depth conversion can be replaced with post-stack depth migration. NMO correction can be deferred from the first flow, for example, and some form of prestack migration used in the second, instead of CDP stack and post-stack migration. However, prestack depth migration is computationally intensive and could be time-consuming, so we implemented a more practical approach using fairly standard technologies.

3.3.5 Event correlation

After all the static corrections and migration were carried out on both the vertical and radial components, event correlation was accomplished by tying P-P and P-S synthetic seismograms. One of the most important sources of error in using the simultaneous-inversion method is the problem of correlating P-P and P-S reflection events in the time or depth domain.

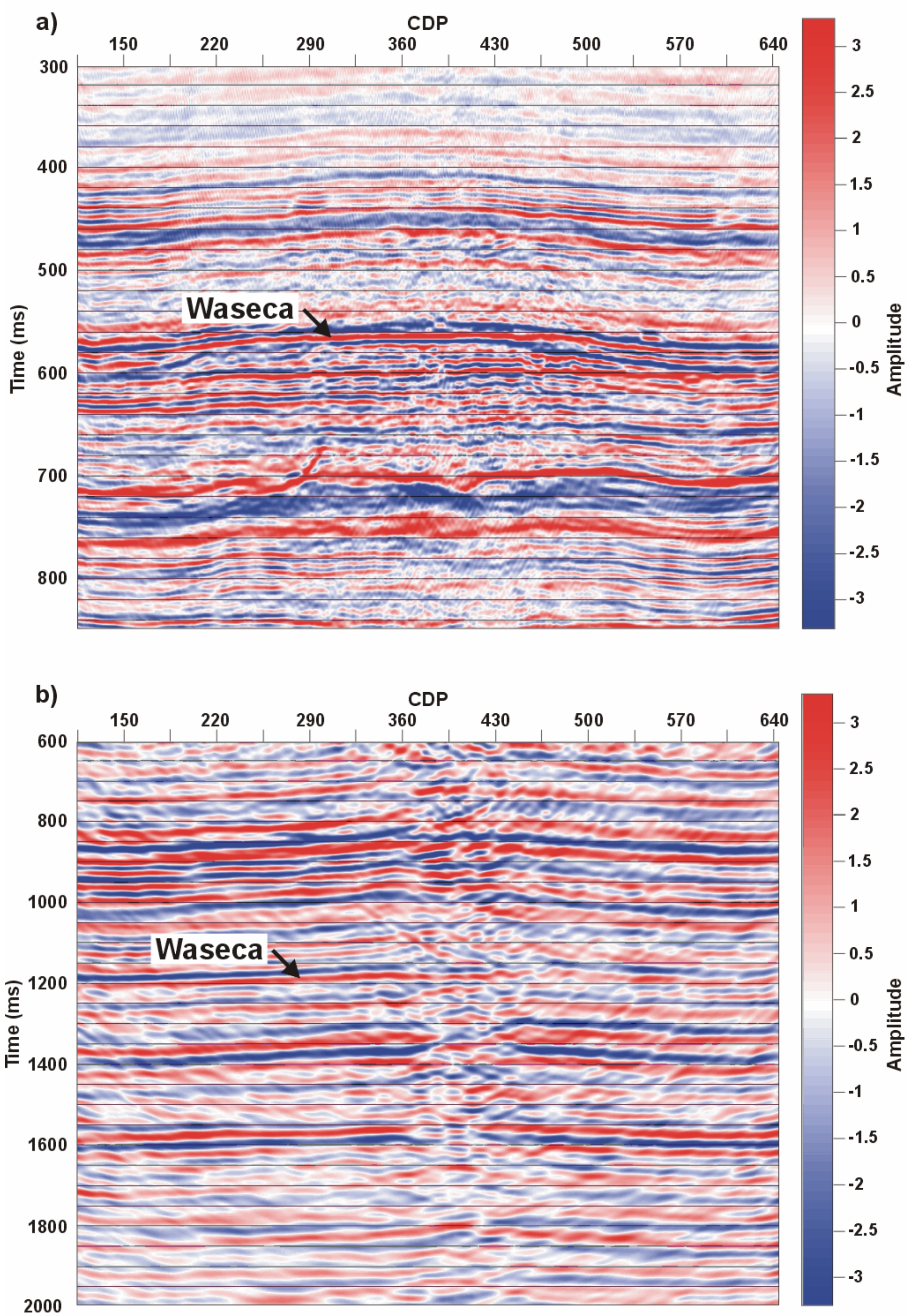

Figure 3.8: a) Mid-range offset vertical-component stacked section and b) radial-component stacked section. Both were post-stack time-migrated.

A common method for correlating P-P and P-S sections is used in the converted-wave processing in this study. This method is an interpretive approach where the P-S time-stretch factor is derived by matching picked events on P-P and P-S sections. A simple relationship used to relate interval V_P/V_S and P-P and P-S traveltimes is summarized as follows (Margrave et al, 1998):

$$\gamma = \frac{\alpha}{\beta} = \frac{2T_{PS}}{T_{PP}} - 1 \tag{3.1}$$

where T_{PP} and T_{PS} equal P-P and P-S two-way travelimes, respectively, between two picked events. Once proper phase corrections are done to the P-P and P-S datasets, this method is reliable for estimating V_P/V_S ratios and thus the P-S time-stretch factors used to correlate the two datasets. The result of correlation using this method is shown in figure 3.9. There are frequency differences between P-P and P-S data. The matching is not great but there are correlations at P-P times of 320 ms, 455 ms, 530 ms, 575 ms, 600 ms, 650 ms, 750 ms, 775 ms and 920 ms.

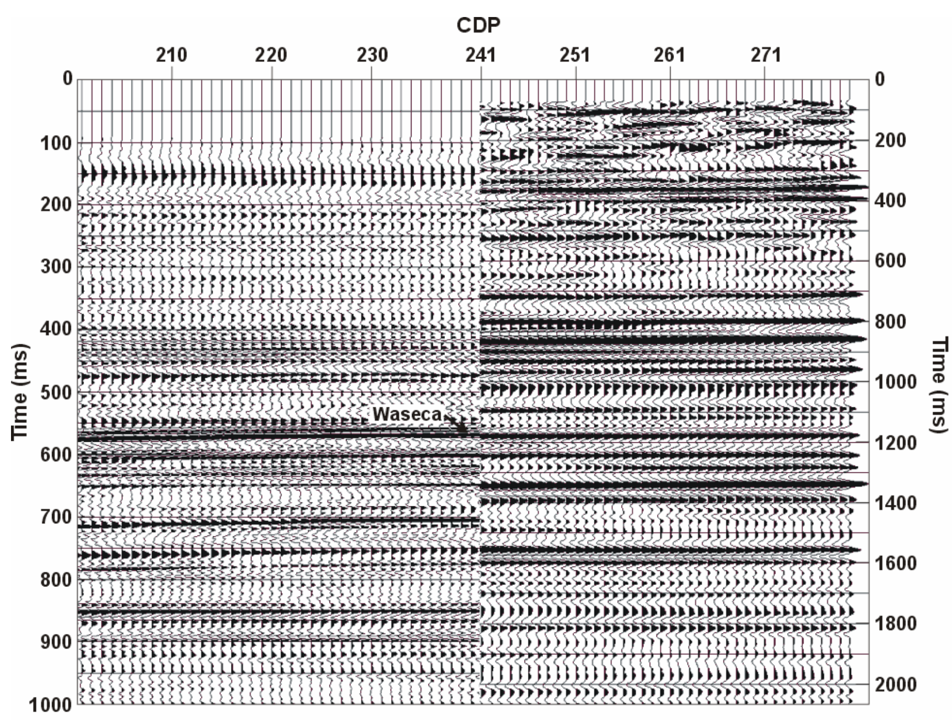

Figure 3.9: Correlation of P-P (CDP 201-240) and P-S (CDP 241-280) stacked sections.

The advantage of this method is that it is completely independent of lithological assumptions such as mudrock line. The disadvantage of this method is the need to rely upon accurate event identification using synthetic seismograms, thus good well control is needed. And because an event is picked on a specific point of phase, these events in P-P and P-S data are difficult to tie in depth.

In this thesis study, the target zone is composed of a relatively simple structure, and in order to restore the top of the zone of interest to the original deposition surface by flattening the datum horizon and to reduce errors in the inversion, a further approximate event correlation is carried out as follows.

The first step is to pick a common, easily identifiable regional horizon that is relatively free of thin-bed tuning effects or phase distortions above the presumed channel zone. An obvious horizon can improve picking accuracy. In this study, the top of the Waseca Formation was picked as shown in figure 3.8.

The second step is to convert P-P and P-S limited-offset data from the time domain to the depth domain (figure 3.10) using interval velocities calculated from P-P and P-S stacking velocities. The inversion is carried out in the depth domain.

The third step is to flatten both P-P and P-S limited-offset depth sections relative to the horizon obtained in step 1 and shift the flattened horizon to the corresponding depth in the well, the calculated attributes of which will be compared to the seismic inversion.

The fourth step is to output limited-offset sections (figure 3.11) relative to the flattened horizon for later use in the joint inversion.

3.4 Synthetic modeling

The wells D15-6, 1A15-6, 3C8-6 and D2-6 shown in figure 3.12 were used to create synthetic P-P seismograms to tie to the P-wave seismic data because they had original sonic and density logs over the Waseca interval. Well D15-6 was drilled in Oct. 1978 and has minor amounts of production (500 m^3). Well 1A15-6 was drilled in Jan/Feb. 2000. Well D2-6 was drilled in Feb. 1981. It was on oil production from 1981-

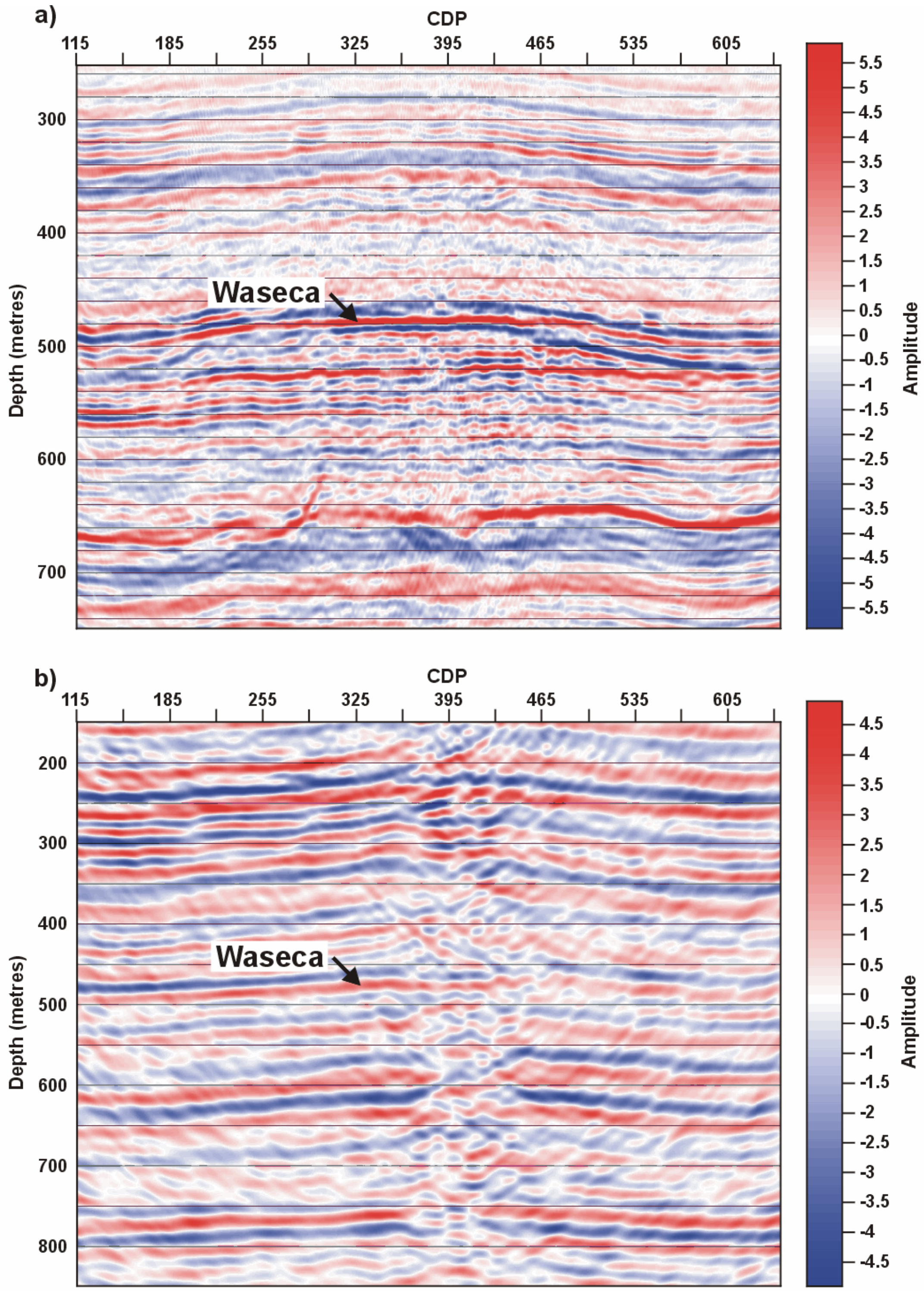

Figure 3.10: a) Vertical and b) radial component mid-range-offset stacked and migrated sections in depth domain. The Waseca top was shifted to the corresponding depth in well 1A15-6.

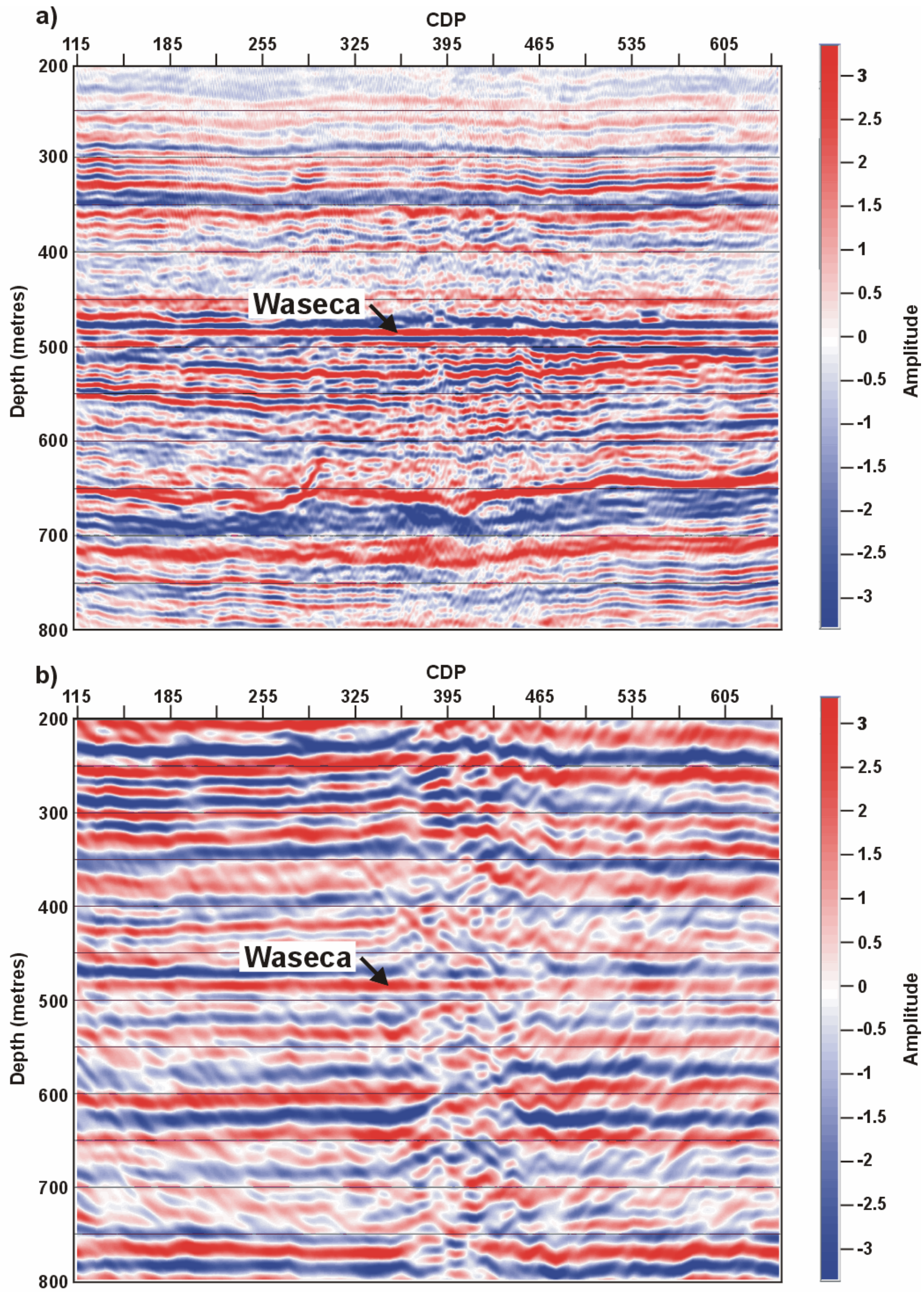

Figure 3.11: a) Vertical and b) radial component mid-range-offset stacked sections with the Waseca top flattened.

1987 and then converted to a steam injector in 1992. 3C-8 was drilled in May/June 1999. It has been used for production and steam injection alternately since Oct. 1999.

There was no steam injection in the first two wells before these 3C-2D seismic data were acquired. But there was steam injection in wells 3C8-6 and D2-6 before the seismic acquisition. There were also some neighboring well-bores that had steam injection prior to the seismic shoot. Well 1A15-6 was also used to tie to the converted-wave (P-S) seismic data because it had a dipole sonic log.

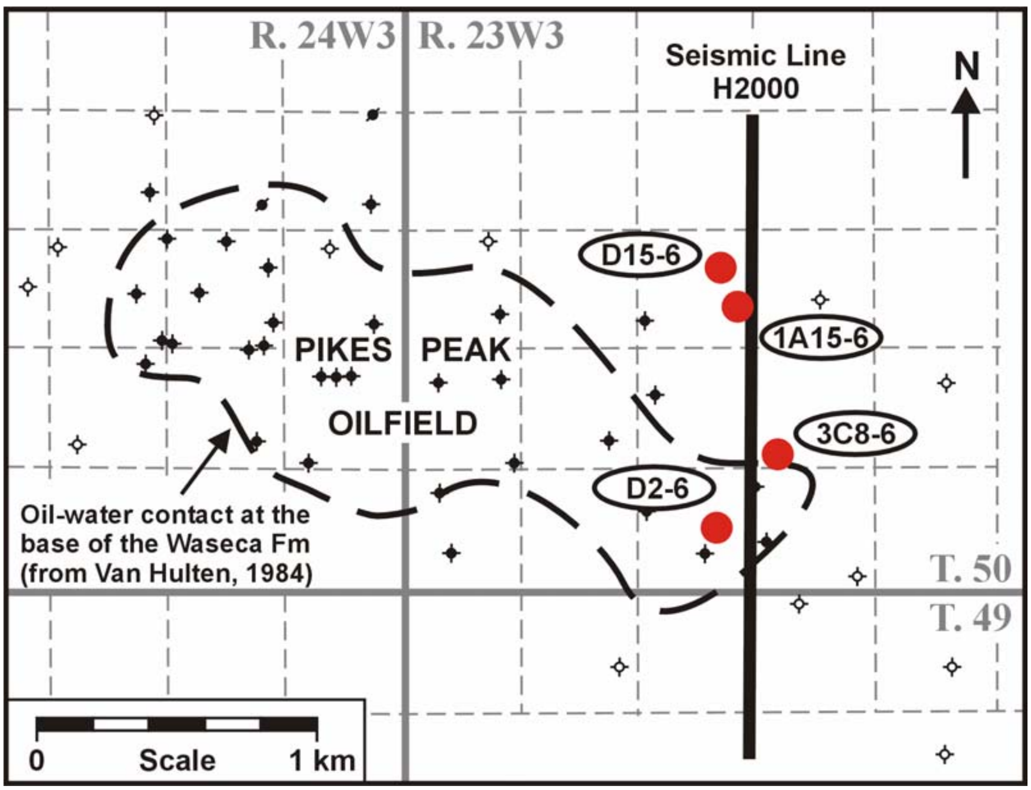

Figure 3.12: Location map of the seismic line and the four wells used in this project.

It is important to consider both the polarity and phase of the input seismic data prior to applying the simultaneous-inversion method. A consistent set of polarity conventions should be maintained between the P-P and P-S seismic data according to the Zoeppritz equations. Brown et al. (2002) pointed out that for the inline geophone (X) in 3-C data acquisition, polarity considerations were complicated by a few factors. One of them is that there is not a 100% consistent relationship between P-P and P-S reflection coefficients (R_{PP} and R_{PS}, respectively) for all possible lithologic interfaces. So Brown et al. (2002) proposed a multicomponent field-polarity standard which could also be called the multicomponent acquisition polarity standard. In this theory, normal polarity is only defined for field records prior to any phase-altering processes for minimum-phase and zero-phase data.

Phase errors are more difficult to predict. In order to decrease the errors in phase and polarity, synthetic seismograms with different phases are created in each of the four wells by raytracing for the traveltimes and using the Zoeppritz equations for the reflection amplitude. The inputs for these seismograms are well logs from the field and the final seismograms are band-limited to match the processed seismic data. Phase rotations from 0° to 180° and from 0° to –180° with an interval of 45° are tested on P-P and P-S synthetic seismograms and compared to the seismic data. Because P-P and P-S synthetic seismograms with 45° and –90° degree phase rotation in well 1A15-6 tie the most of the seismic events, including the events around the zone of interest, the best, as shown in figure 3.13, constant-phase rotation of –45° and 90° were applied to the vertical- and radial-component data, respectively, so as to give an optimal match to the synthetics.

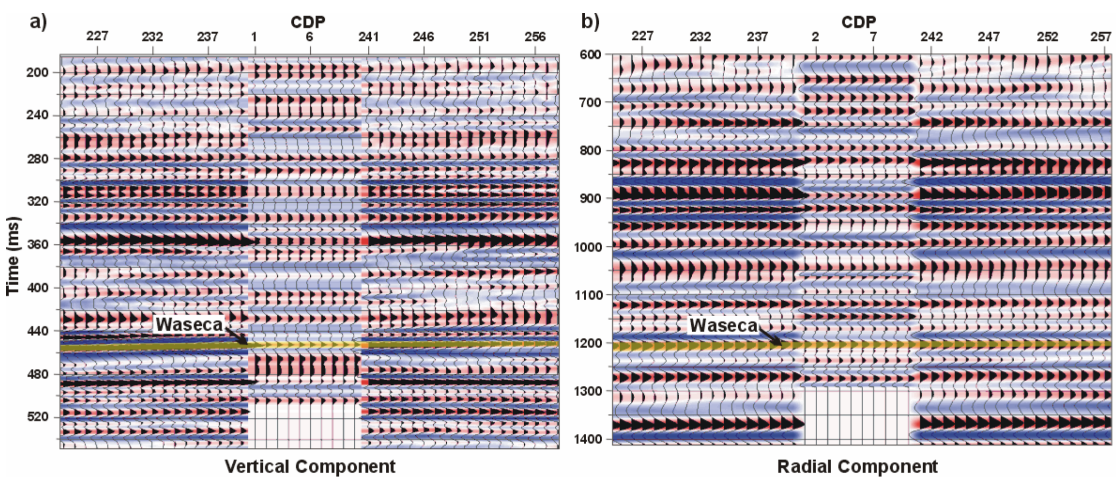

Figure 3.13: a) P-P and b) P-S synthetic seismograms (in the middle of a) and b)) for well 1A15-6 are both initially generated with normal polarity and rotated 45° and –90°, respectively, to tie optimally with the vertical- and radial-component datasets. On both sides of the synthetic seismograms are the seismic traces.

Other phase-rotated P-P and P-S synthetics of well 1A15-6 are compared in figures 3.14 to 3.17. But even after the same bandpass filtering is done, the frequency bands and the wavelets of these synthetics do not match the seismic data very well. Figure 3.18 shows the P-P synthetic seismograms were rotated 45° in well D15-6, 3C8-6 and D2-6 and matched to the vertical-component seismic data at the corresponding CDP positions.

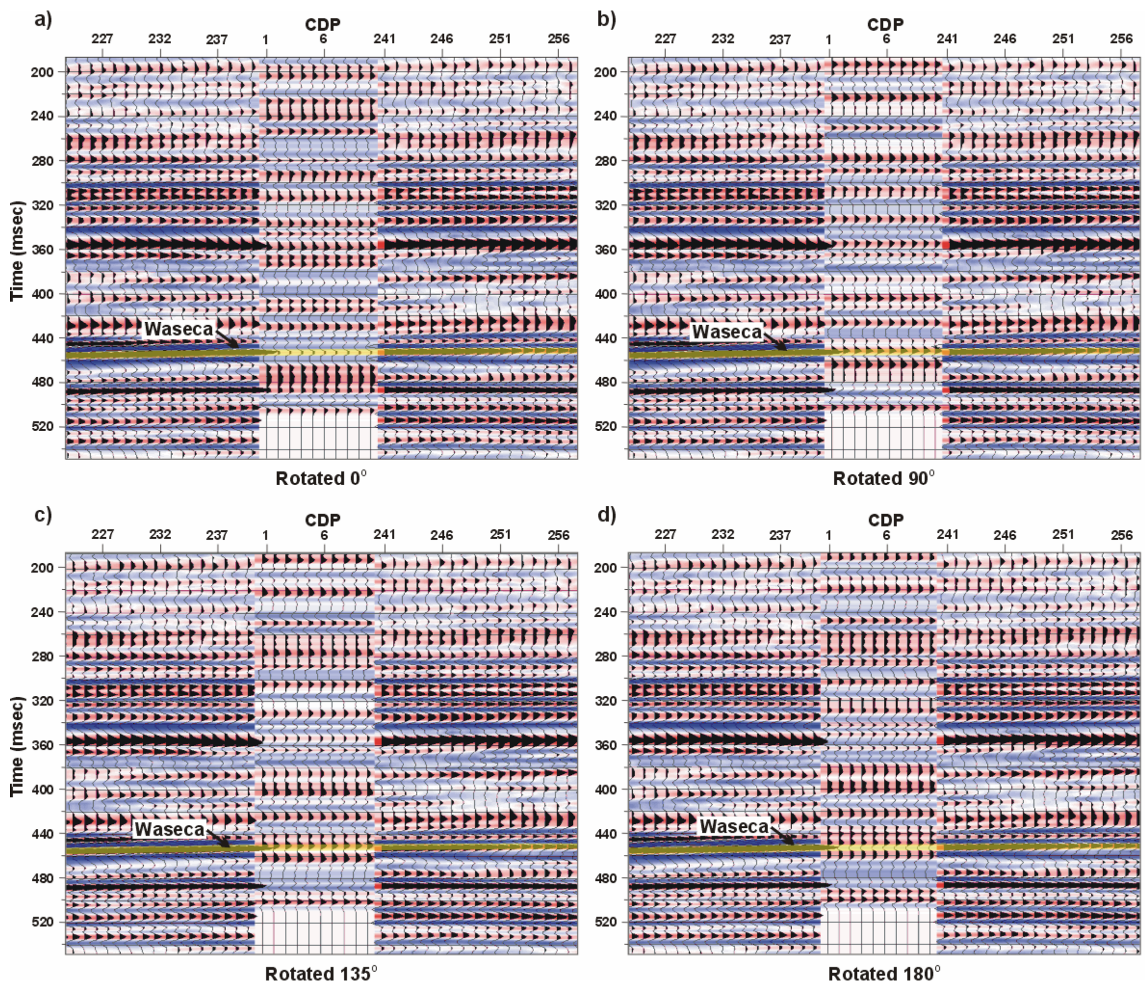

Figure 3.14: P-P synthetics in a), b), c) and d) are phase rotated 0°, 90°, 135° and 180° and compared to the vertical-component data.

3.5 Constructing background velocities

The background velocities include interval P-wave and interval S-wave velocities. They are used to calculate average angles of incidence, reflection and transmission for both the stand-alone P-P and the simultaneous inversions. Thus, it is possible to calculate

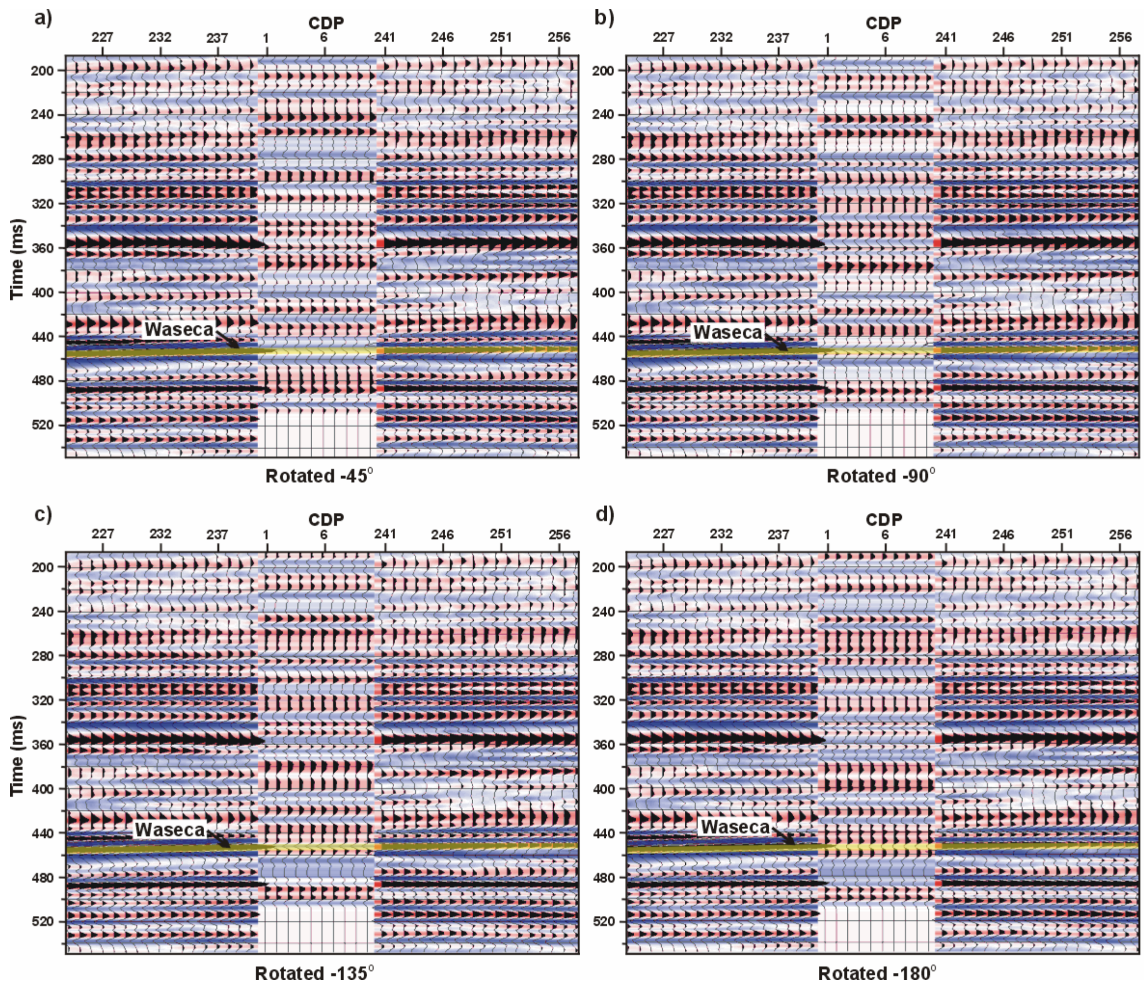

Figure 3.15: P-P synthetics in a), b), c) and d) are phase rotated –45°, –90°, –135° and –180° and compared to the vertical-component data.

the weights for each inversion method. According to the assumption of small changes in the elastic parameters across the interfaces in the first-order Zoeppritz-equation approximation, the background velocities should be highly smoothed. In order to test the sensitivity of joint PP-PS AVO inversion on the Pikes Peak 2-D seismic data, two sets of background velocities as functions of depth were constructed as background velocities and tested in the joint inversion. The interval velocities in depth were also employed in post-stack migration and time-depth conversion.

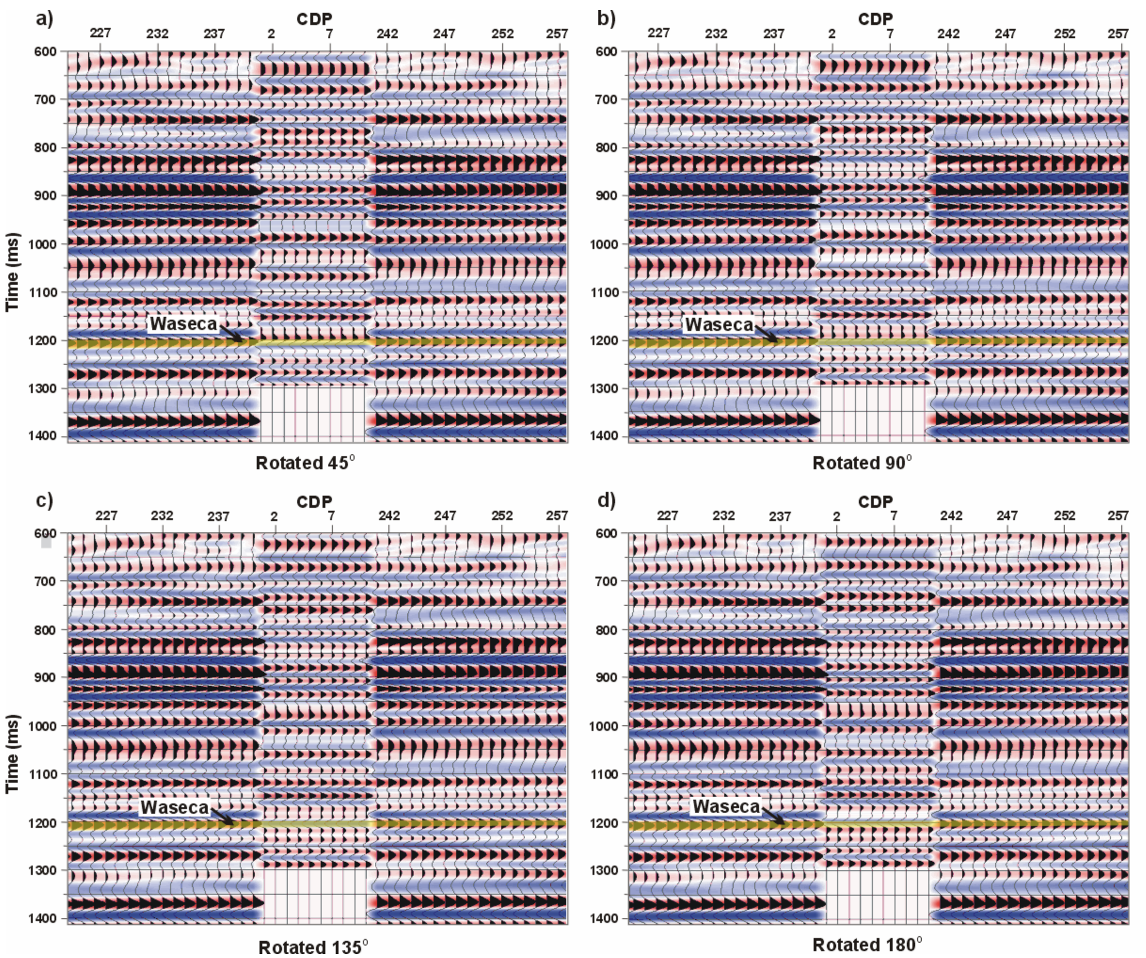

Figure 3.16: P-S synthetics in a), b), c) and d) are phase rotated 45°, 90°, 135° and 180° and compared to the radial-component data.

3.5.1 Interval velocities derived from stacking velocities

The first set of background velocities was derived from stacking velocities. Firstly, velocity analysis was carried out on the vertical- and radial-component (figure 3.19) common-reflection-point gathers to obtain the stacking velocities. The stacking velocities for the vertical component can be regarded directly as P-wave RMS velocities and so they were converted to interval P-wave velocities in time and depth domains immediately. But the stacking velocities for the radial component have to be regarded as converted-wave (P-S) RMS velocities, not S-wave RMS velocities. So a calculation in equation (3.2) (Tessmer and Behle, 1988) was done to obtain the approximate S-wave stacking velocities.

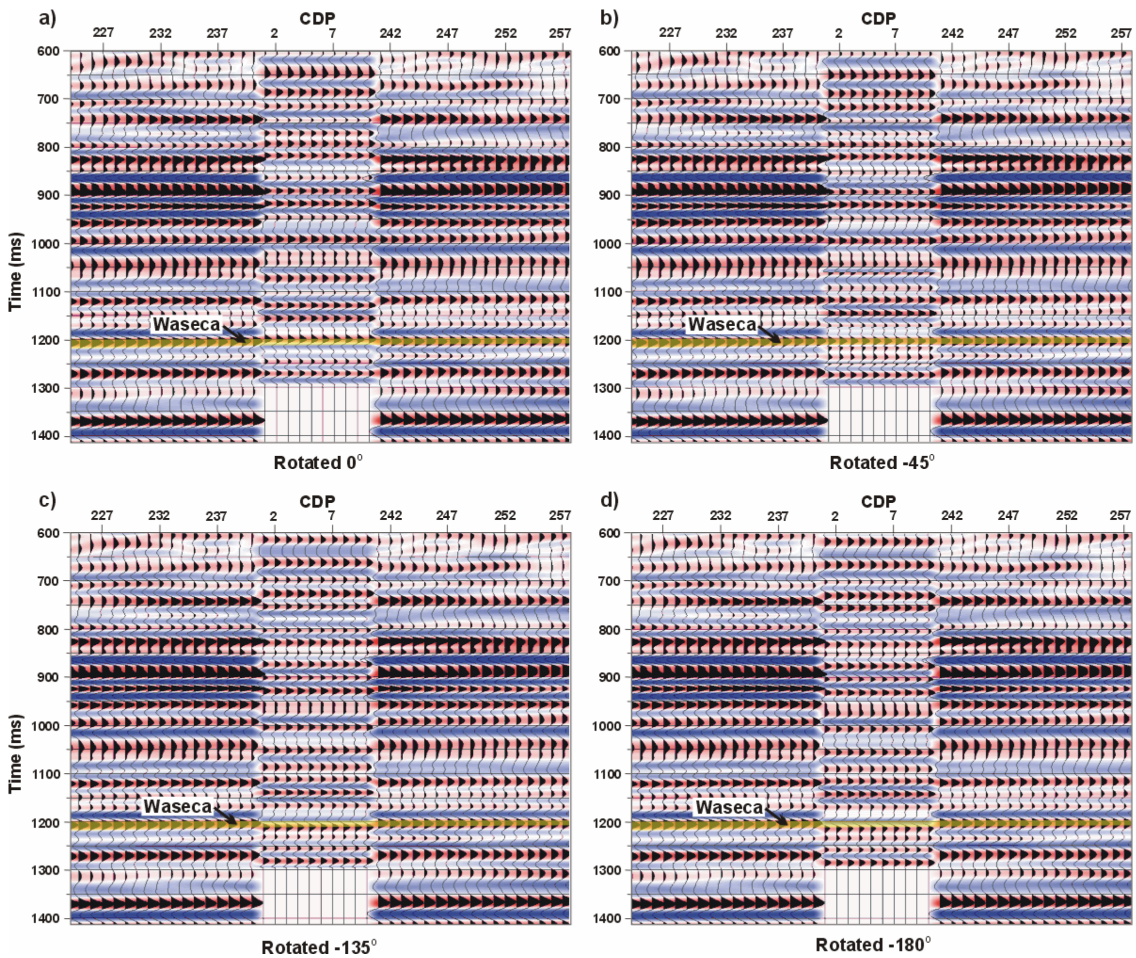

Figure 3.17: P-S synthetics in a), b), c) and d) are phase rotated 0°, –45°, –135° and –180° and compared to the radial-component data.

$$V_{SS}^{stk} \approx \frac{\left(V_{PS}^{stk}\right)^2}{V_{PP}^{stk}} \tag{3.2}$$

where V_{SS}^{stk} is S-wave stacking velocity, V_{PS}^{stk} is converted-wave stacking velocity and V_{PP}^{stk} is P-wave stacking velocity. Once the S-wave stacking velocities are obtained, the interval S-wave velocities can be obtained in ProMAX and applied in time-depth conversion and simultaneous inversion. The interval P-wave and S-wave velocities are shown in figure 3.20.

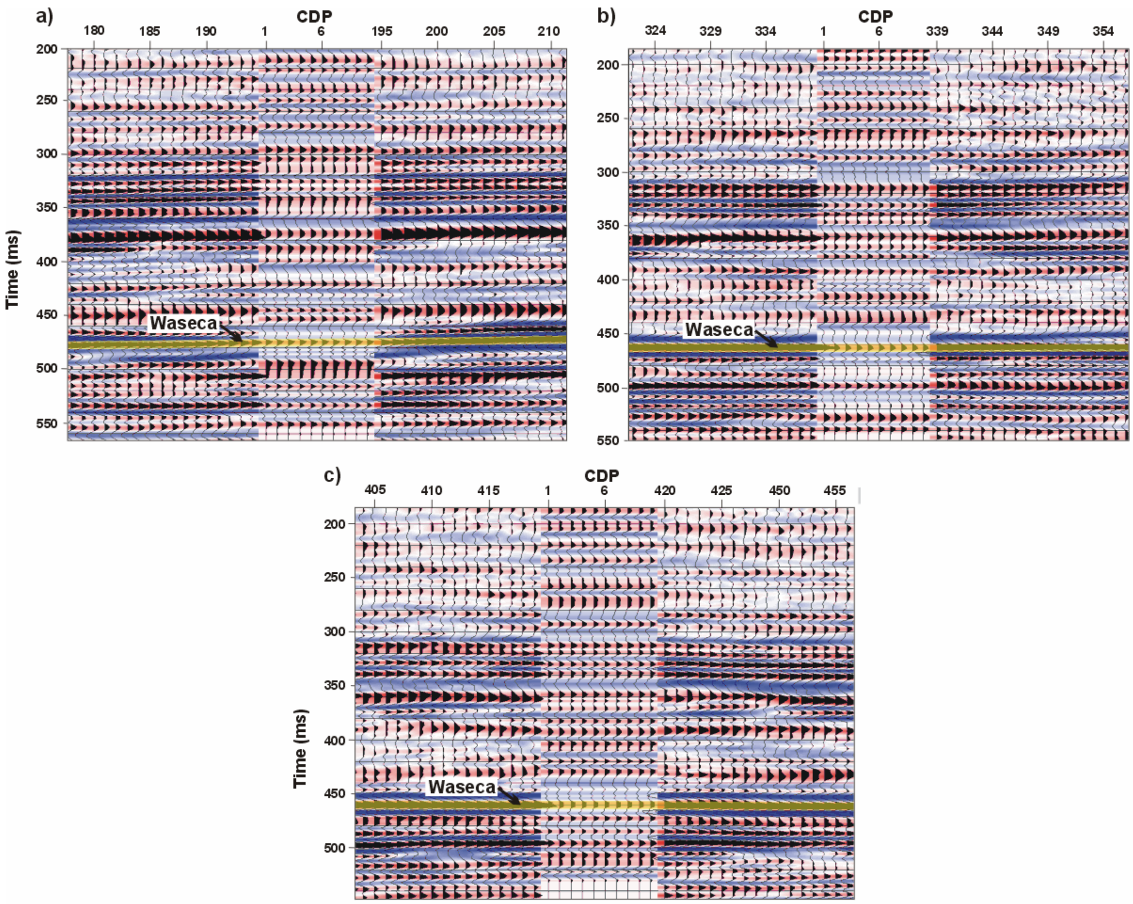

Figure 3.18: Synthetic seismograms in a) well D15-6, b) well 3C8-6 and c) D2-6 are initially generated with normal polarity and rotated 45° to tie optimally with the vertical-component data.

3.5.2 Interval velocities derived from well logs

Well 1A15-6 was used in deriving interval P-wave and S-wave velocities since this is the only well with a dipole sonic. Because the well logging did not start from depth

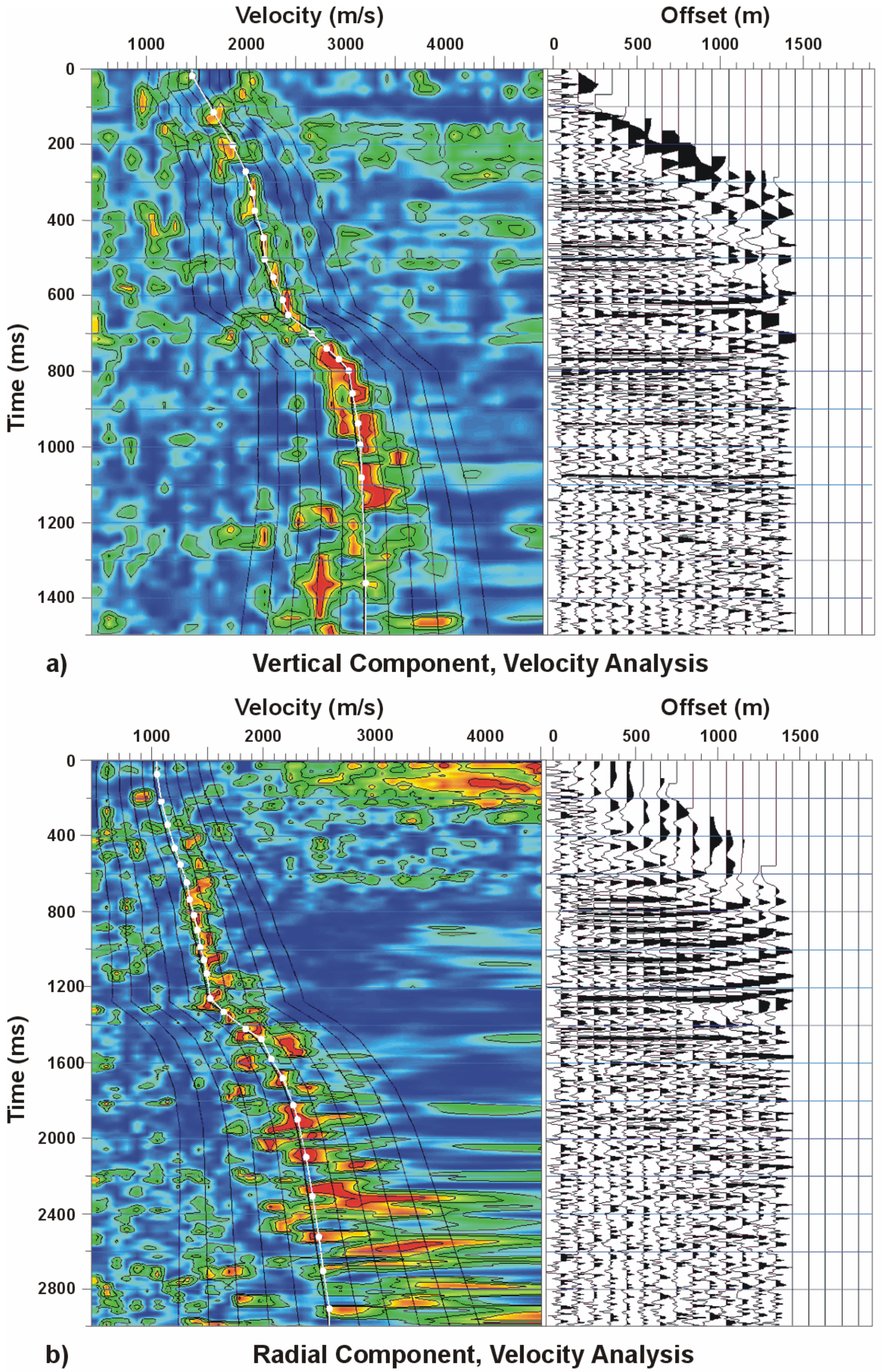

Figure 3.19: Velocity analysis for a) the vertical component and b) the radial component.

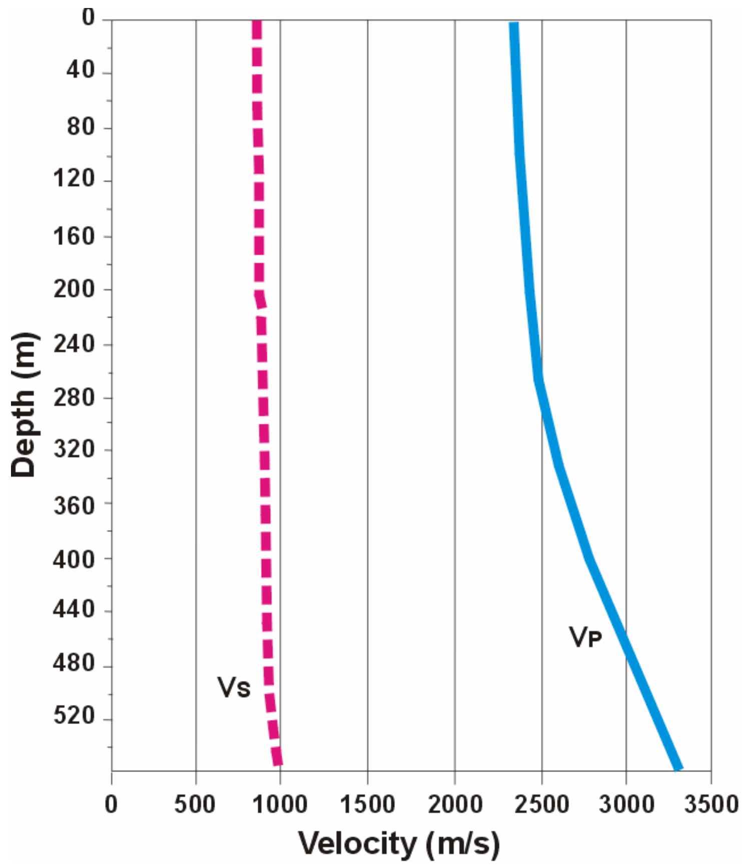

Figure 3.20: Interval P-wave (solid) and S-wave (dash) velocities derived from seismic P-P stacking velocities and P-S interval velocities.

zero, overburden velocities needed to be determined. The linear least-square functions were fitted to the well logs in figure 3.21 and extended to depth zero to obtain optimal overburden velocities.

As we know, well logs have much higher frequencies and much broader frequency bands than seismic data. In order to lower the frequencies of the well logs sothat they would be similar to those of the seismic data, the velocities and densities obtained from the well logs were blocked and correlated with the seismic data (figure 3.22).

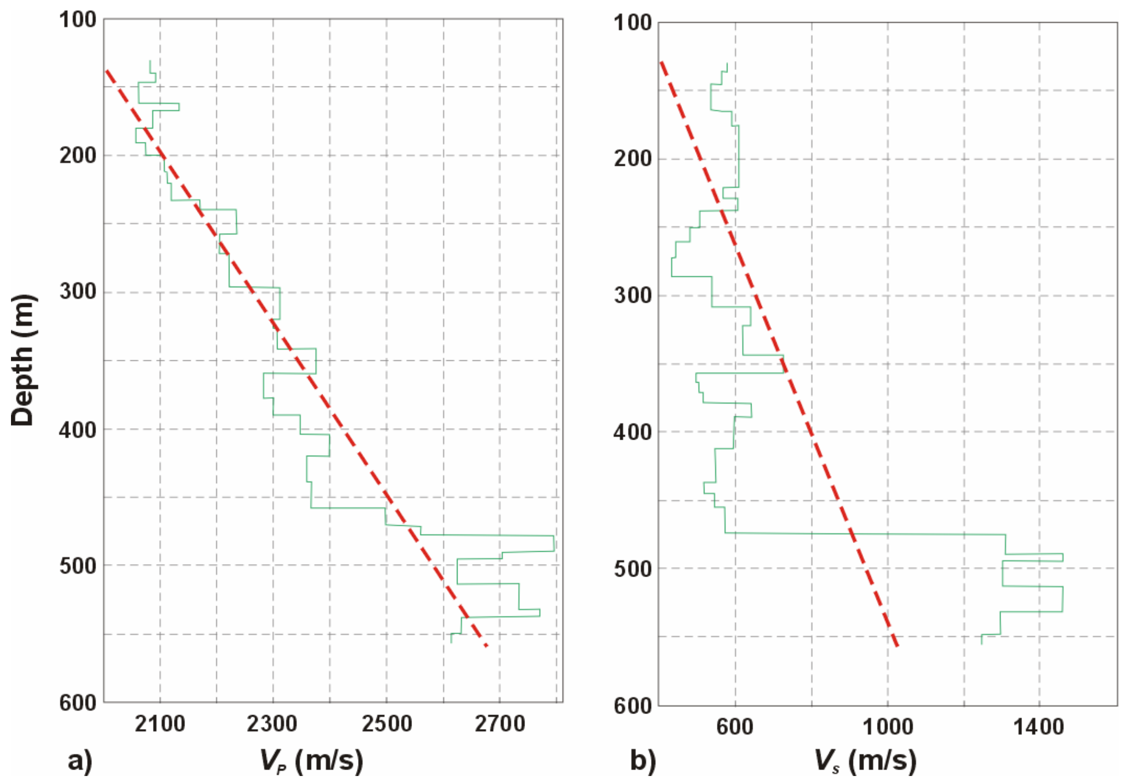

Figure 3.21: Overburden P-wave and S-wave velocities were derived from linear least-square fits to the a) P-wave and b) S-wave velocities in well logs.

The blocking interval is as great as 20 m from the top of the well to depth 450 m since there is no pay zone within this depth range. The pay zone starts at 485 m., we start blocking the well-log curves using an interval that is as fine as 3 m from depth 450 m because there is a dramatic change in P- and S-wave velocity at this depth.

To avoid violating assumptions made in the Zoeppritz-equation approximations, i.e., small elastic changes across a given interface, the blocked interval velocities in depth were smoothed (figure 3.23). Figure 3.24 shows that interval P-wave velocities and S-wave velocities derived from seismic are both greater than the velocities derived from well logs.

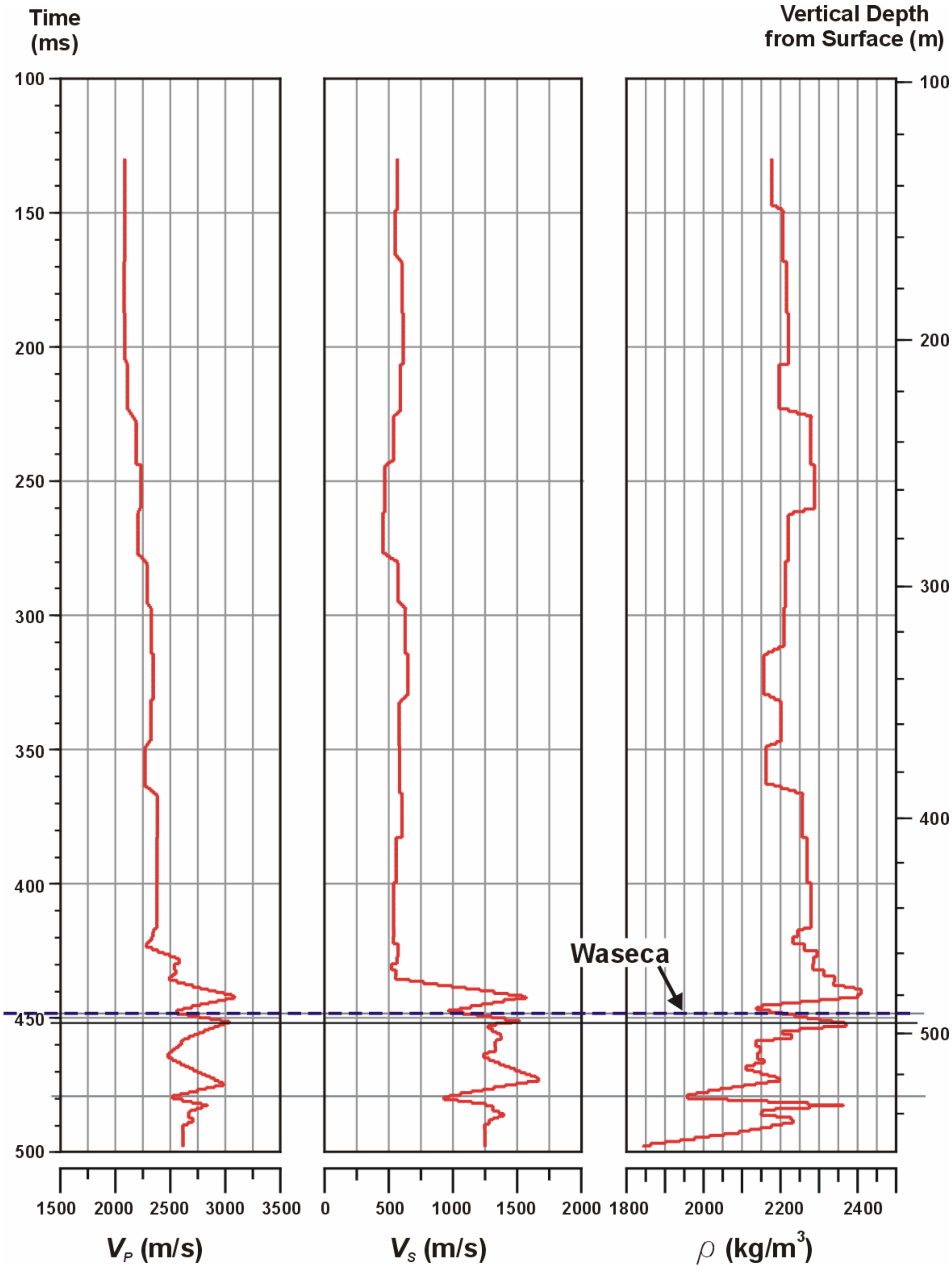

Figure 3.22: Blocked P-wave velocities, S-wave velocities and densities from well 1A15-6. The blocking intervals are 20 m from the top of the well to a depth of 450 m and 3 m from 450 m to the bottom of the well.

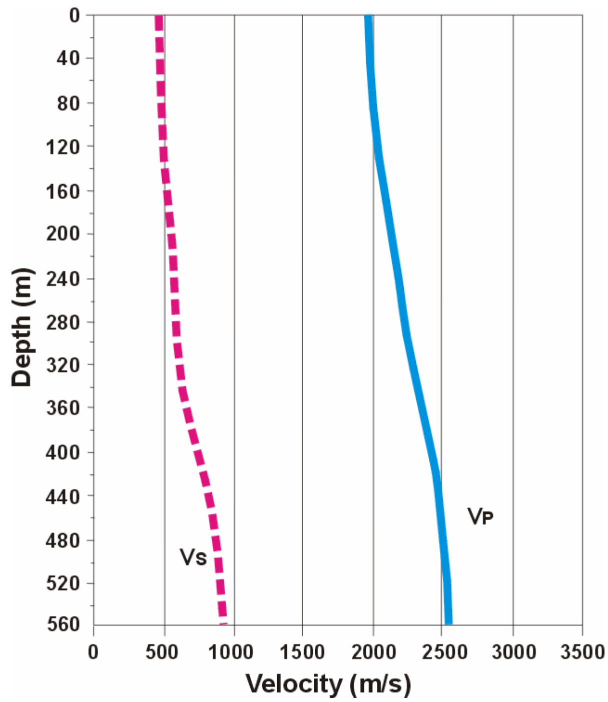

Figure 3.23: Smoothed interval P-wave (solid) and S-wave (dash) velocities derived from well 1A15-6.

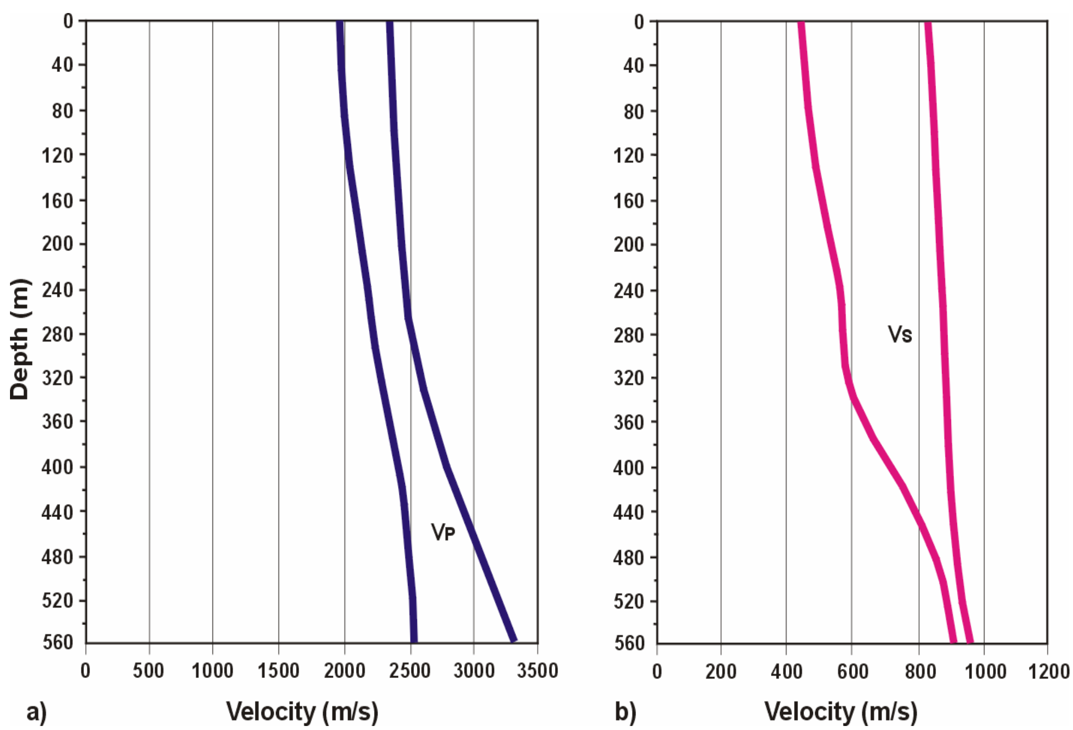

Figure 3.24: a) P-wave and b) S-wave interval velocities derived from seismic are greater than those from well logs.

3.6 Restoration of regional P-P and P-S reflection behavior with offset

True amplitude recovery during seismic processing is not perfect for AVO analysis. In fact, to stack out undesirable noise and reduce the variations in amplitude, trace equalization and time-variant scaling are almost always required before stacking so the extremely strong noise does not dominate the stack (figure 3.25 and figure 3.26). Trace equalization is a process in which all traces are adjusted to have the same RMS power level. Time-variant scaling computes and applies a time-variant scaling function so that the variations in amplitude are reduced. This is not a great problem for P-P AVO analysis because the regional AVO behavior is nearly constant. However, for P-S data the regional AVO behavior is roughly sinusoidal with zero amplitude at zero offset and a maximum at some intermediate offset. Hence, it is necessary to attempt to restore the regional AVO.

For this purpose, synthetic seismograms were generated (figure 3.27) by raytracing for the traveltimes and using the Zoeppritz equations for the reflection strength. The input for these seismograms consisted of well logs from the field. The final seismograms were band-limited to match the processed seismic data. In each offset range, the RMS amplitude was calculated to obtain the average expected normalized amplitude values (figure 3.28).

Because the hydrocarbons in the zone of interest cause dramatic changes in velocity and density, only the parts above the production zone in each sonic and density log were used in the RMS amplitude calculation. When a joint PP-PS AVO inversion is being carried out in ProMAX, a table of these RMS amplitude values is created as scale factors by interpolation for all offsets. So the supplied RMS amplitude values need not correspond to actual trace-header offsets, but only to fall within the range of offsets for the input data set.

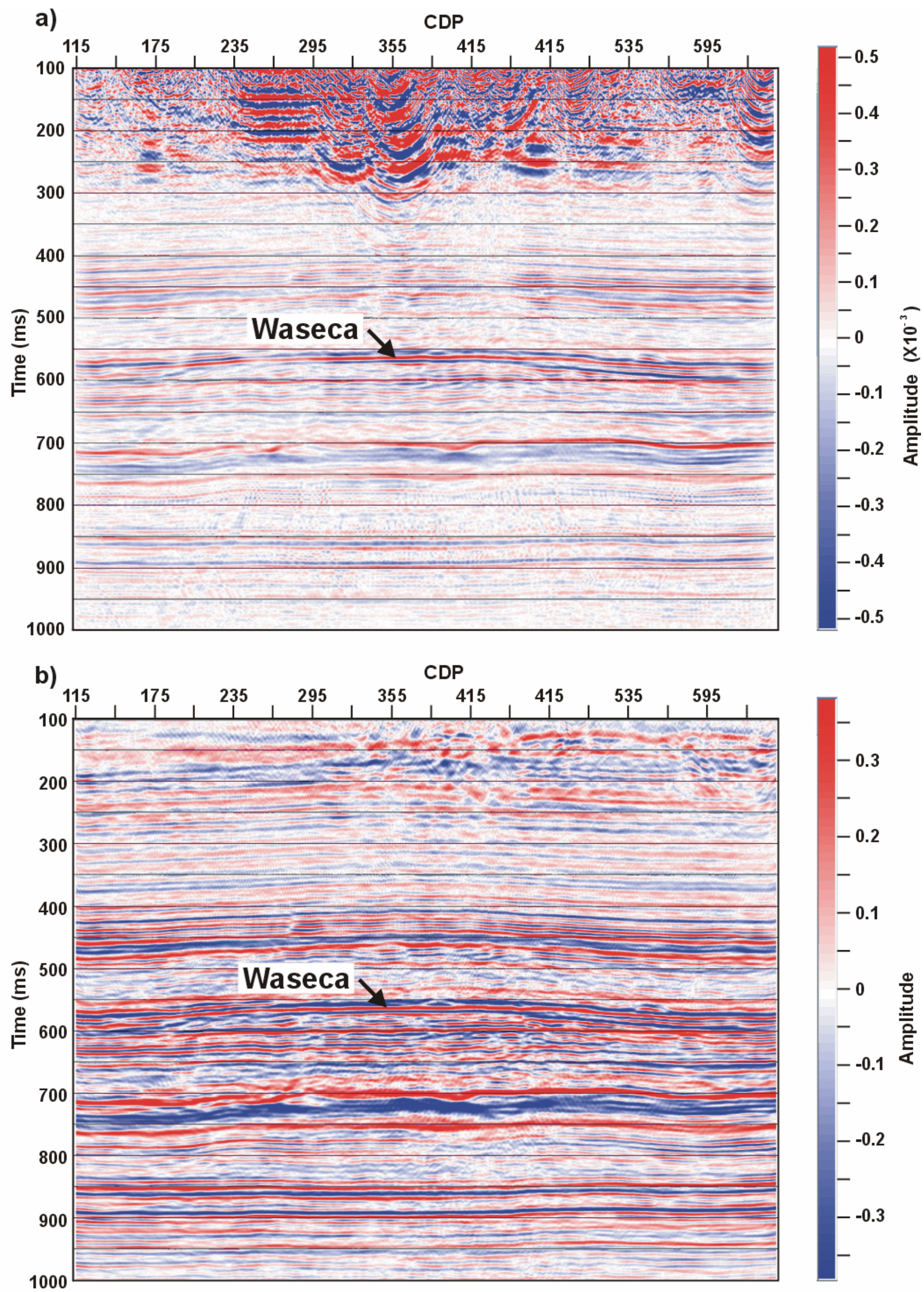

Figure 3.25: P-P stacked section a) without time-variant scaling or trace equalization and b) with both time-variant scaling and trace equalization.

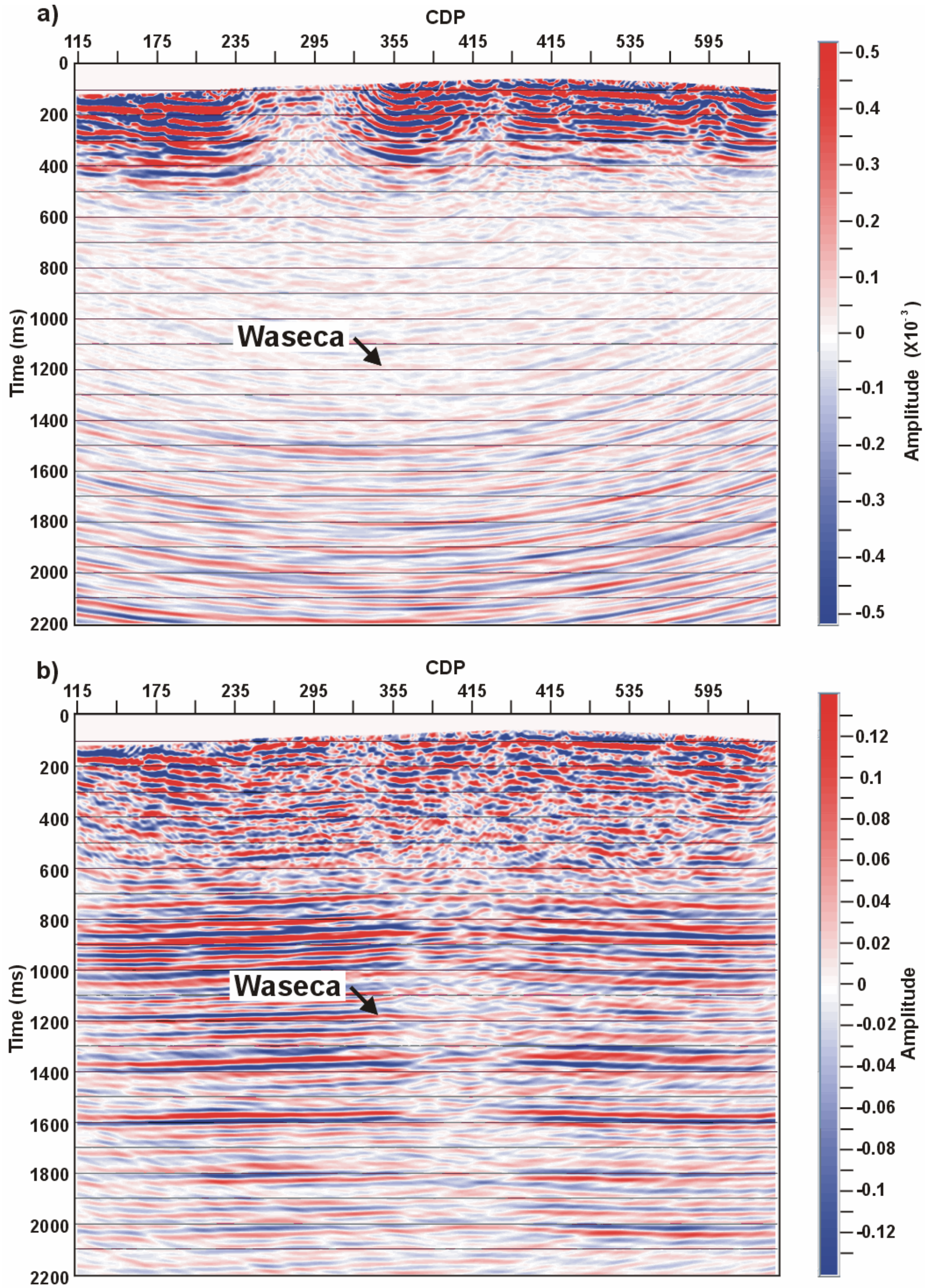

Figure 3.26: P-S stacked section a) without time-variant scaling or trace equalization and b) with both time-variant scaling and trace equalization.

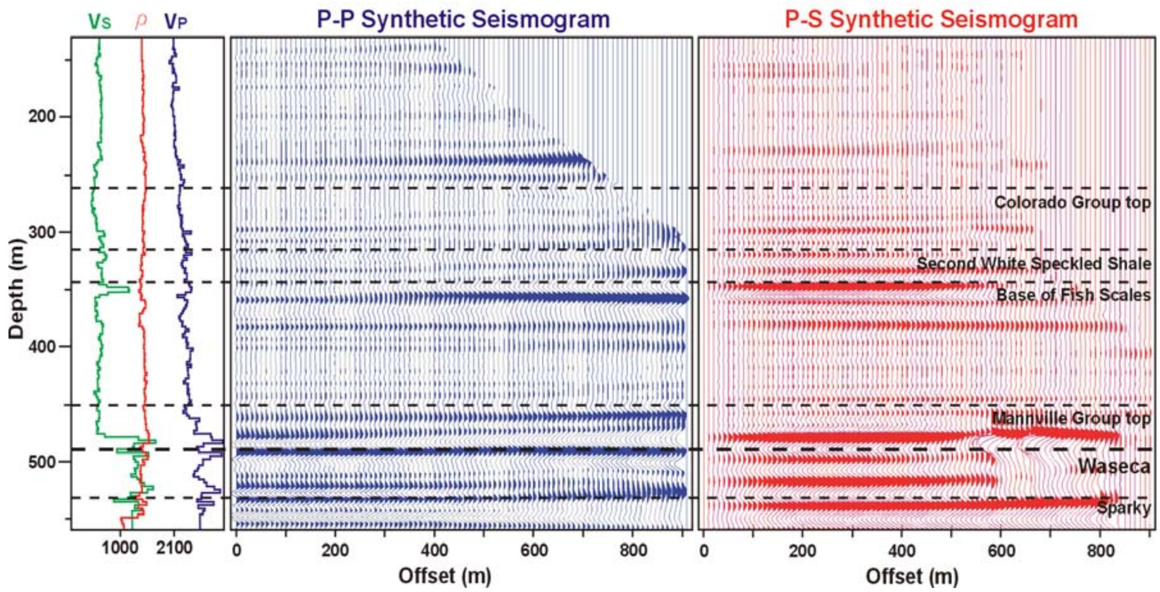

Figure 3.27: Well 1A15-6 P-P and P-S synthetic seismograms used in calculating the RMS amplitude values over a range of offsets.

The processed data were then adjusted to have the same RMS amplitude as the synthetics to represent the stacked P-P and P-S response over these offsets by multiplication by a different scalar for each offset according to the following formulae (adapted from Larsen 1999):

$$R_{PP}(t,h) = \frac{\int_0^{T_{max}} \left| S_{PP}^{\,model}(t',h) \right| dt'}{\int_0^{T_{max}} \left| S_{PP}^{\,data}(t',h) \right| dt'} S_{PP}^{\,data}(t,h) \tag{3.3}$$

$$R_{PS}(t,h) = \frac{\int_0^{T_{max}} \left| S_{PS}^{\,model}(t',h) \right| dt'}{\int_0^{T_{max}} \left| S_{PS}^{\,data}(t',h) \right| dt'} S_{PS}^{\,data}(t,h) \tag{3.4}$$

where $R_{PP}(t,h)$ and $R_{PS}(t,h)$ are the corrected reflection coefficients at a given time t and offset h, $S_{PP}^{data}(t,h)$ and $S_{PS}^{data}(t,h)$ are the reflection coefficient inputs from a trace-equalized time sample, and $S_{PP}^{model}(t,h)$ and $S_{PS}^{model}(t,h)$ are calculated model-based reflection coefficient amplitudes from SYNTH algorithm. Each trace as a result has the same time-averaged amplitude as the synthetic.

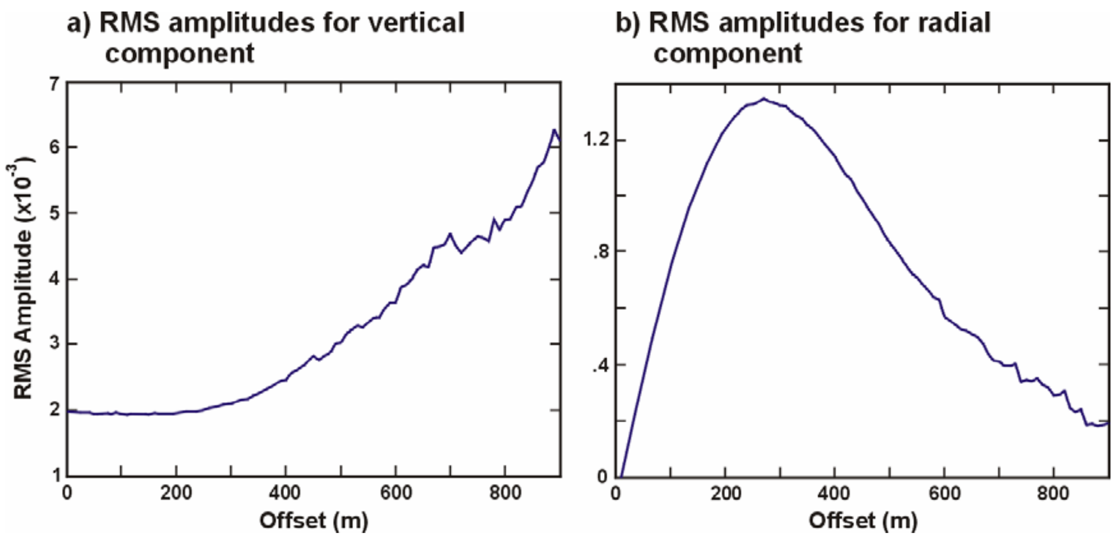

Figure 3.28: RMS amplitudes versus offsets for (a) vertical and (b) radial components.

Up to this stage, the five P-P and five P-S 2-D volumes can be considered as band-limited estimates of R_{PP} and R_{PS}. Because they were converted to depth domain relative to the top of the zone of interest, horizons taken from these volumes just beneath the reference depth should correspond to the same stratigraphic level. The weighted-stacking method was then implemented by weighting and summing these horizons at each desired depth. Specifically, estimates of fractional P-impedance contrast, $\Delta I/I$, and fractional S-impedance contrast, $\Delta J/J$, were produced.

3.7 Maximum angle of incidence

In the module of joint PP-PS AVO inversion in ProMAX, the maximum angle of incidence determines the maximum allowable incidence angle to use in constructing the parameter and coefficient tables. When maximum offset range is 759 m for P-P datasets and 852 m for P-S datasets, the maximum angles of incidence at the target depth (approximately 485 m) do not exceed 39° for P-P datasets and 42° for P-S datasets. Meanwhile, because the P-S synthetic model shows that the smallest critical angle among the four wells at the target depth for P-S datasets is 43° and attributes $\Delta J/J$ and

$\Delta(\lambda/\mu)/(\lambda/\mu)$ are more dependant upon P-S reflection coefficients, the maximum angle of 41° is used in the inversion of $\Delta J/J$ and $\Delta(\lambda/\mu)/(\lambda/\mu)$. The P-P synthetic seismogram shows that the critical angle at the target depth is much greater. Because the inverted $\Delta I/I$ and $\Delta(\lambda\rho)/\lambda\rho$ are affected more by noise when the angle of incidence exceeds 35°, 35° is used in the inversion of these two attributes.

3.8 Chapter summary

In this chapter, following the Pikes Peak geological overview, the data preparation for the joint P-P and P-S AVO inversion was demonstrated. In general, there were four major stages corresponding to four sets of input parameters for the joint inversion. The first two stages were to create five P-P and P-S limited-offset stacked sections. The important procedures were to arrange five limited-offset bins for both P-P and P-S seismic data and convert the stacked sections into depth domain. The third stage was to restore regional reflectivity behavior of P-P and P-S seismic data with offset. This is carried out by adjusting the stacked P-P and P-S sections to have the same amplitudes as the RMS amplitude values calculated at each offset range in P-P and P-S synthetic seismograms. The last major stage was to create interval P- and S-velocities for the joint inversion. The interval velocities were derived from seismic and well logs, and they will be further tested and compared in chapter four.

CHAPTER 4

CORRELATION OF SEISMIC INVERSION AND WELL LOG COMPUTATION

4.1 Introduction

In this thesis, in order to test how effective the method of joint PP-PS AVO inversion is, especially in the zone of interest shown in figure 4.1, correlations of the results from the simultaneous inversion and P-P stand-alone inversion with the attribute estimates calculated from well logs were conducted.

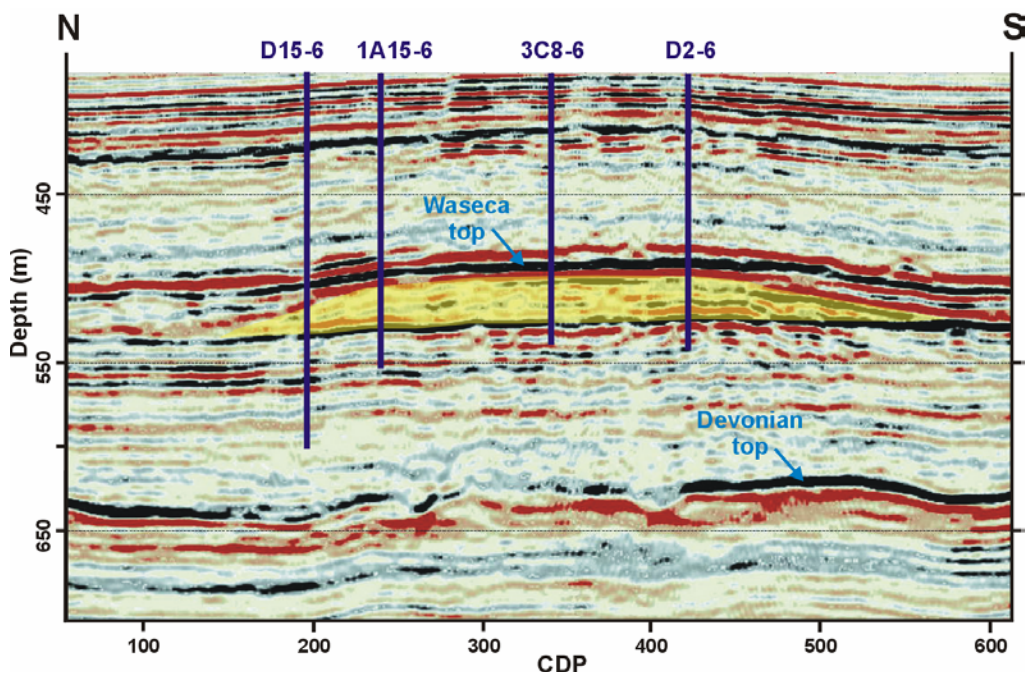

Figure 4.1: The Waseca Fm zone of interest (in yellow) and the four wells used in this thesis.

4.2 Calculation of fractional impedance contrast from well logs

Since the frequencies of well-log data are much higher than those of seismic data, the well logs must be smoothed and downsampled (figure 4.2) to be directly compared with the seismic data. First, the well-log sampling interval (dz_2) is increased by local averaging and decimation. The well logs were averaged over 4-m and 2-m length scales for better P and S impedances correlation with the results from seismic inversion. Second, the fractional impedance (P and S) contrasts are generated from these downsampled data according to equations (4.1) to (4.2). Fractional $\lambda\rho$ contrast, $\Delta(\lambda\rho)/\lambda\rho$, and fractional λ/μ contrast, $\Delta(\lambda/\mu)/(\lambda/\mu)$, can be calculated according to equations (2.5) to (2.6).

Fractional P-wave impedance contrast: $$\frac{\Delta I}{I}=\frac{2(I_2-I_1)}{I_2+I_1} \tag{4.1}$$

Fractional S-wave impedance contrast: $$\frac{\Delta J}{J}=\frac{2(J_2-J_1)}{J_2+J_1} \tag{4.2}$$

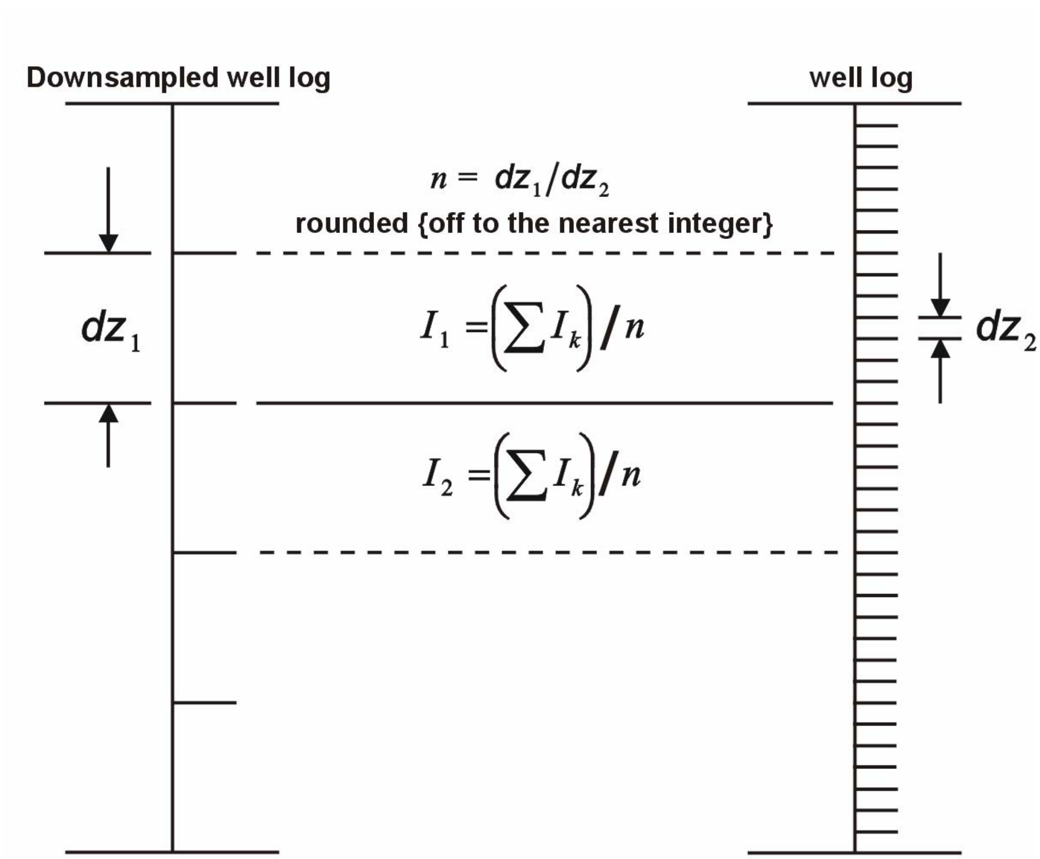

Figure 4.2: An example of how the well log is downsampled to calculate fractional P-wave impedance contrast.

4.3 Filtering of well-log computation

Despite the fact that the well logs were downsampled, the four attributes calculated according to equations (4.1) to (4.2) directly from the well logs have wider frequency bands and much higher frequency content than those obtained from seismic inversion. For example, figure 4.3a) shows the spectrum of fractional acoustic impedance $\Delta I/I$ resulting from the joint PP-PS AVO inversion. Figure 4.3b) shows the spectrum of fractional acoustic impedance directly calculated from well 1A15-6 according to

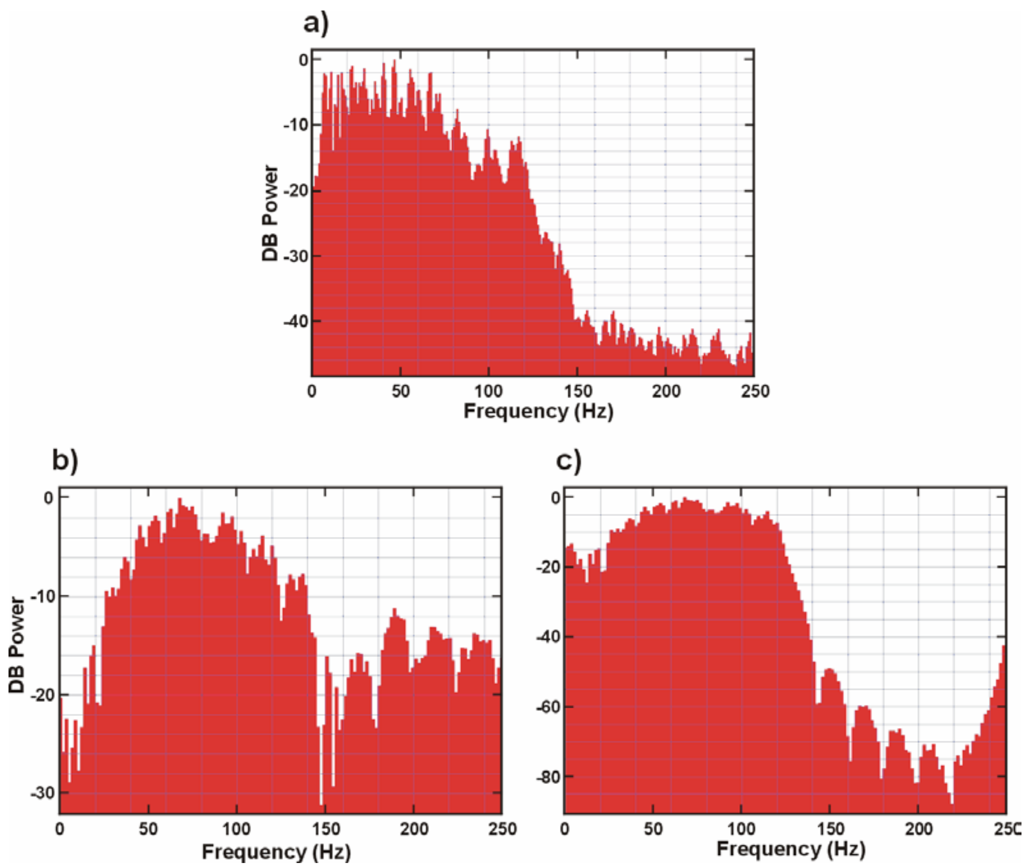

Figure 4.3: The frequency band of fractional acoustic impedance contrast $\Delta I/I$ of b) direct well-log computation according to equation (4.1) is much wider and contains much higher frequencies than $\Delta I/I$ a) from joint inversion. After bandpass filtering, the frequency content of c) well-log computation matches joint inversion better.

equation (4.1), which is quite different from what is shown in figure 4.3a). In order to correlate the well-log computation with the seismic inversion, the well-log computation was bandpass-filtered (figure 4.3c) in the time domain. They were then converted back to depth after the filtering by the same average velocity used in the previous depth-time conversion. The bandpass filter was chosen according to the frequency band of $\Delta I/I$ resulting from the seismic inversion and how well the events of the filtered well-log computation would tie those from the seismic inversion. The use of interval velocities in the time-depth conversion and depth-time conversion would provide very similar results.

4.4 Comparison of simultaneous inversion and P-P stand-alone inversion

The objective of P-P stand-alone inversion is simply to examine the case of a P-P reflection and to extract lithology and pore-fluid parameters from P-P seismic data only. In this case, all weights and reflectivities except weights in P-P reflectivity are set to zero. However, the P-P weights for P-P only inversion are different from the P-P weights for joint PP-PS inversion. In order to decide whether joint PP-PS AVO inversion is effective and how effective it is, the results from joint seismic inversion and P-P stand-alone inversion are correlated to the direct well-log computations (figures 4.4-4.19). The background velocities used in the time-depth conversion and inversions are the interval P and S velocities derived from the dipole well 1A15-6. The optimal depth shifts applied to the P-S data in the simultaneous inversion for $\Delta I/I$, $\Delta J/J$, $\Delta(\lambda\rho)/\lambda\rho$ and $\Delta(\lambda/\mu)/(\lambda/\mu)$ are 0 m, –5 m, 0 m and –1 m, respectively. No horizon is flattened in either simultaneous or P-P stand-alone inversion.

Generally, the correlation between seismic inversion and well-log computation for wells D15-6, 1A15-6, 3C8-6 and D2-6 is fairly good around the zone of interest. In comparison, the results of P-wave-only inversion are similar for $\Delta I/I$ and $\Delta(\lambda\rho)/\lambda\rho$ but quite different for $\Delta J/J$ and $\Delta(\lambda/\mu)/(\lambda/\mu)$. It seems that the joint-inversion estimates of $\Delta J/J$ and $\Delta(\lambda/\mu)/(\lambda/\mu)$ are more coherent than those from P-wave-only inversion but also of lower resolution. I do not yet know the reason for this reduced bandwidth but speculate that it is a consequence of the lower bandwidth of the P-S data. Despite this lower bandwidth, the $\Delta J/J$ and $\Delta(\lambda/\mu)/(\lambda/\mu)$ estimates from joint inversion tie to the well control better than those from P-P only.

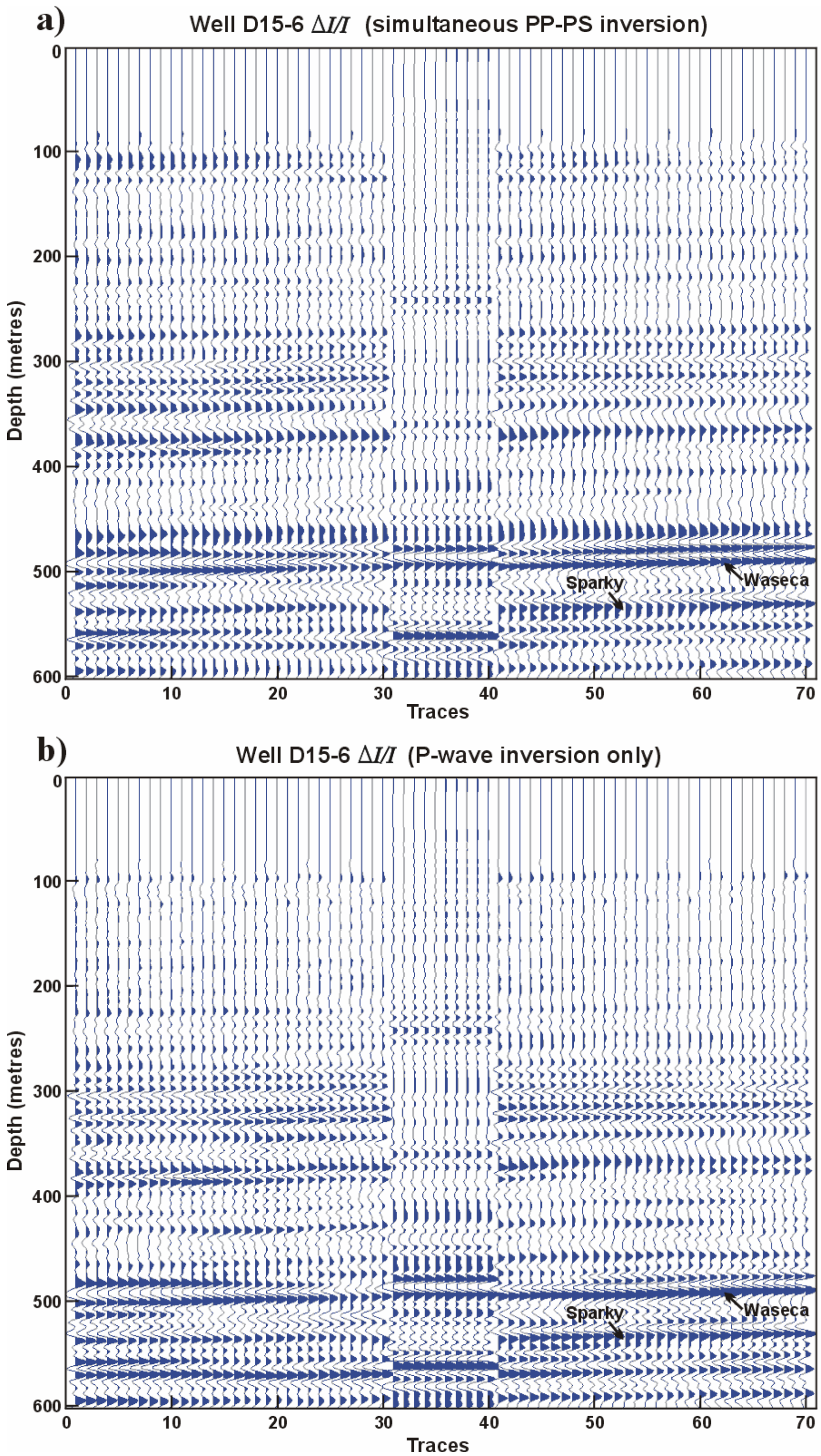

Figure 4.4: Comparison of $\Delta I/I$ from D15-6 well-log computation with $\Delta I/I$ from a) the simultaneous inversion and b) P-P stand-alone inversion.

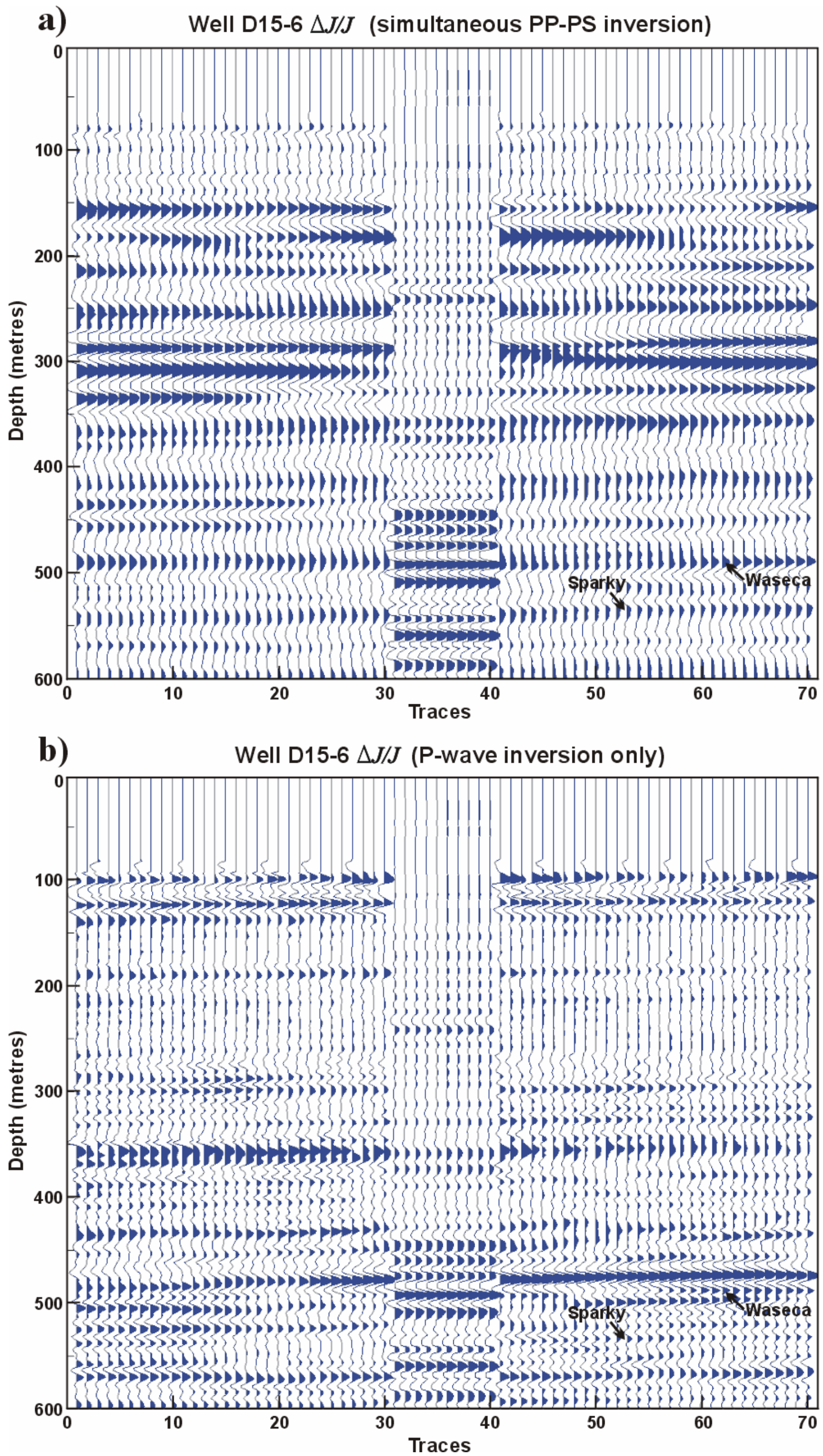

Figure 4.5: Comparison of $\Delta J/J$ from D15-6 well-log computation with $\Delta J/J$ from a) the simultaneous inversion and b) P-P stand-alone inversion.

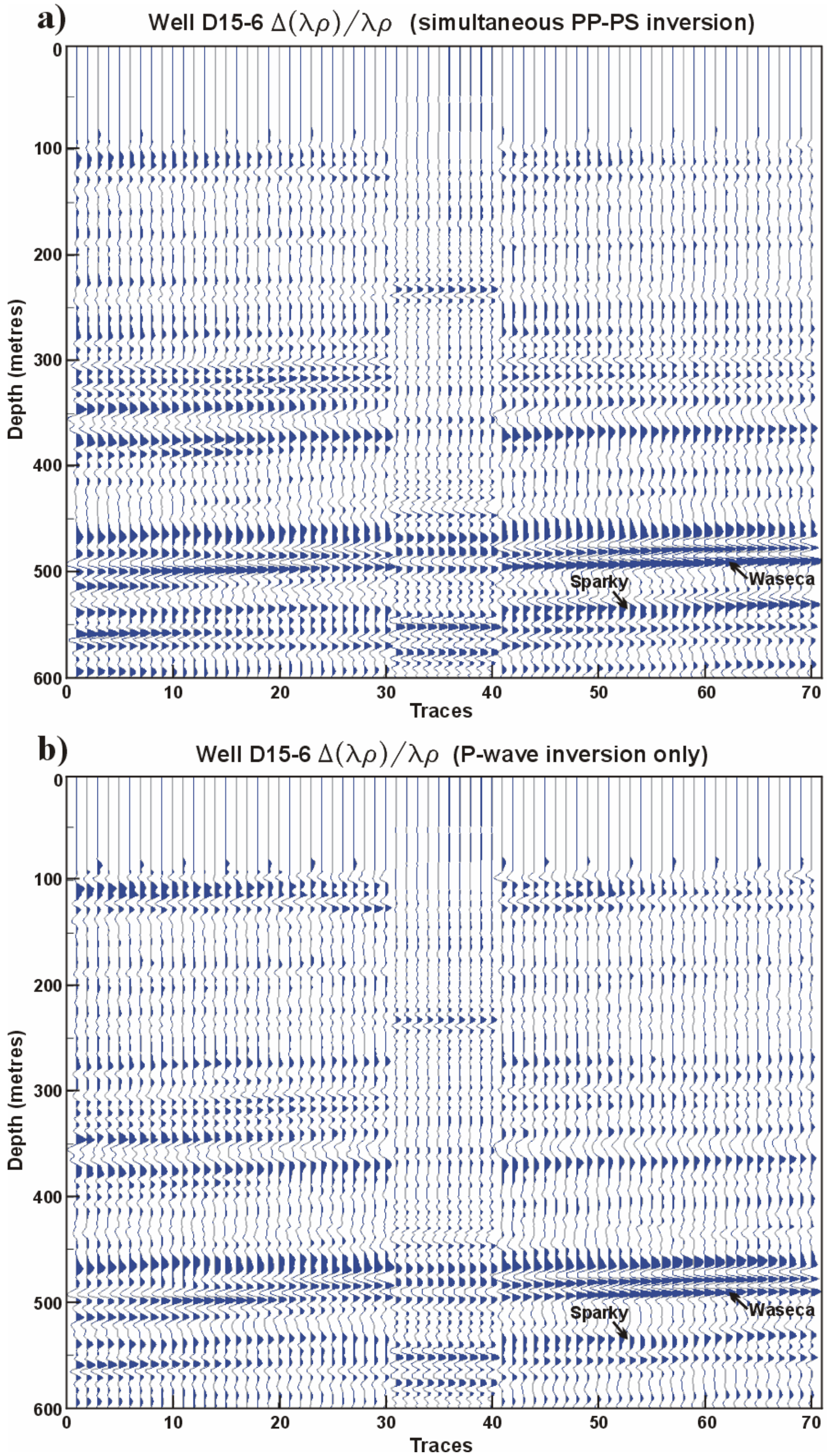

Figure 4.6: Comparison of $\Delta(\lambda\rho)/\lambda\rho$ from D15-6 well-log computation with $\Delta(\lambda\rho)/\lambda\rho$ from a) the simultaneous inversion and b) P-P stand-alone inversion.

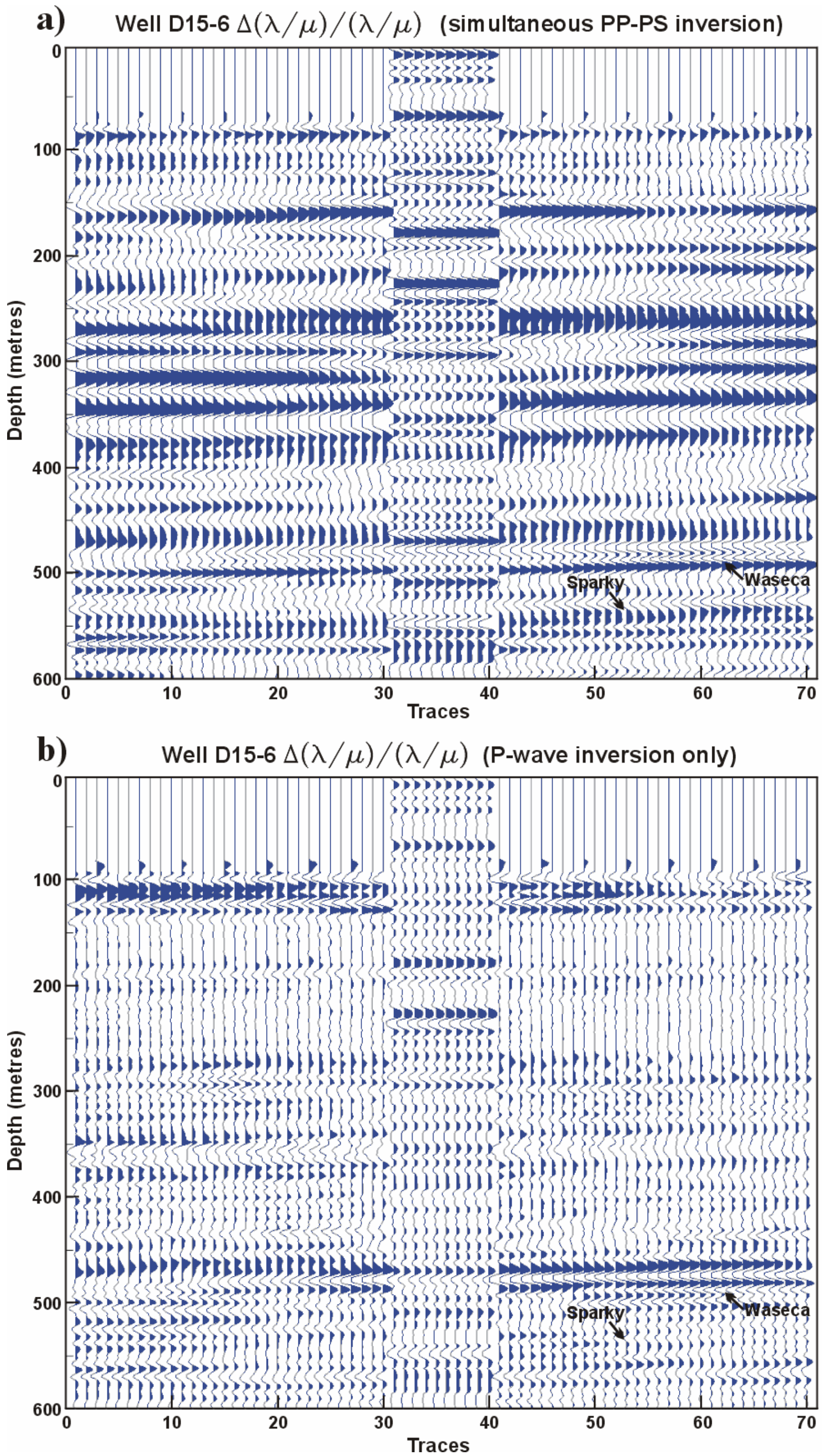

Figure 4.7: Comparison of $\Delta(\lambda/\mu)/(\lambda/\mu)$ from D15-6 well-log computation with $\Delta(\lambda/\mu)/(\lambda/\mu)$ from a) the simultaneous inversion and b) P-P stand-alone inversion.

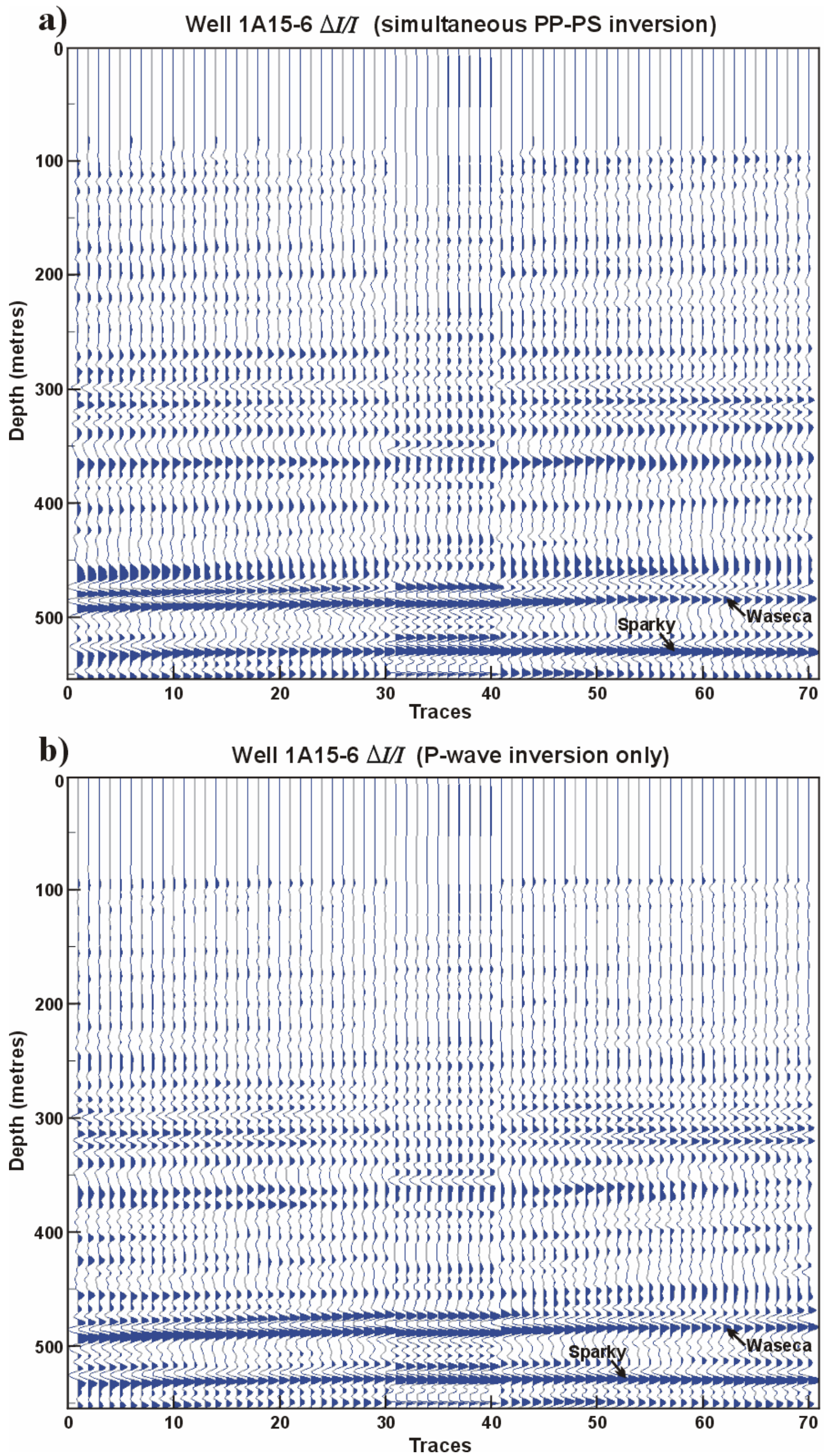

Figure 4.8: Comparison of $\Delta I/I$ from 1A15-6 well-log computation with $\Delta I/I$ from a) the simultaneous inversion and b) P-P stand-alone inversion.

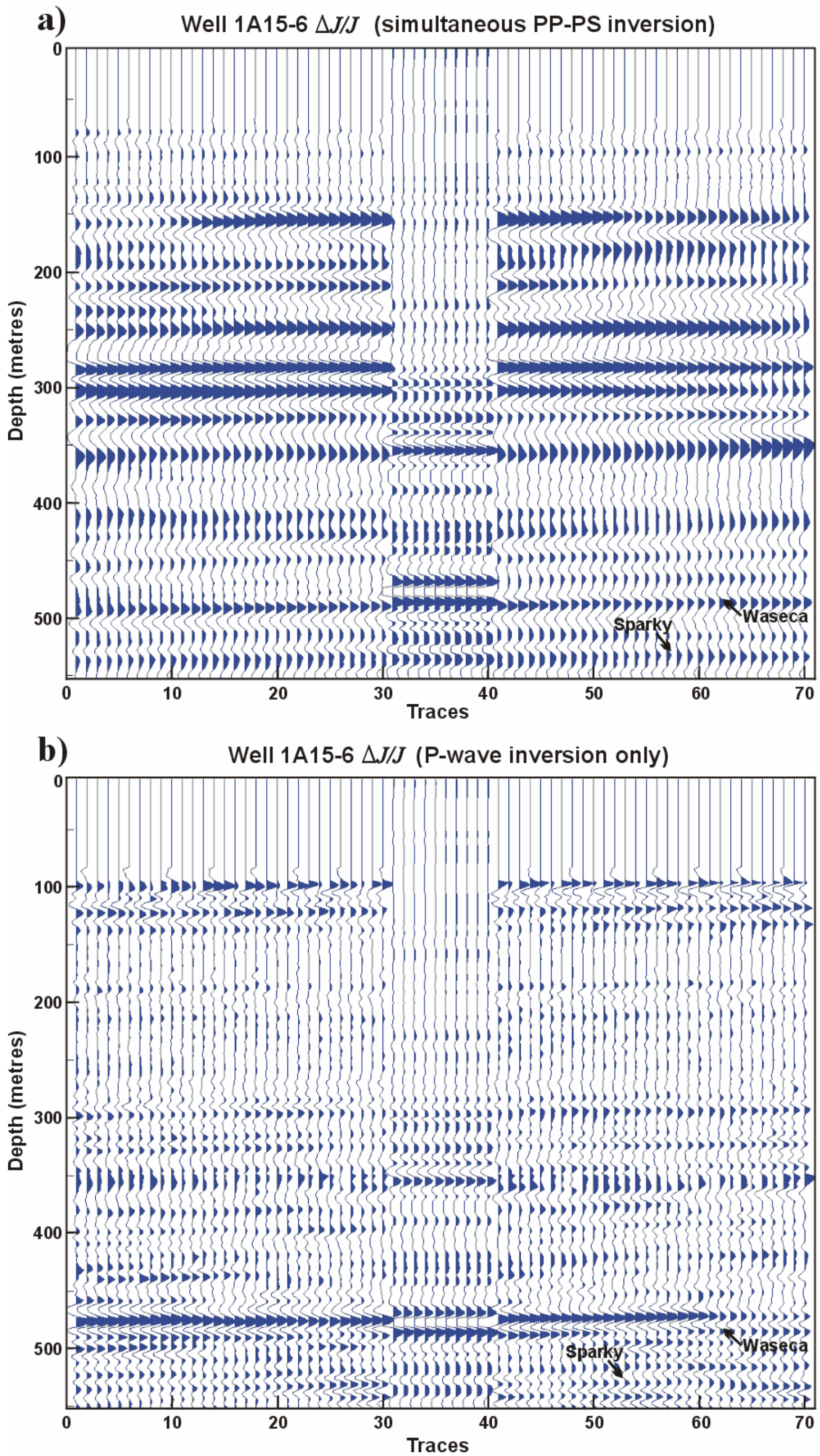

Figure 4.9: Comparison of $\Delta J/J$ from 1A15-6 well-log computation with $\Delta J/J$ from a) the simultaneous inversion and b) P-P stand-alone inversion.

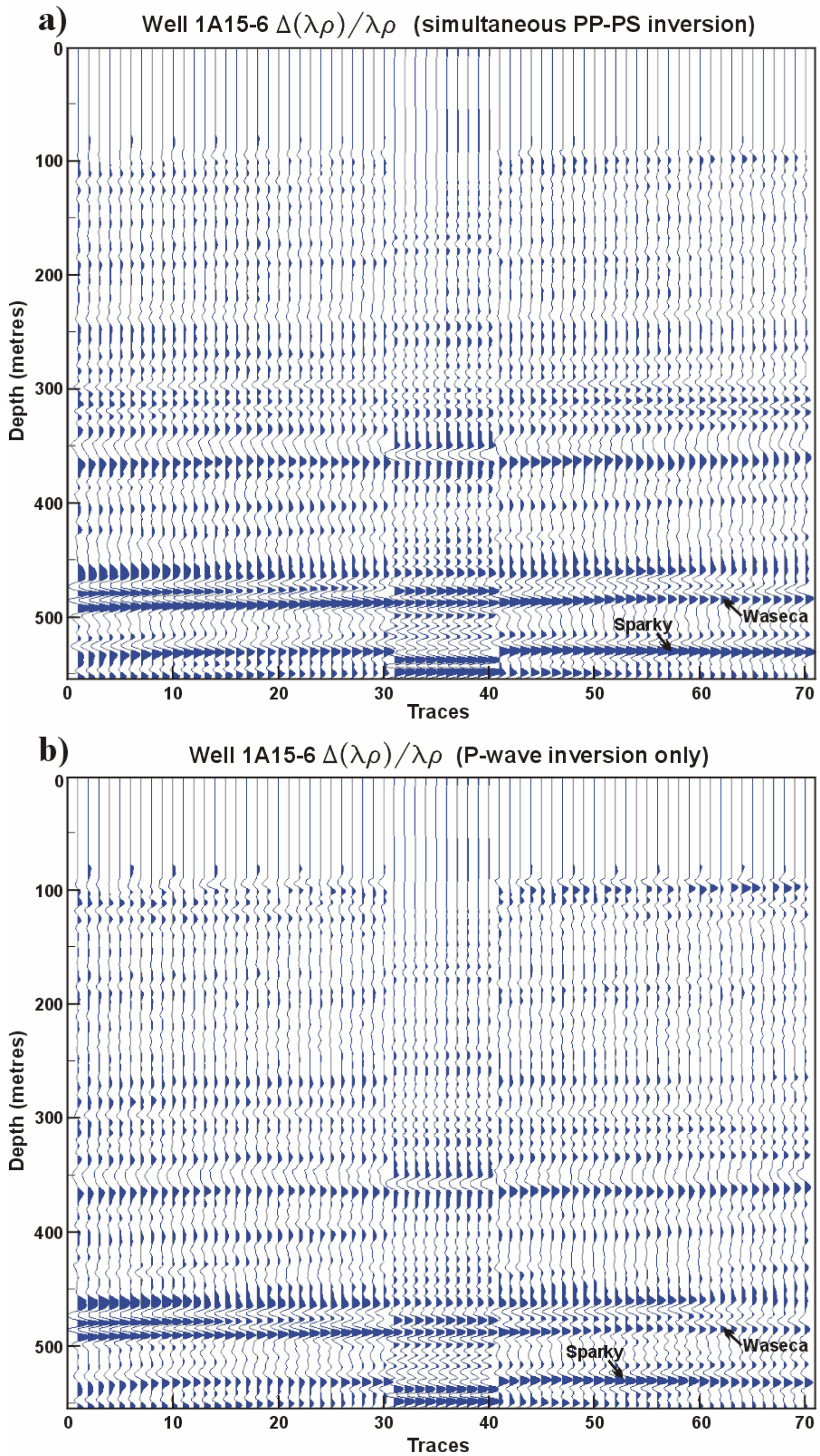

Figure 4.10: Comparison of $\Delta(\lambda\rho)/\lambda\rho$ from 1A15-6 well-log computation with $\Delta(\lambda\rho)/\lambda\rho$ from a) the simultaneous inversion and b) P-P stand-alone inversion.

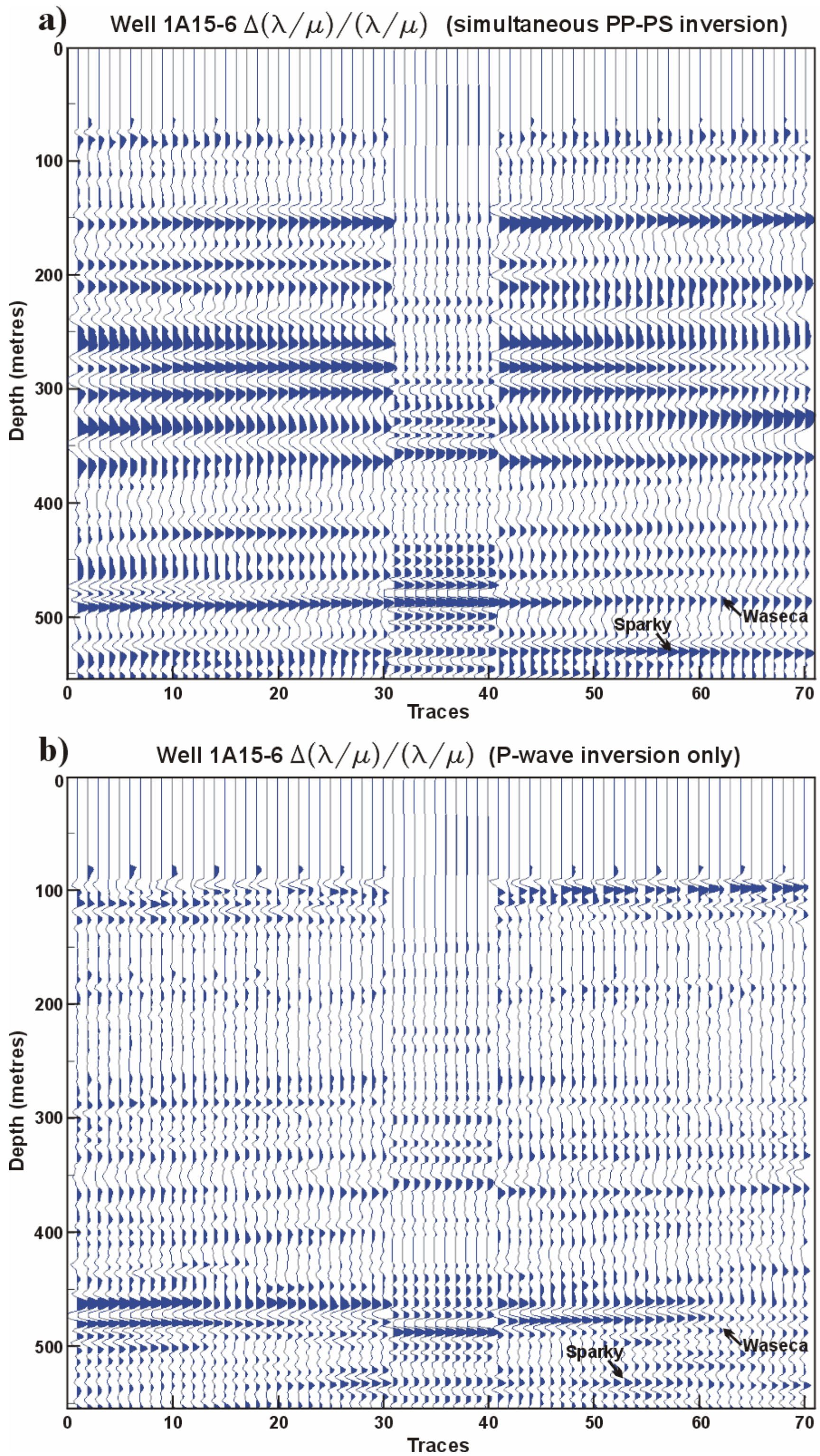

Figure 4.11: Comparison of $\Delta(\lambda/\mu)/(\lambda/\mu)$ from 1A15-6 well-log computation with $\Delta(\lambda/\mu)/(\lambda/\mu)$ from a) the simultaneous inversion and b) P-P stand-alone inversion.

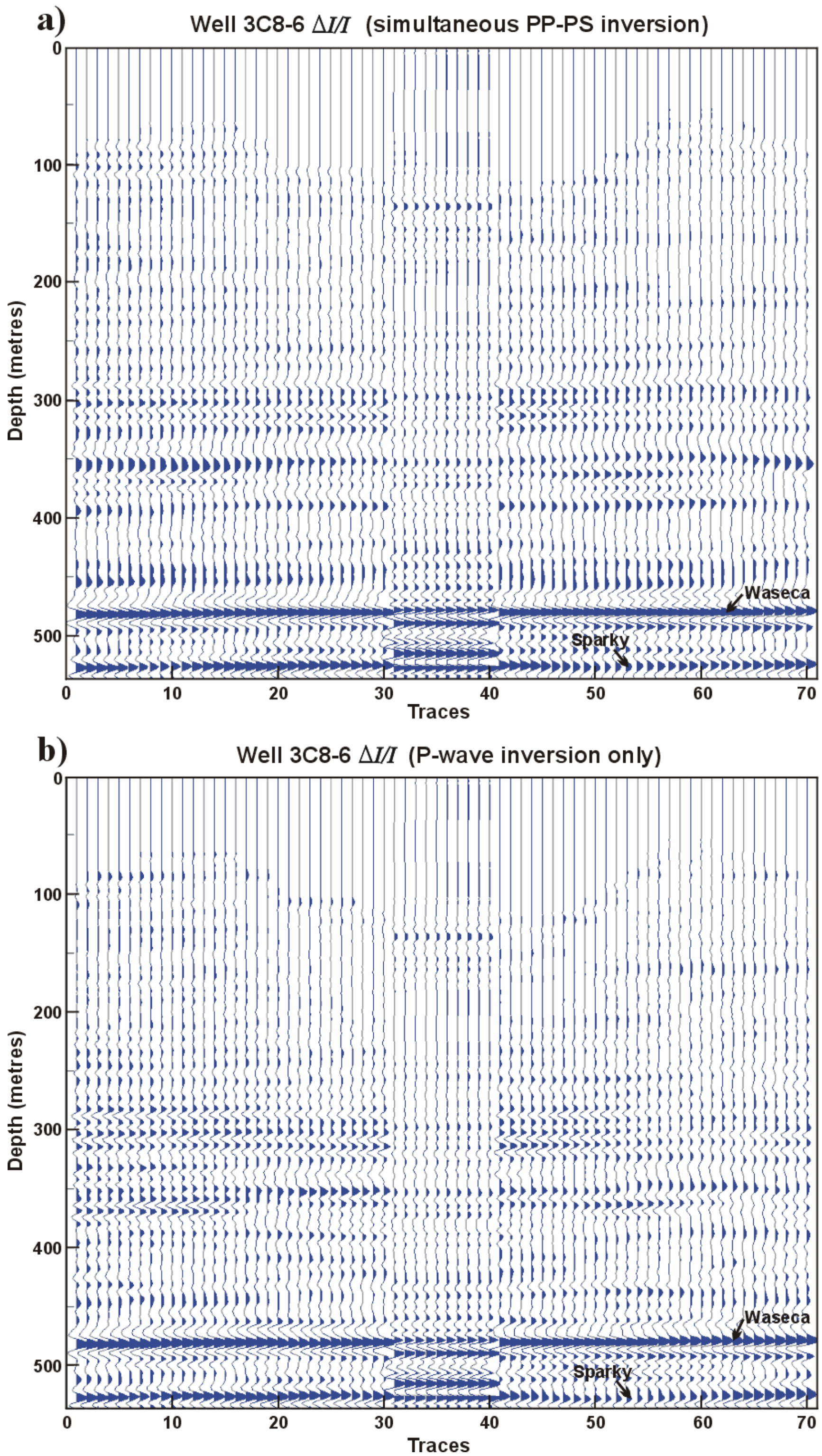

Figure 4.12: Comparison of $\Delta I/I$ from 3C8-6 well-log computation with $\Delta I/I$ from a) the simultaneous inversion and b) P-P stand-alone inversion.

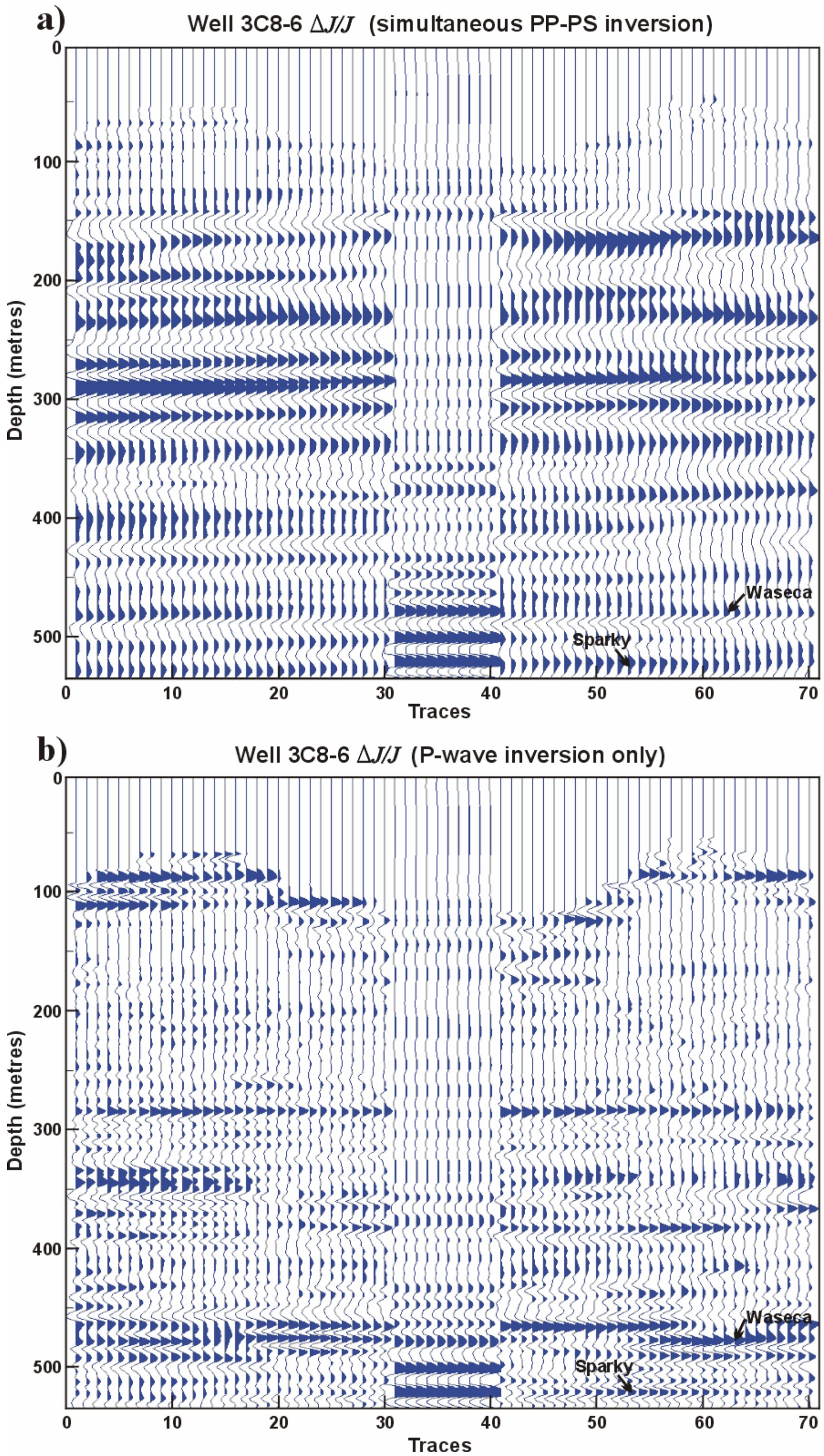

Figure 4.13: Comparison of $\Delta J/J$ from 3C8-6 well-log computation with $\Delta J/J$ from a) the simultaneous inversion and b) P-P stand-alone inversion.

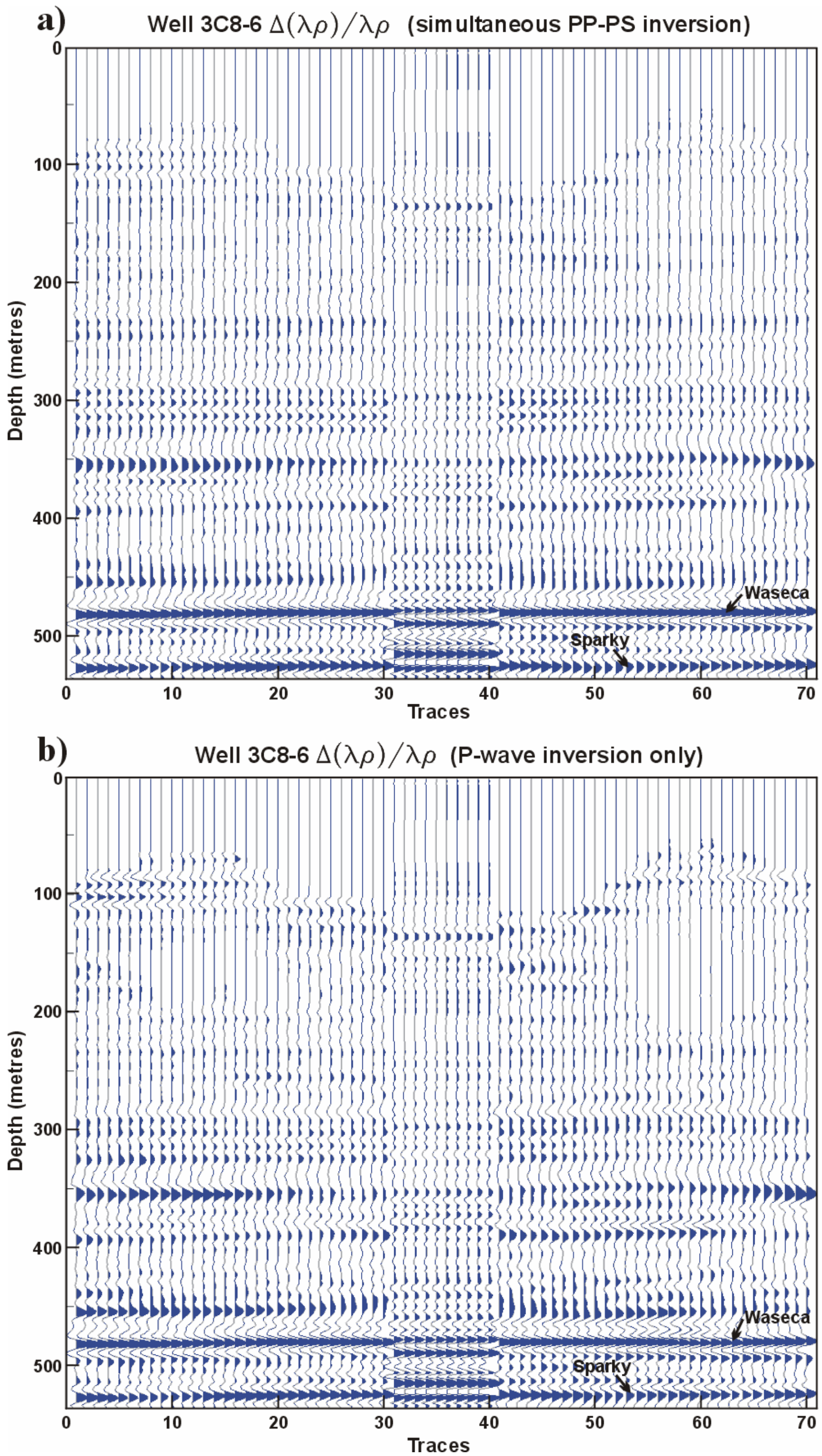

Figure 4.14: Comparison of $\Delta(\lambda\rho)/\lambda\rho$ from 3C8-6 well-log computation with $\Delta(\lambda\rho)/\lambda\rho$ from a) the simultaneous inversion and b) P-P stand-alone inversion.

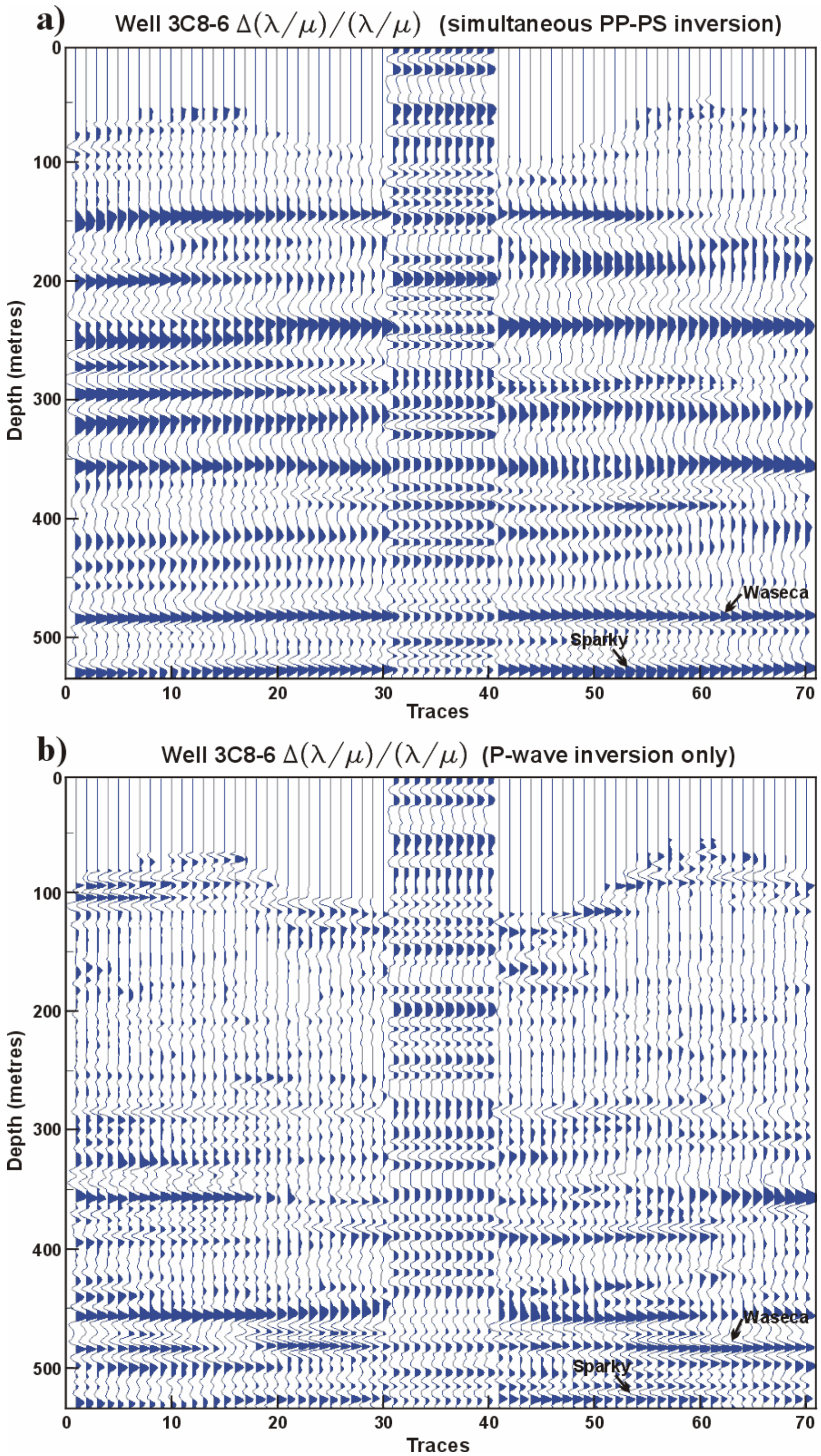

Figure 4.15: Comparison of $\Delta(\lambda/\mu)/(\lambda/\mu)$ from 3C8-6 well-log computation with $\Delta(\lambda/\mu)/(\lambda/\mu)$ from a) the simultaneous inversion and b) P-P stand-alone inversion.

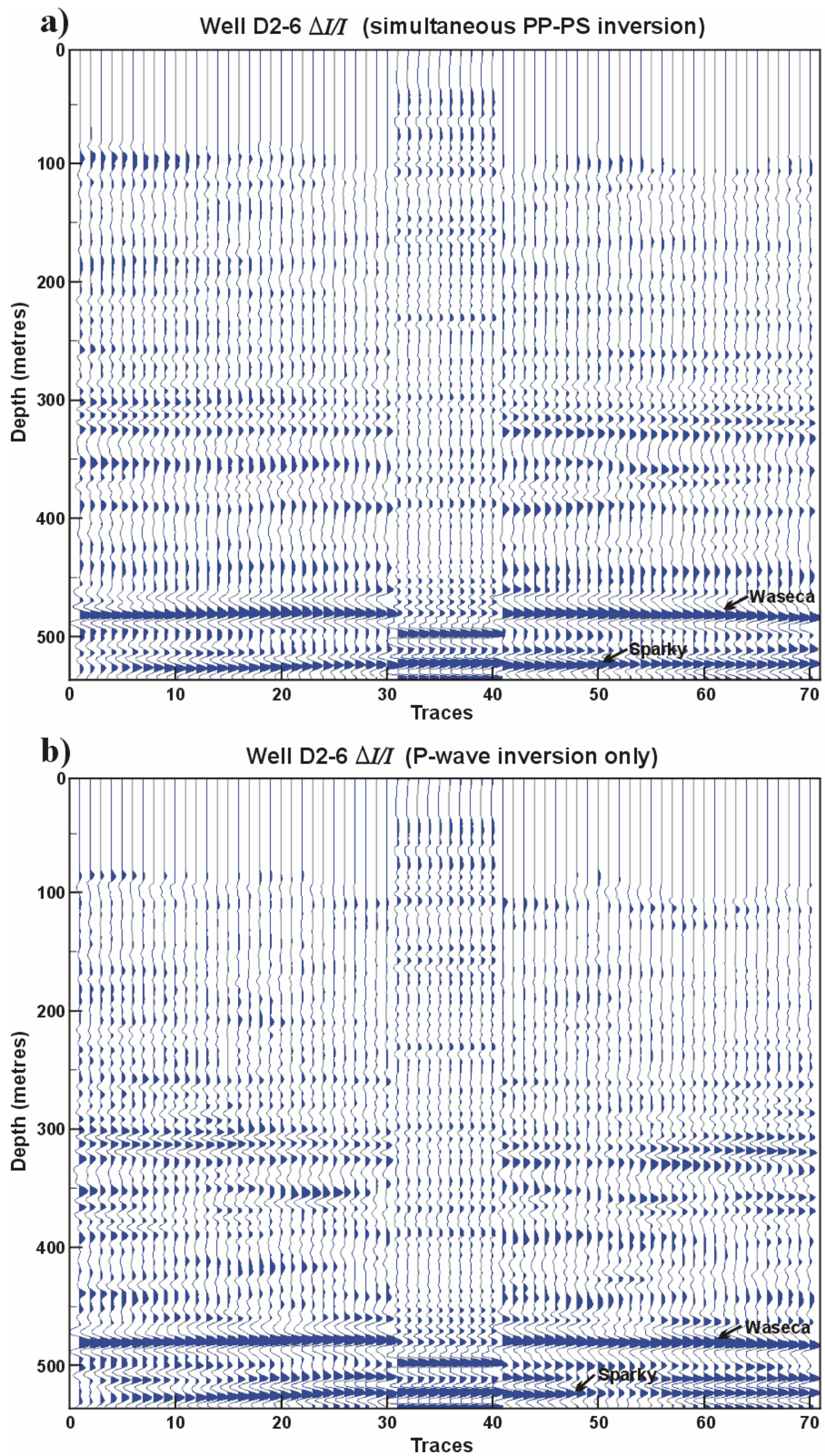

Figure 4.16: Comparison of $\Delta I/I$ from D2-6 well-log computation with $\Delta I/I$ from a) the simultaneous inversion and b) P-P stand-alone inversion.

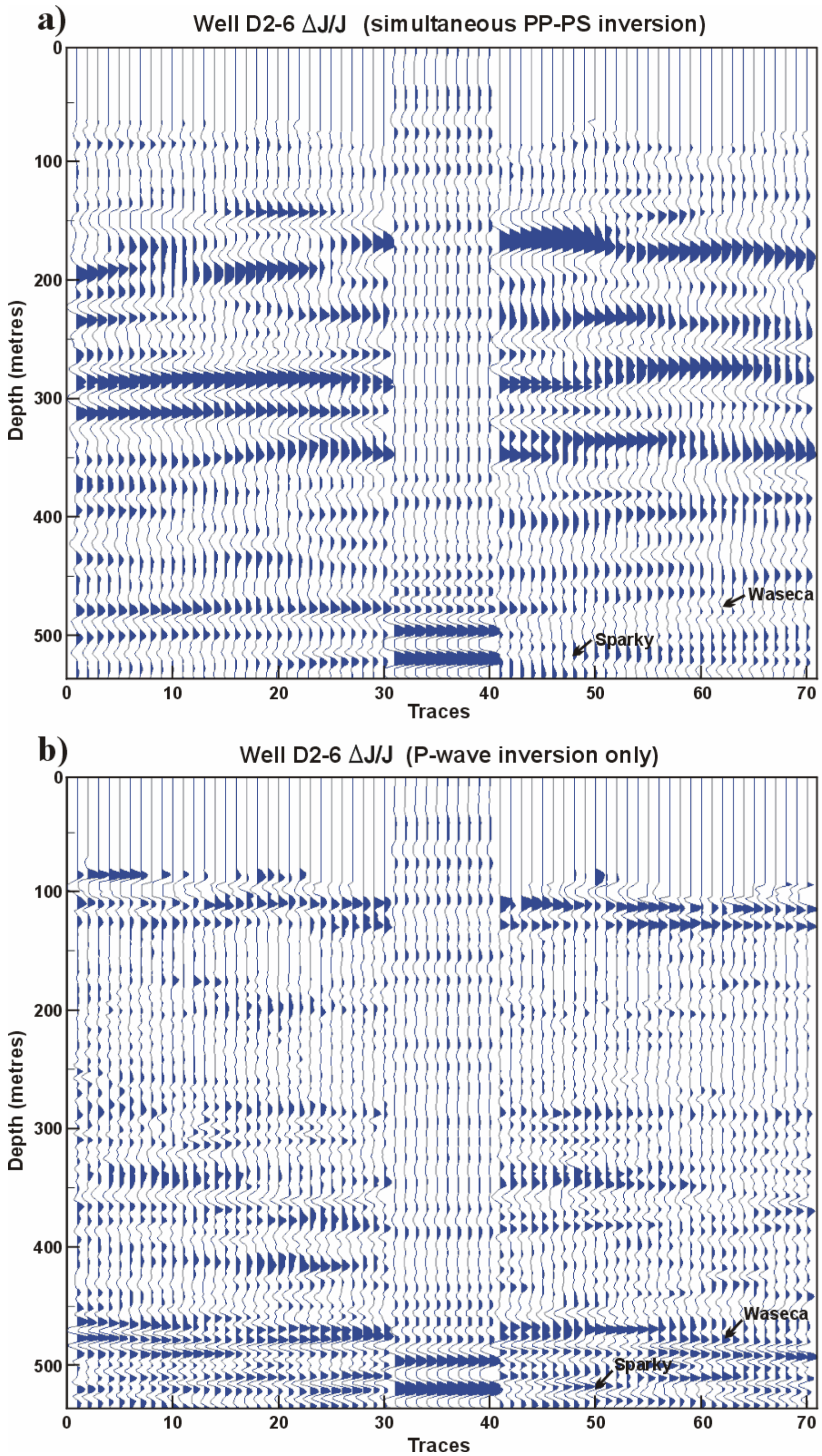

Figure 4.17: Comparison of $\Delta J/J$ from D2-6 well-log computation with $\Delta J/J$ from a) the simultaneous inversion and b) P-P stand-alone inversion.

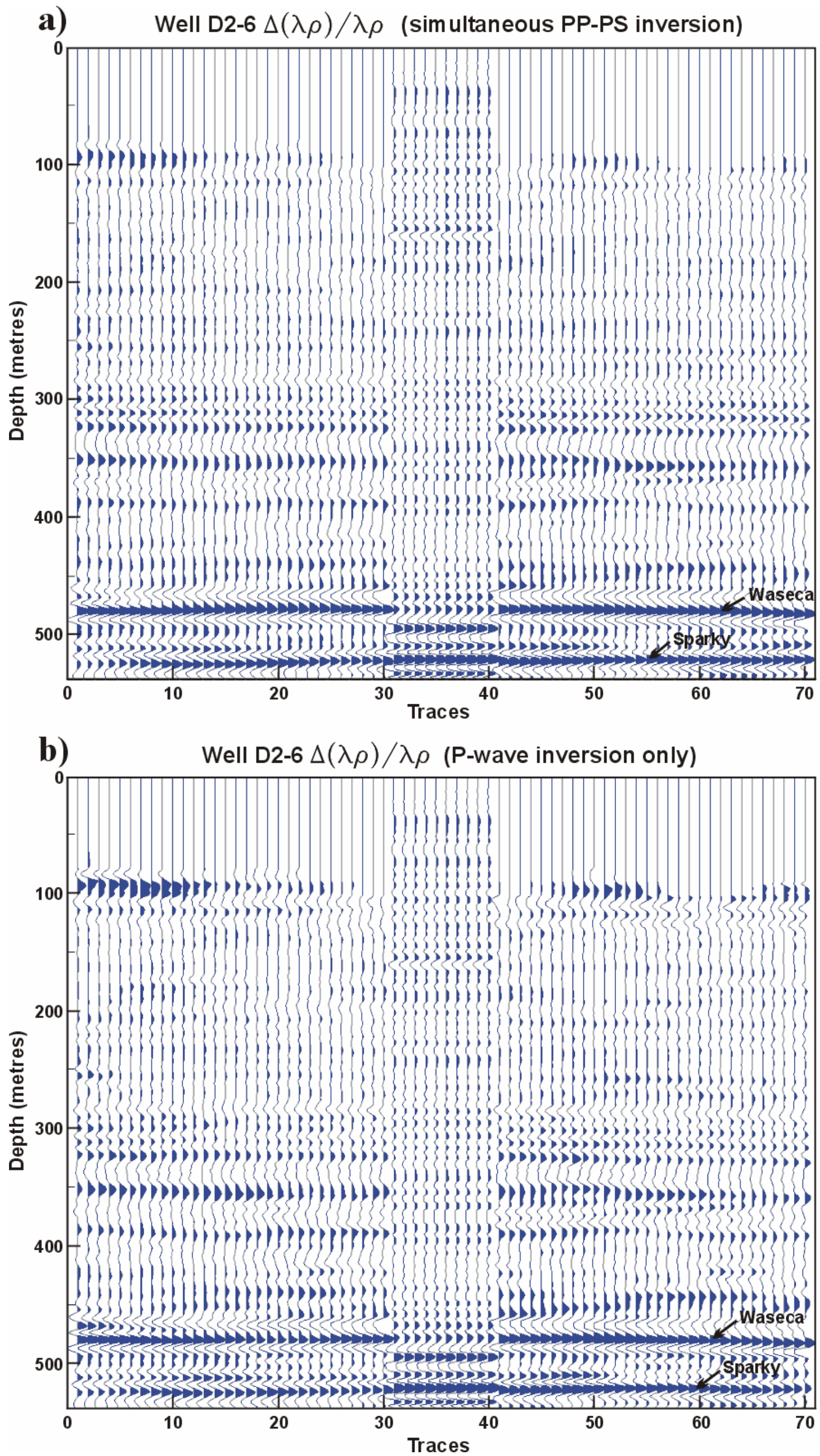

Figure 4.18: Comparison of $\Delta(\lambda\rho)/\lambda\rho$ from D2-6 well-log computation with $\Delta(\lambda\rho)/\lambda\rho$ from a) the simultaneous inversion and b) P-P stand-alone inversion.

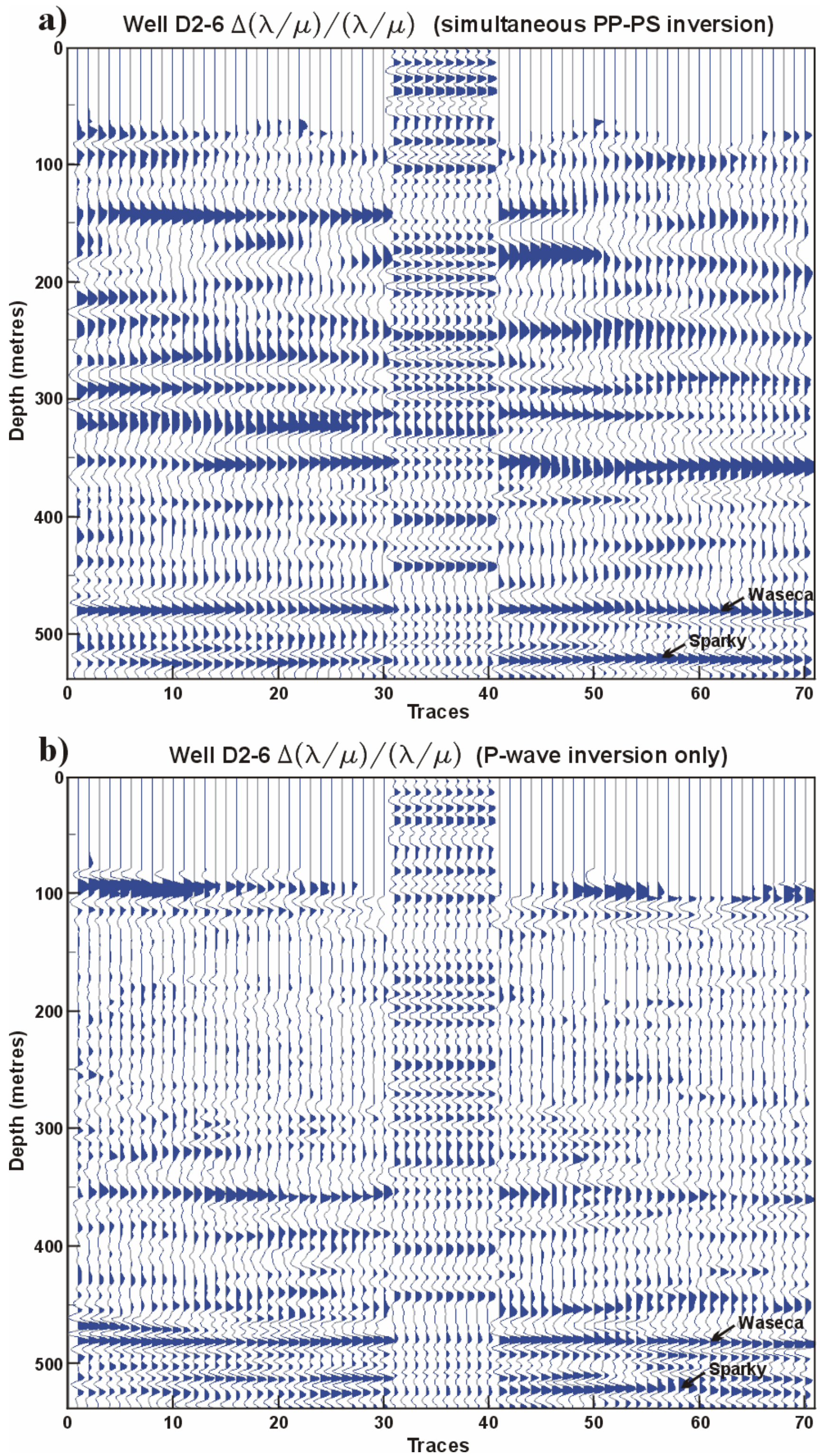

Figure 4.19: Comparison of $\Delta(\lambda/\mu)/(\lambda/\mu)$ from D2-6 well-log computation with $\Delta(\lambda/\mu)/(\lambda/\mu)$ from a) the simultaneous inversion and b) P-P stand-alone inversion.

Especially; the channel sequence within the zone of interest between the Waseca top and Sparky top is somewhat better imaged by the joint inversion in well 3C8-6 and D2-6, where the hydrocarbon was found (figures 4.20-4.23). The toplap channel-sequence features around wells D15-6 and 1A15-6 are shown more clearly by the joint inversion than P-wave-only inversion (figures 4.24-4.25). So the joint inversion fits the interpretation better than P-wave-only inversion.

Meanwhile, among the four attributes inverted for, $\Delta I/I$ and $\Delta(\lambda\rho)/\lambda\rho$ are of higher frequencies and better imaging quality because they are more highly dependent upon P-P reflectivity. In contrast, $\Delta J/J$ and $\Delta(\lambda/\mu)/(\lambda/\mu)$ are of lower frequency because they are more dependent on shear impedance contrasts.

There are some misties between seismic inversion and well-log computation in either the shallow part of the section or the zone of interest. The latter may be due to phase differences between seismic and well-log computation and the noise caused by the steam-injection that was going on in the nearby wells. The former may be due to both lower fold for shallow seismic data and phase differences. Wells 3C8-6 and D2-6 were logged before the steam-injection was done and the seismic data were acquired after the steam-injection was done. This difference in conditions is probably another reason why the correlation between the 3C8-6 and D2-6 well-log computations and the seismic inversion is not as good as that of wells D15-6 and 1A15-6.

4.5 Results of applying different velocities in the time-depth conversion and the simultaneous inversion

The background velocities derived in the two different ways illustrated in chapter 3 were used in the time-depth conversion of the P-P and P-S seismic data and PP-PS simultaneous AVO inversion. Well 1A15-6 and 3C8-6 were put through the following experiments to judge which method yields more accurate velocities for the joint inversion. No horizon is flattened in the seismic data.

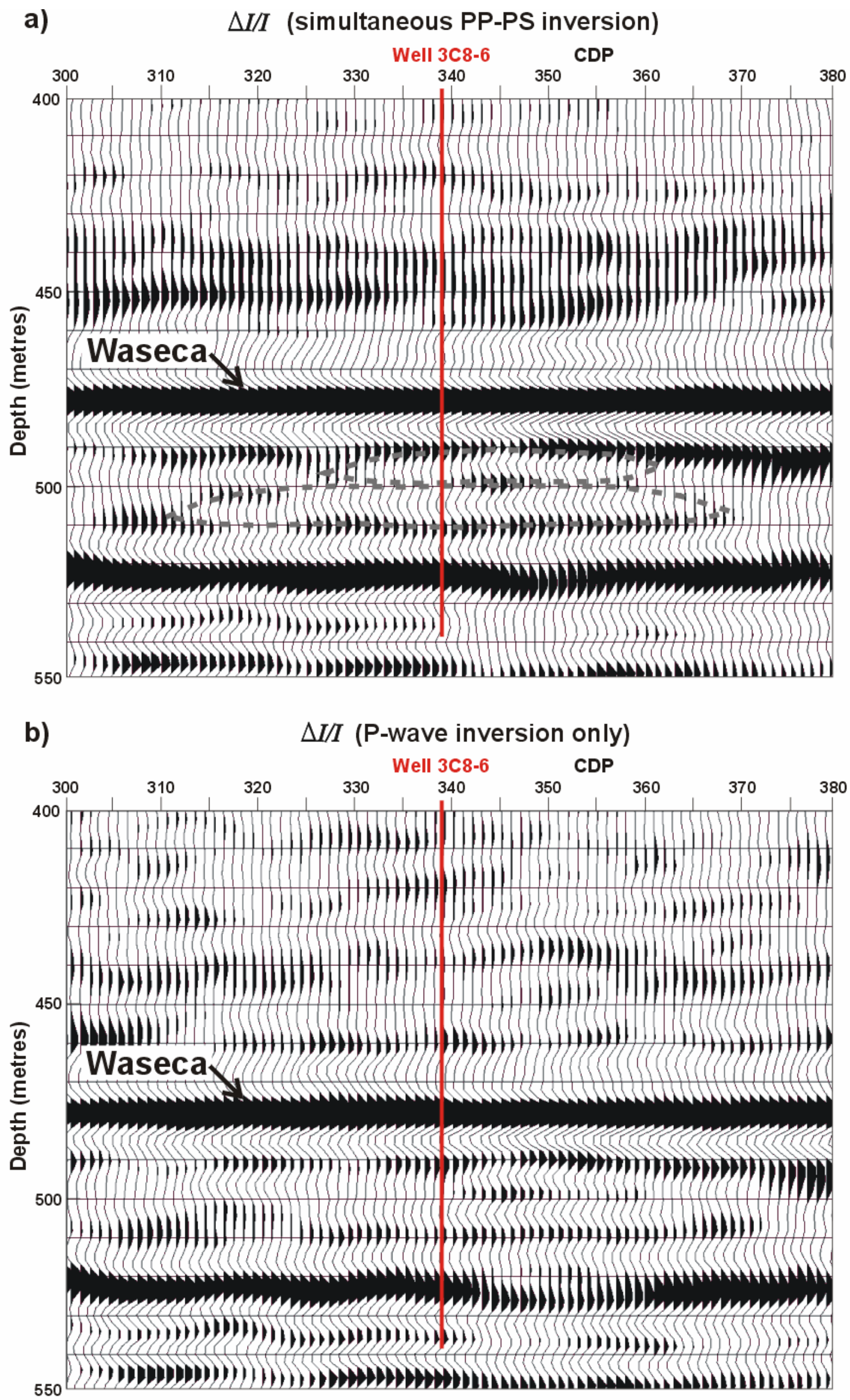

Figure 4.20: The channel sequence around well 3C8-6 shown in $\Delta I/I$ is somewhat more clearly imaged by a) the simultaneous inversion than b) P-P stand-alone inversion.

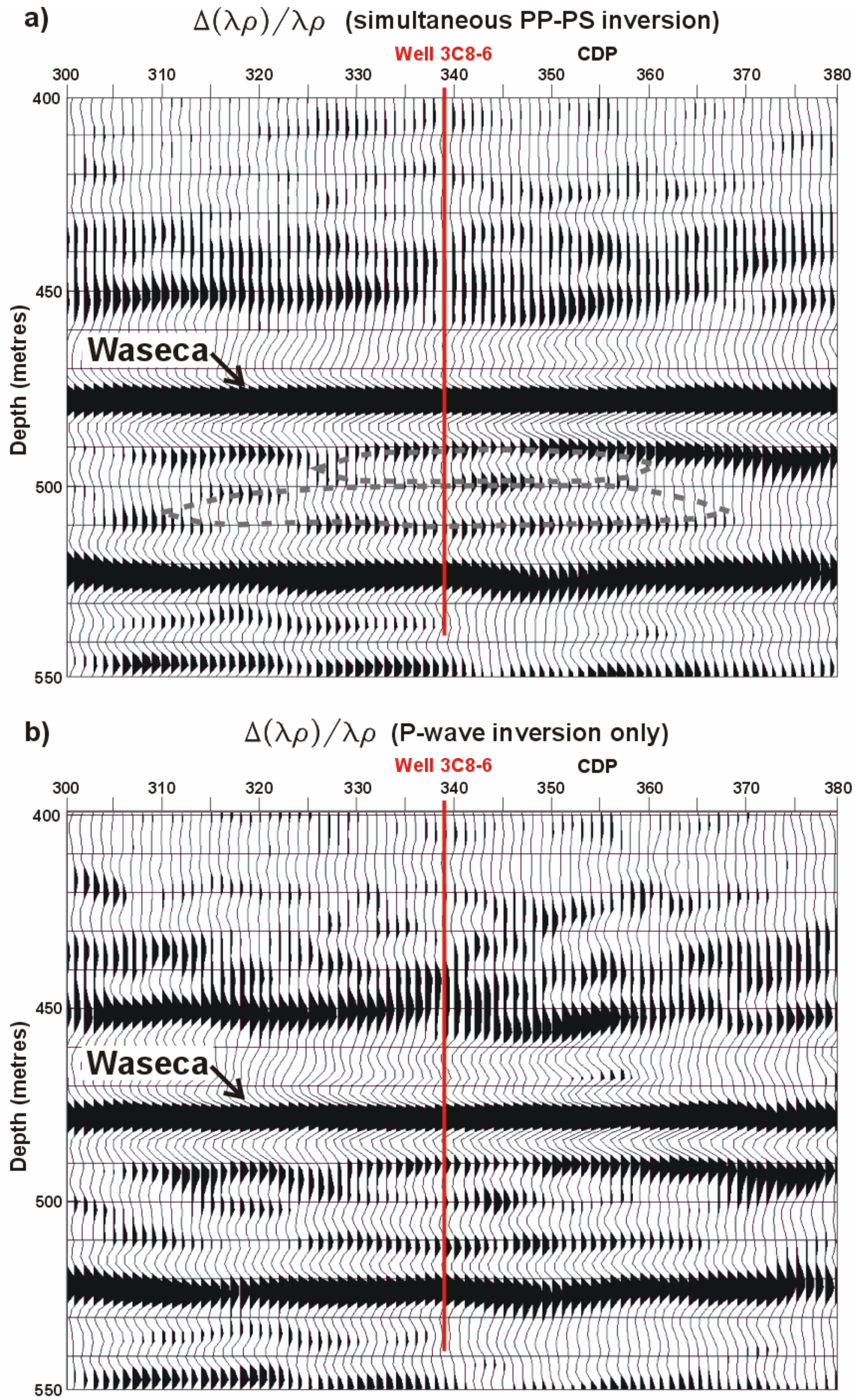

Figure 4.21: The channel sequence around well 3C8-6 shown in $\Delta(\lambda\rho)/\lambda\rho$ is somewhat more clearly imaged by a) the simultaneous inversion than b) P-P stand-alone inversion.

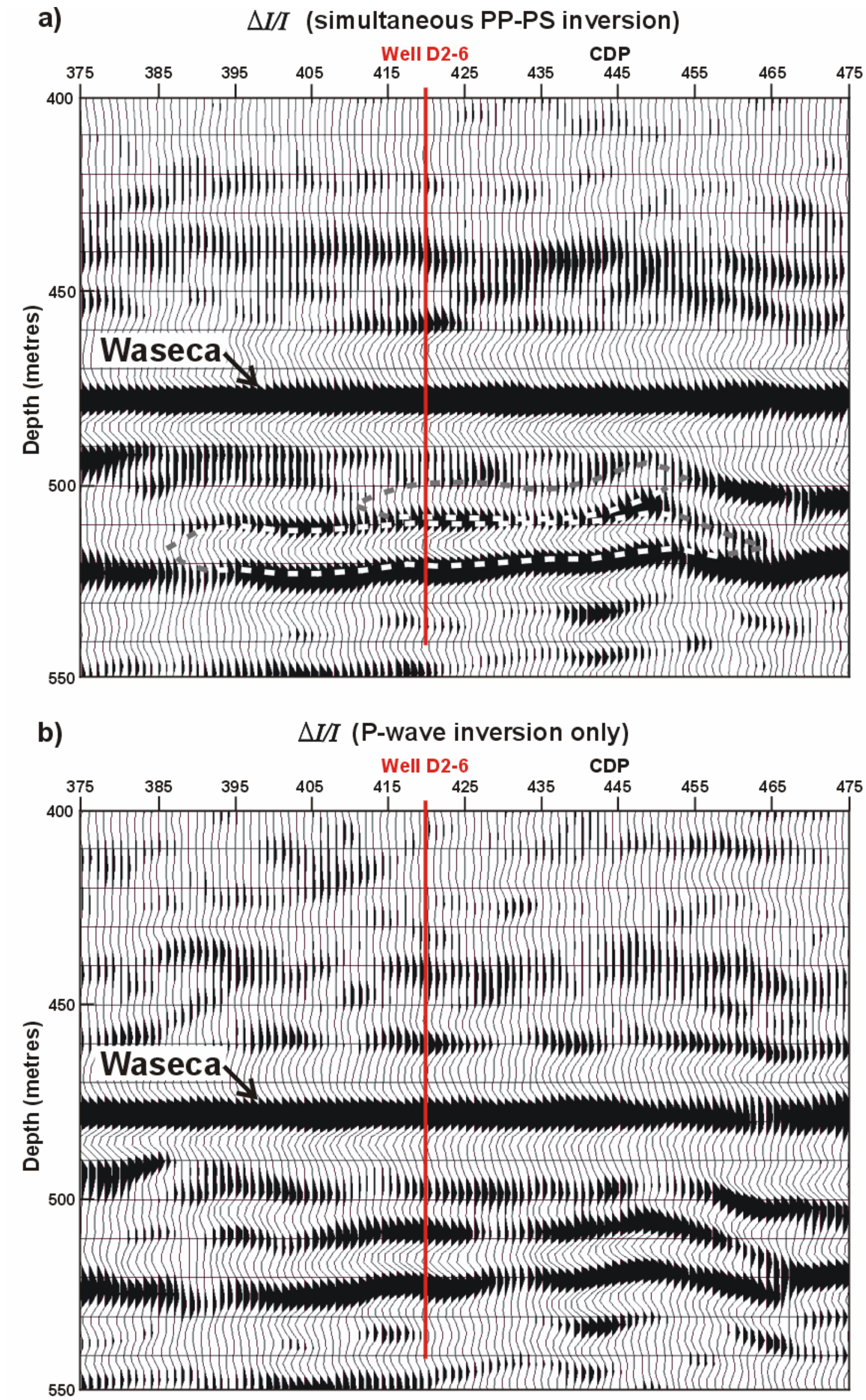

Figure 4.22: The channel sequence around well D2-6 shown in $\Delta I/I$ is slightly more clearly imaged by a) the simultaneous inversion than b) P-P stand-alone inversion.

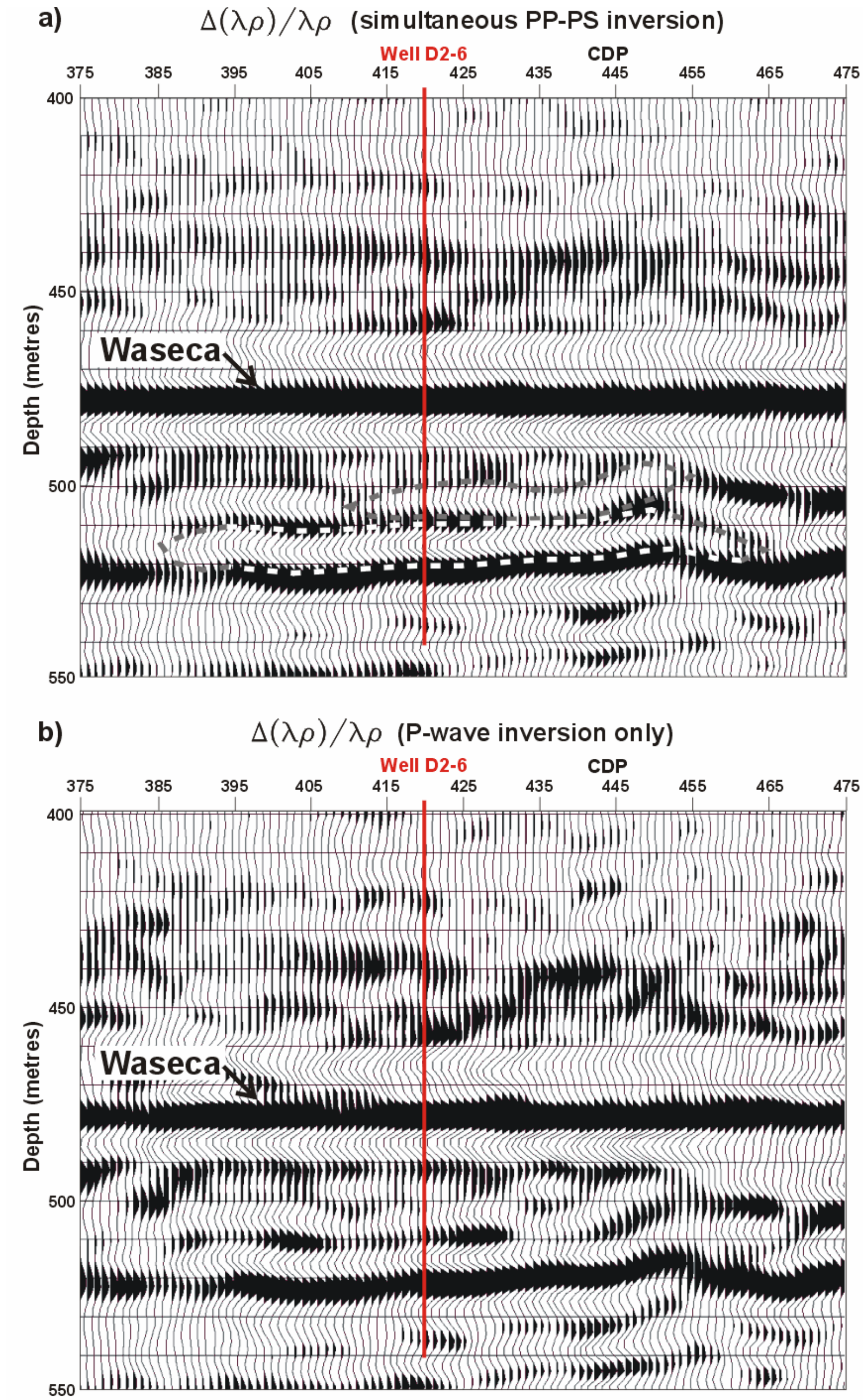

Figure 4.23: The channel sequence around well D2-6 shown in $\Delta(\lambda\rho)/\lambda\rho$ is slightly more clearly imaged by a) the simultaneous inversion than b) P-P stand-alone inversion.

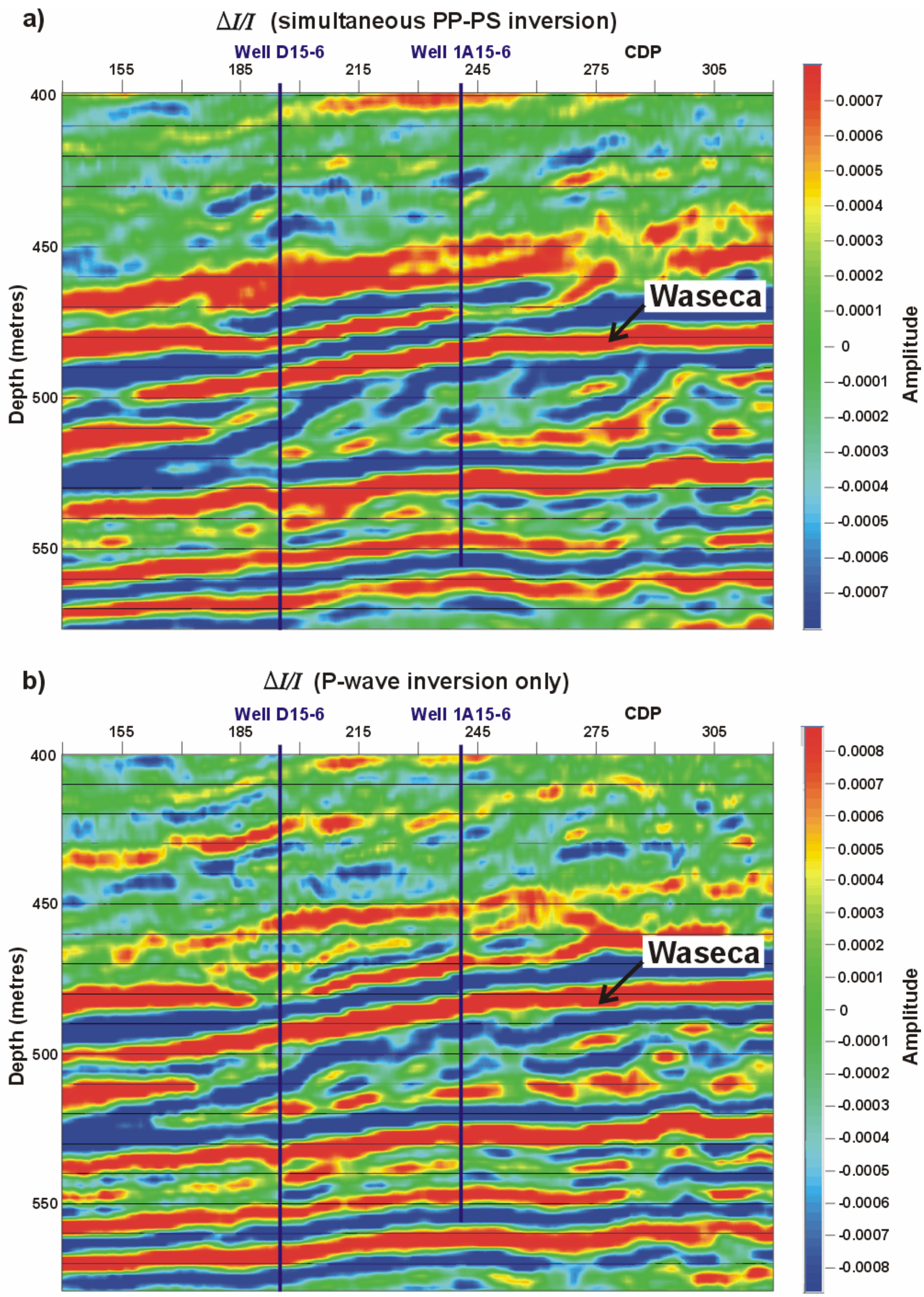

Figure 4.24: The toplap channel sequence feature is better seen around well D15-6 and 1A15-6 in $\Delta I/I$ from a) the simultaneous inversion than b) P-P stand-alone inversion.

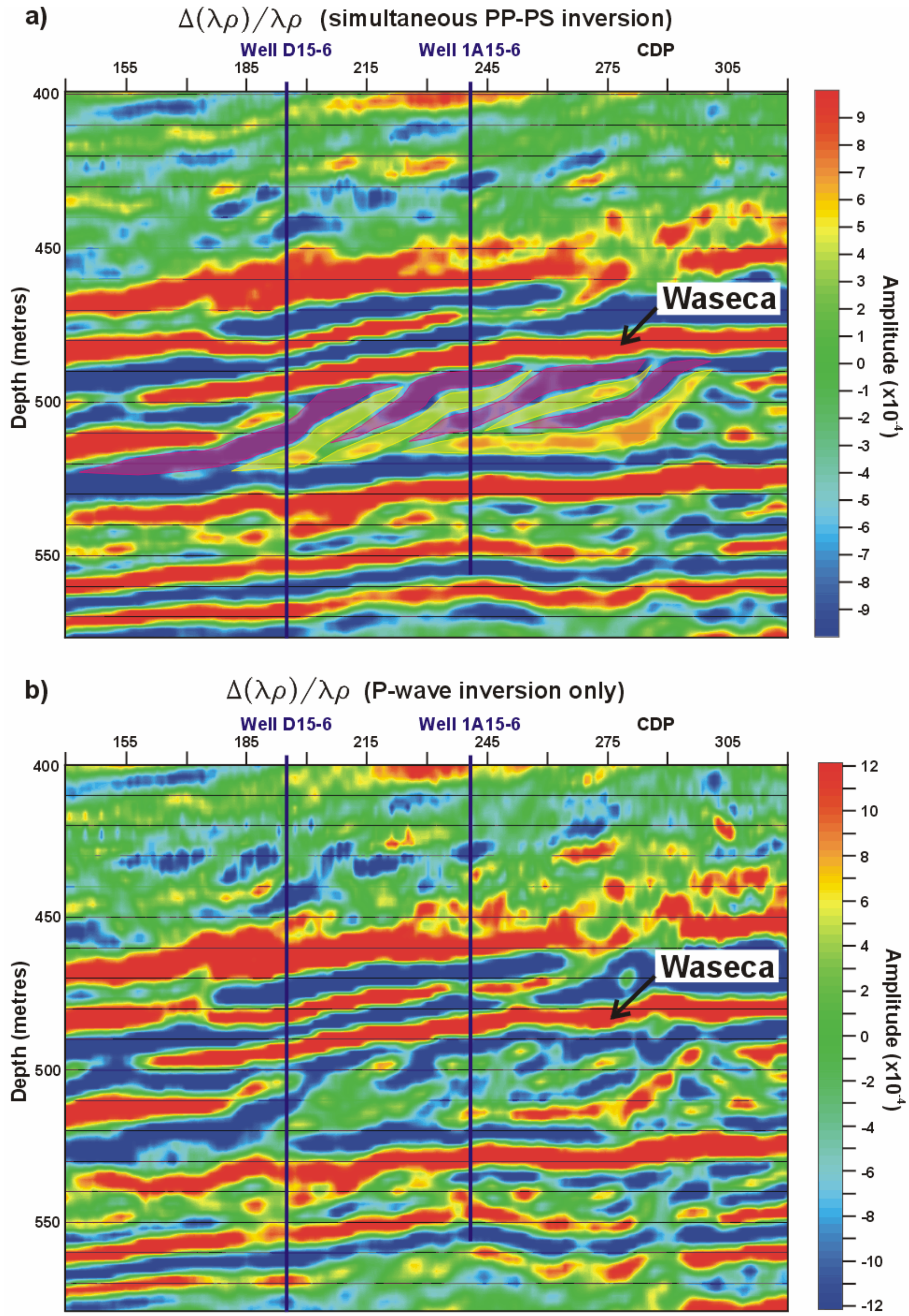

Figure 4.25: The toplap channel sequence feature highlighted in purple and yellow is better seen around well D15-6 and 1A15-6 in $\Delta(\lambda\rho)/\lambda\rho$ from a) the simultaneous inversion than b) P-P stand-alone inversion.

First, the interval P and S velocities from well 1A15-6 were employed in both the time-depth conversion of poststack migrated seismic data and simultaneous inversion. The results of comparison for well 1A15-6 are seen in figures 4.8a, 4.9a, 4.10a and 4.11a. For well 3C8-6, the results are shown in figures 4.12a, 4.13a, 4.14a and 4.15a.

Second, the interval velocities from well 1A15-6 were employed in the time-depth conversion of the seismic data and the seismic-derived interval velocities in the inversion. The results of comparison are shown in figures 4.26-4.29.

Third, the seismic-derived interval velocities were used in the time-depth conversion and well-log velocities in inversion. The results of comparison are shown in figures 4.30-4.33.

Finally, the seismic-derived interval velocities were used in both the time-depth conversion and inversion with the results of correlation shown in figures 4.34-4.37. Comparing the results from these four experiments, the results of the simultaneous inversion and the correlation with the direct well-log computation are the best when the interval P and S velocities obtained from well 1A15-6 are used. That is why these background velocities were used in both the joint inversion and P-P stand-alone inversion.

4.6 Results of joint inversion for different depth shifts of radial-component seismic data relative to the vertical-component

The existence of P-S seismic data highlights more information on rock properties and pore-fluid parameters in the joint inversion provided that the P-P and P-S data are very well registered. Event correlation was carried out during the course of preparing the seismic data for the joint inversion. But due to the frequency difference in P-P and P-S data, the lack of very good well control and the possible complex geological structure, the event correlation may not be perfect. Hence, the ProMAX module for doing joint PP-PS AVO inversion is designed to allow the P-S seismic data to be shifted in depth relative to the P-P data so that an optimal PP-PS event correlation and thus an optimal inversion results can be achieved.

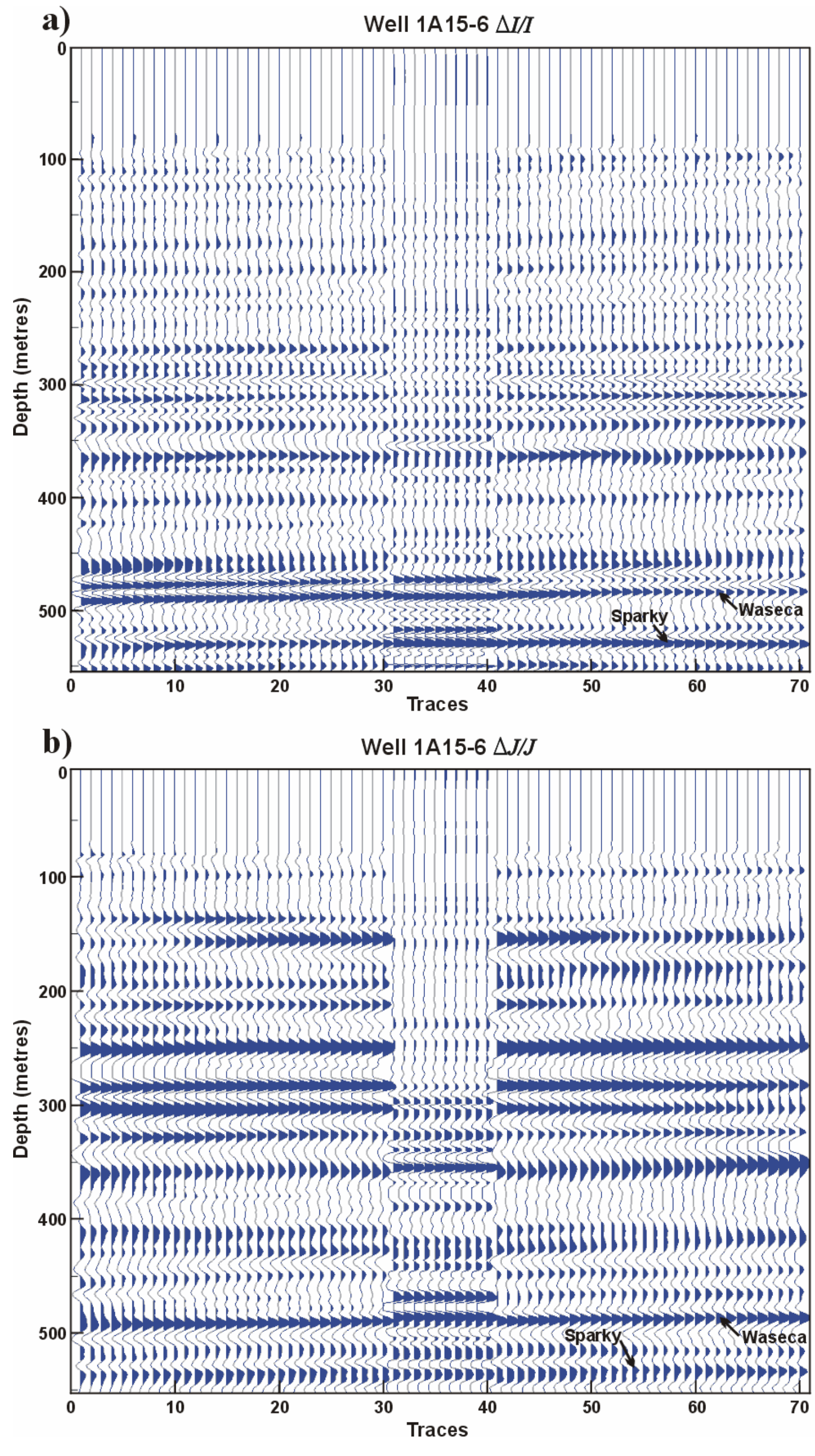

Figure 4.26: Comparison of a) $\Delta I/I$ and b) $\Delta J/J$ from 1A15-6 well-log computations with the simultaneous inversion. The well-log interval velocities were used in the time-depth conversion and seismic interval velocities were used in the inversion.

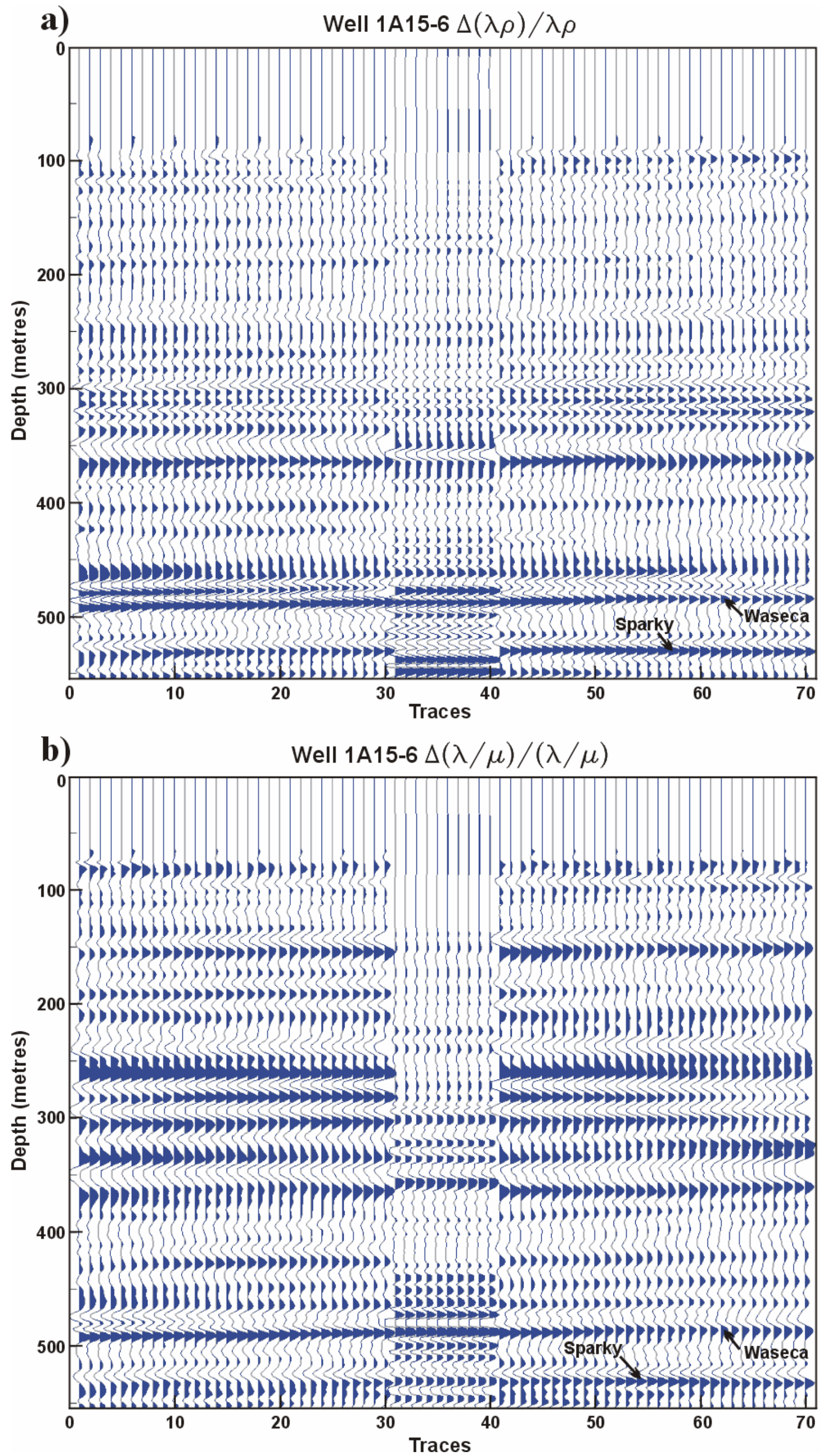

Figure 4.27: Comparison of a) $\Delta(\lambda\rho)/\lambda\rho$ and b) $\Delta(\lambda/\mu)/(\lambda/\mu)$ from 1A15-6 well-log computations with the simultaneous inversion. The well-log interval velocities were used in the time-depth conversion and seismic interval velocities were used in the inversion.

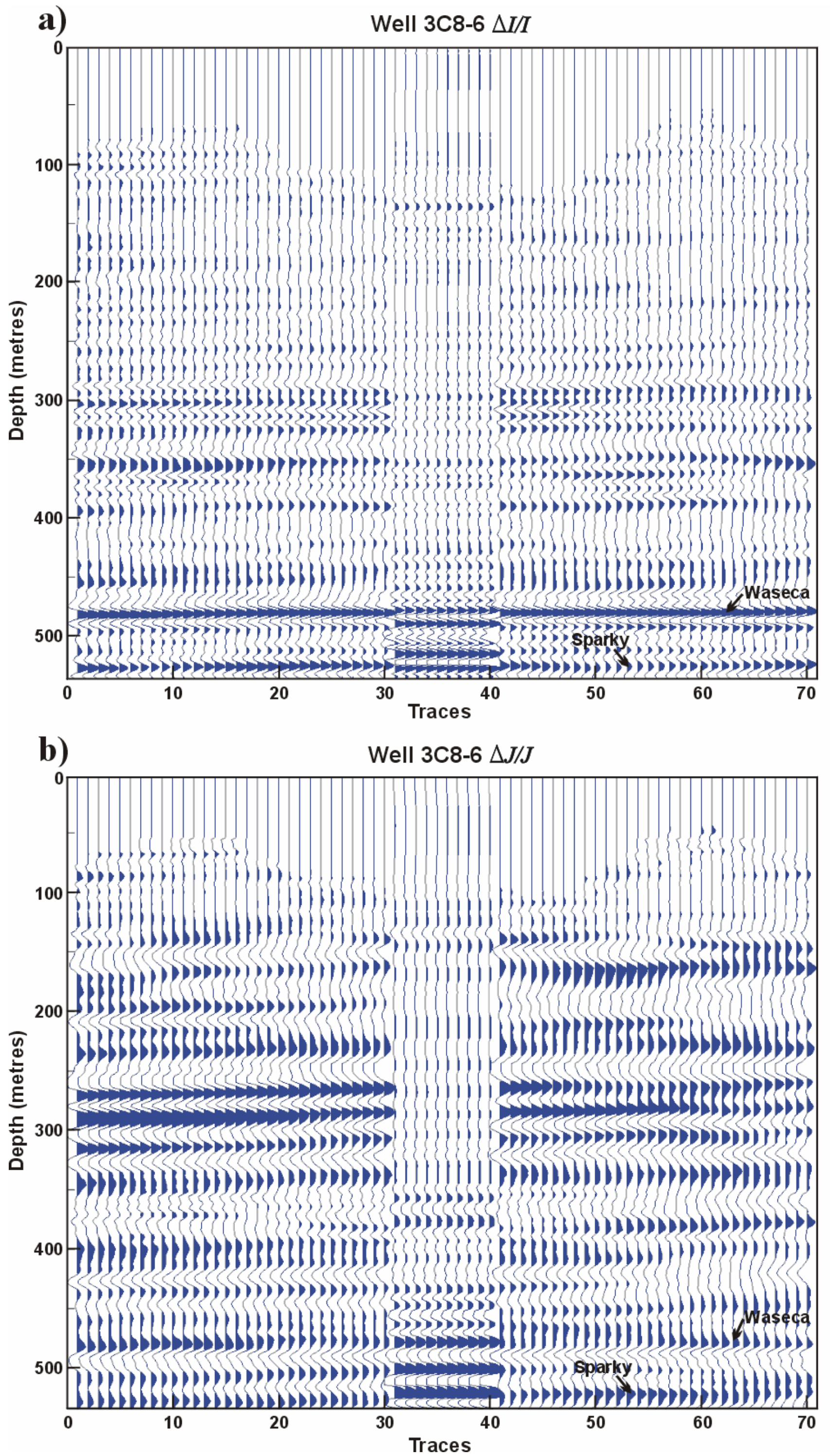

Figure 4.28: Comparison of a) $\Delta I/I$ and b) $\Delta J/J$ from 3C8-6 well-log computations with the simultaneous inversion. The well-log interval velocities were used in the time-depth conversion and seismic interval velocities were used in the inversion.

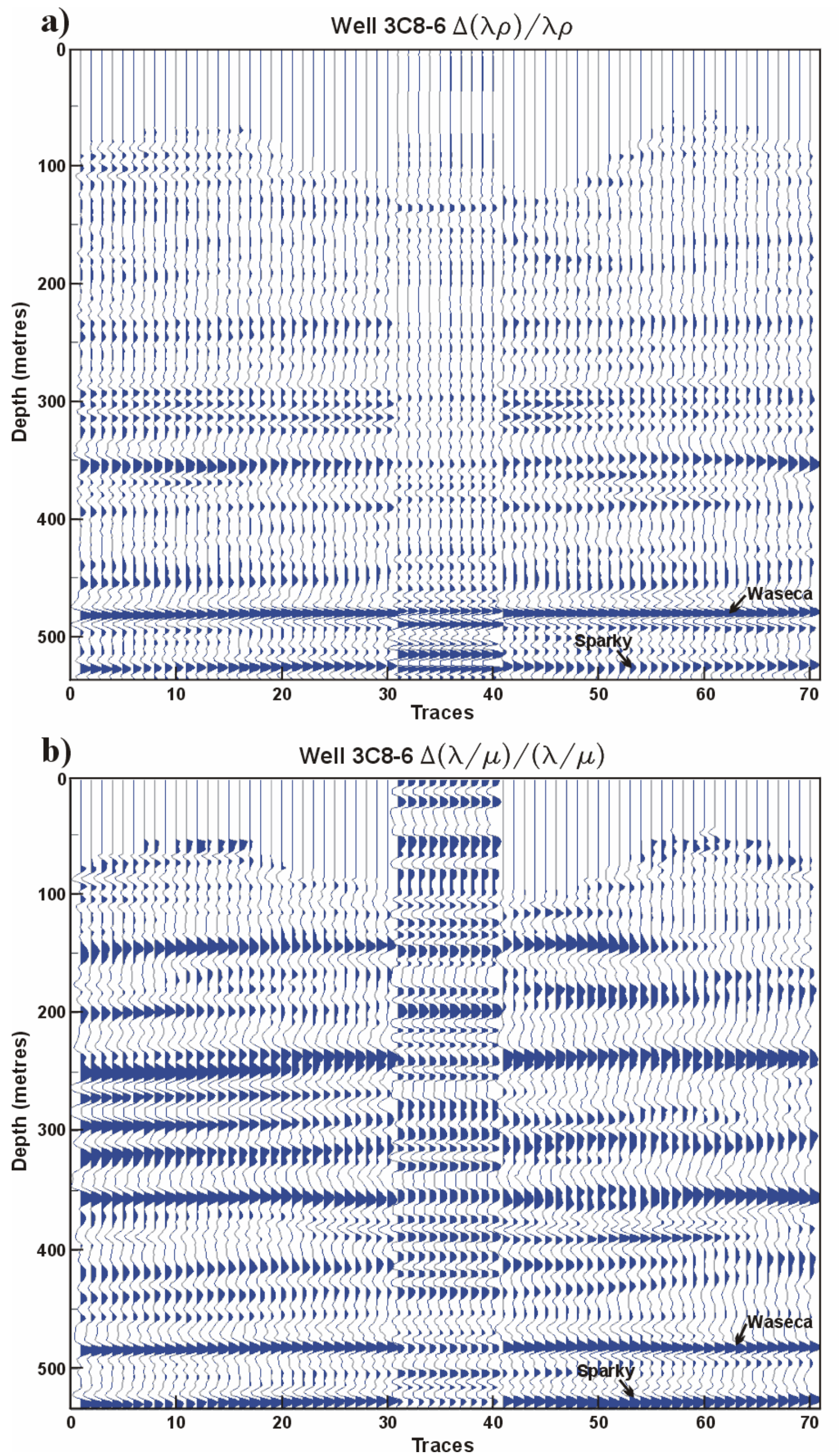

Figure 4.29: Comparison of a) $\Delta(\lambda\rho)/\lambda\rho$ and b) $\Delta(\lambda/\mu)/(\lambda/\mu)$ from 3C8-6 well-log computations with the simultaneous inversion. The well-log interval velocities were used in the time-depth conversion and seismic interval velocities were used in the inversion.

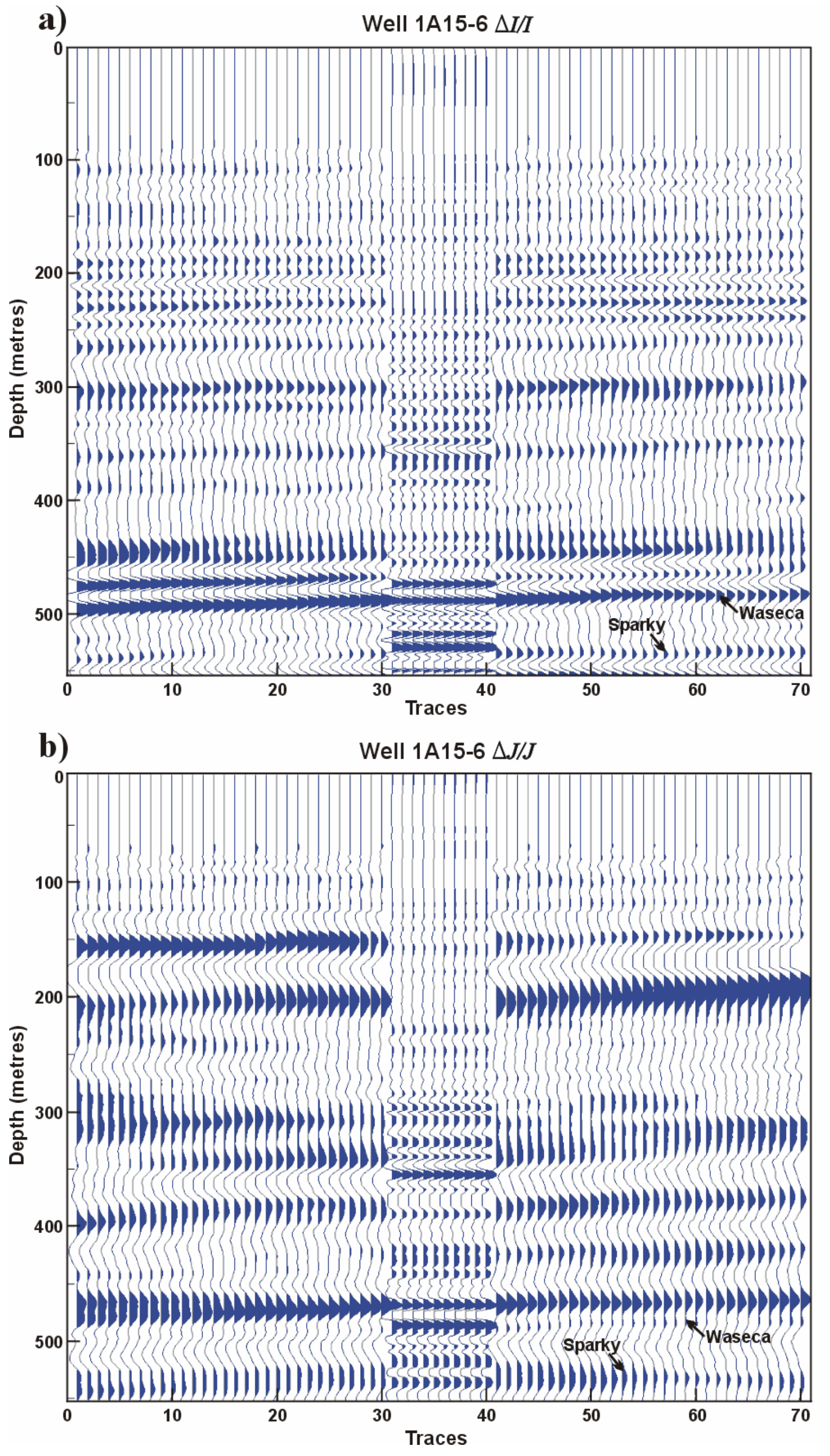

Figure 4.30: Comparison of a) $\Delta I/I$ and b) $\Delta J/J$ from 1A15-6 well-log computations with the simultaneous inversion. The seismic interval velocities were used in the time-depth conversion and well-log interval velocities were used in the inversion.

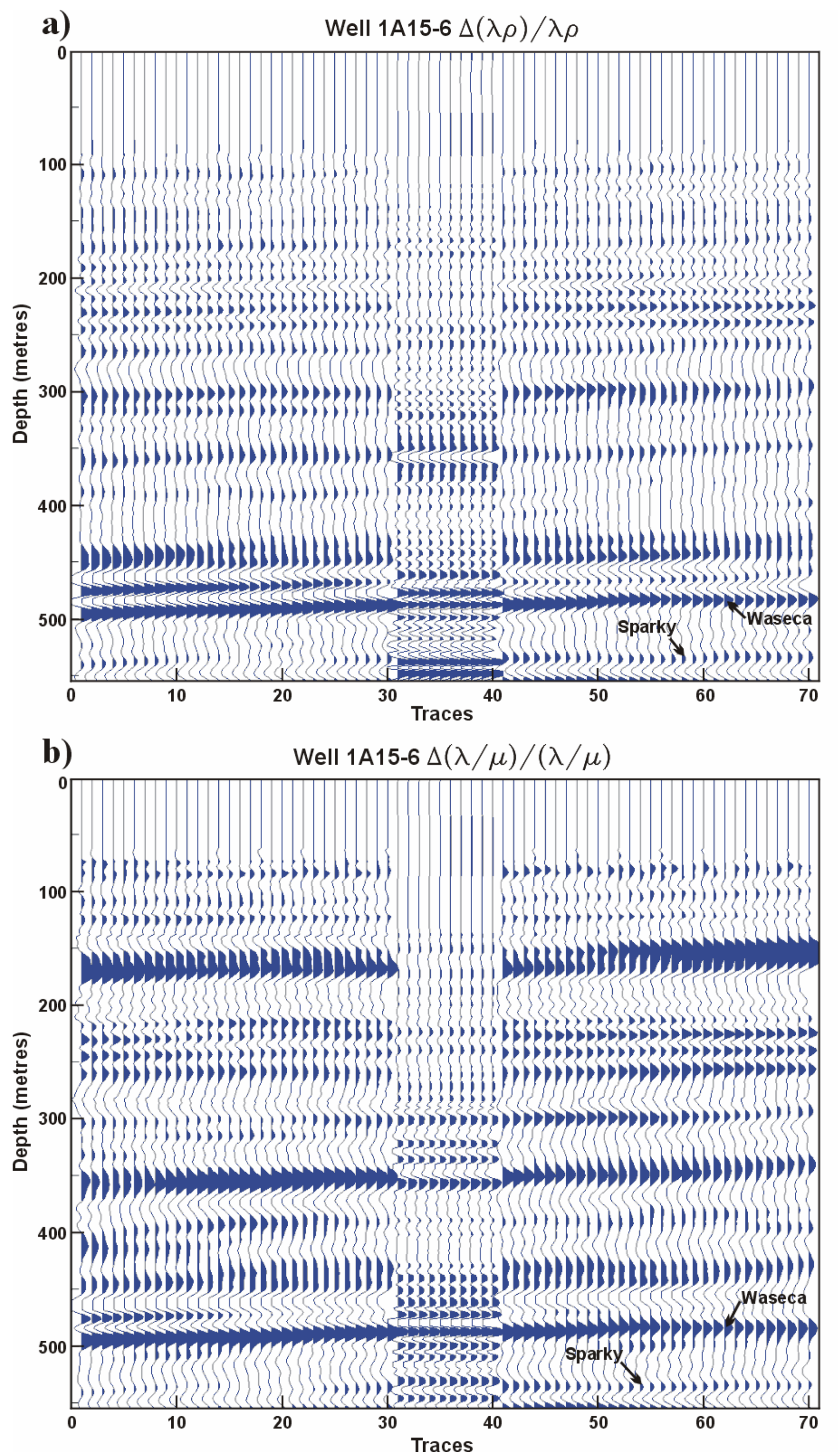

Figure 4.31: Comparison of a) $\Delta(\lambda\rho)/\lambda\rho$ and b) $\Delta(\lambda/\mu)/(\lambda/\mu)$ from 1A15-6 well-log computations with the simultaneous inversion. The seismic interval velocities were used in the time-depth conversion and well-log interval velocities were used in the inversion.

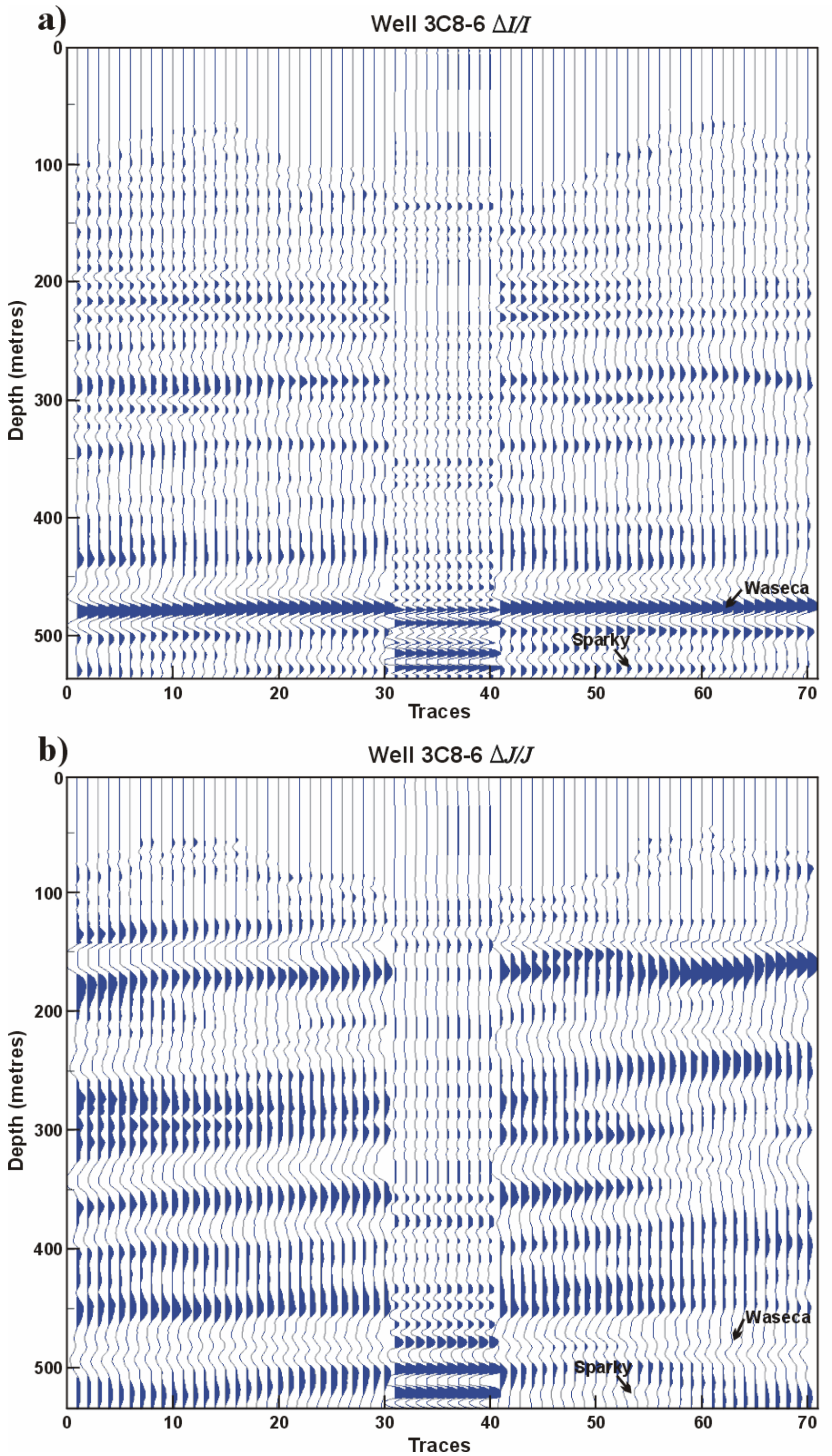

Figure 4.32: Comparison of a) $\Delta I/I$ and b) $\Delta J/J$ from 3C8-6 well-log computations with the simultaneous inversion. The seismic interval velocities were used in the time-depth conversion and well-log interval velocities were used in the inversion.

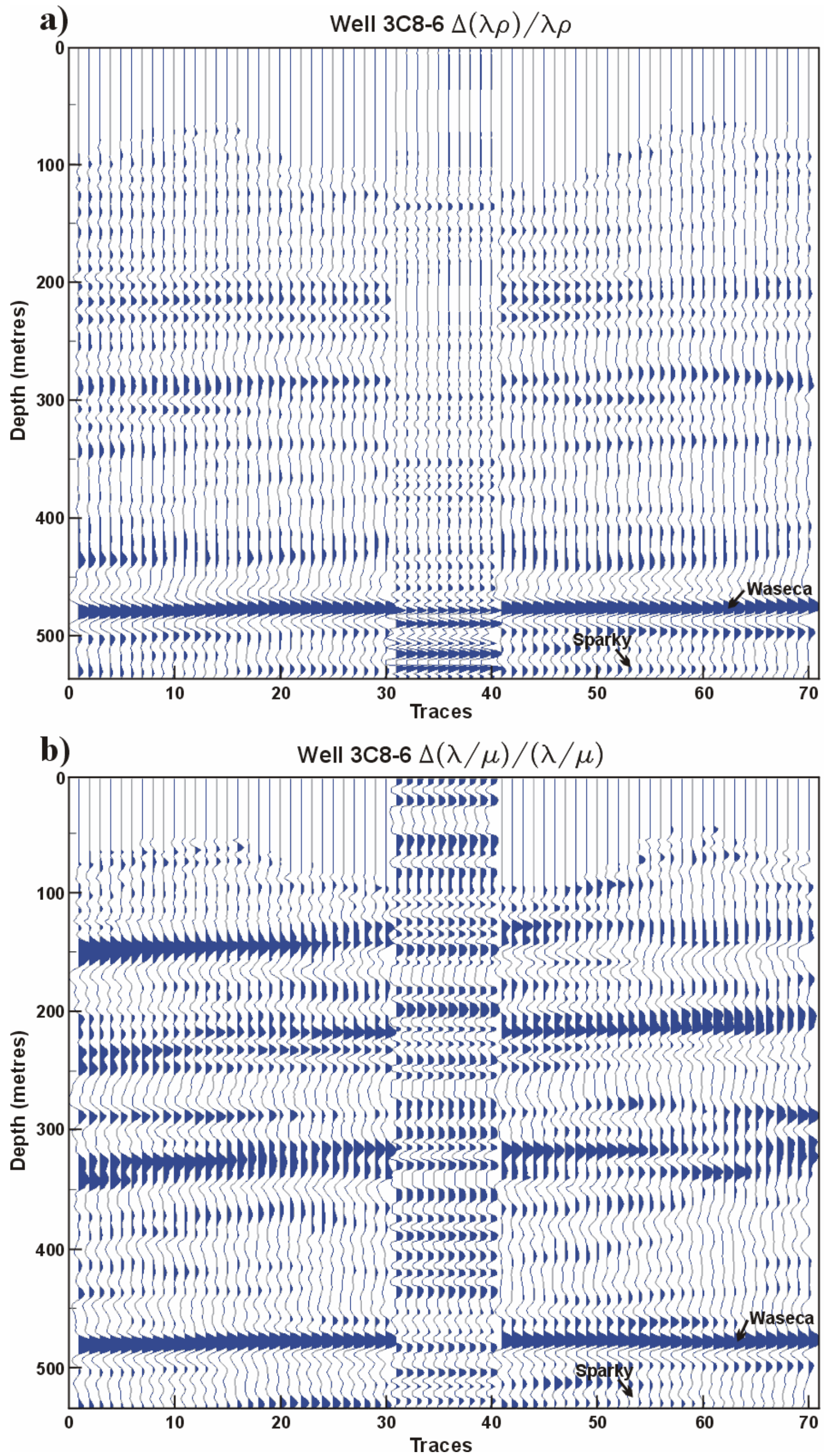

Figure 4.33: Comparison of a) $\Delta(\lambda\rho)/\lambda\rho$ and b) $\Delta(\lambda/\mu)/(\lambda/\mu)$ from 3C8-6 well-log computations with the simultaneous inversion. The seismic interval velocities were used in the time-depth conversion and well-log interval velocities were used in the inversion.

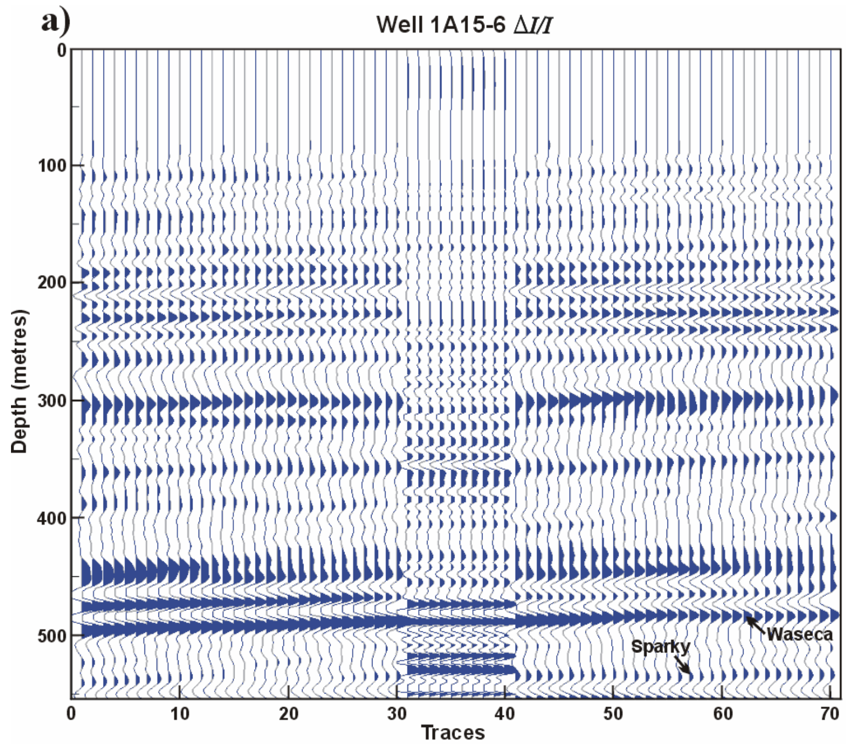

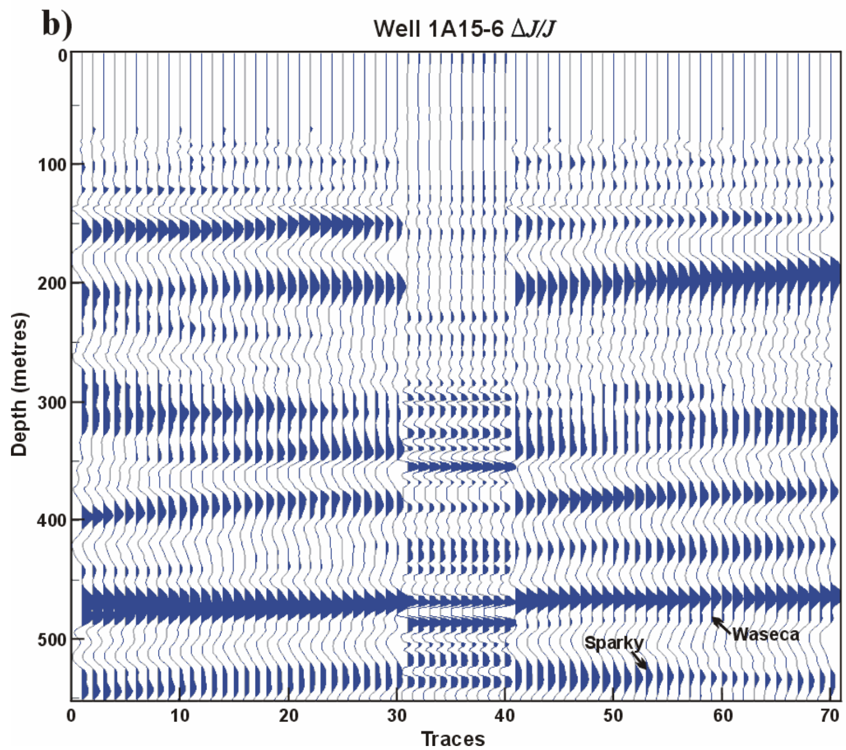

Figure 4.34: Comparison of a) $\Delta I/I$ and b) $\Delta J/J$ from 1A15-6 well-log computations with the simultaneous inversion. The seismic interval velocities were used in both the time-depth conversion and inversion.

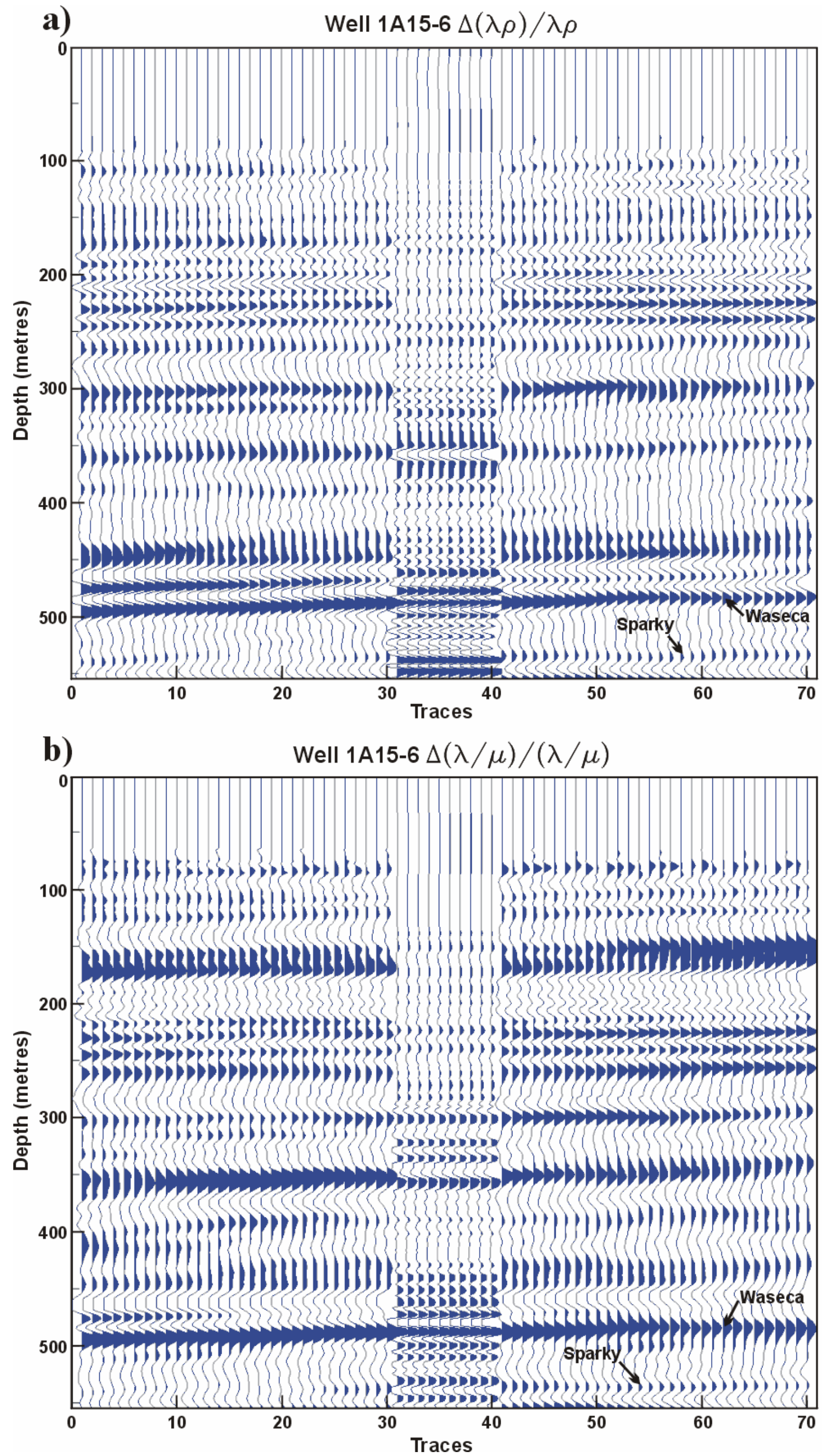

Figure 4.35: Comparison of a) $\Delta(\lambda\rho)/\lambda\rho$ and b) $\Delta(\lambda/\mu)/(\lambda/\mu)$ from 1A15-6 well-log computations with the simultaneous inversion. The seismic interval velocities were used in both the time-depth conversion and inversion.

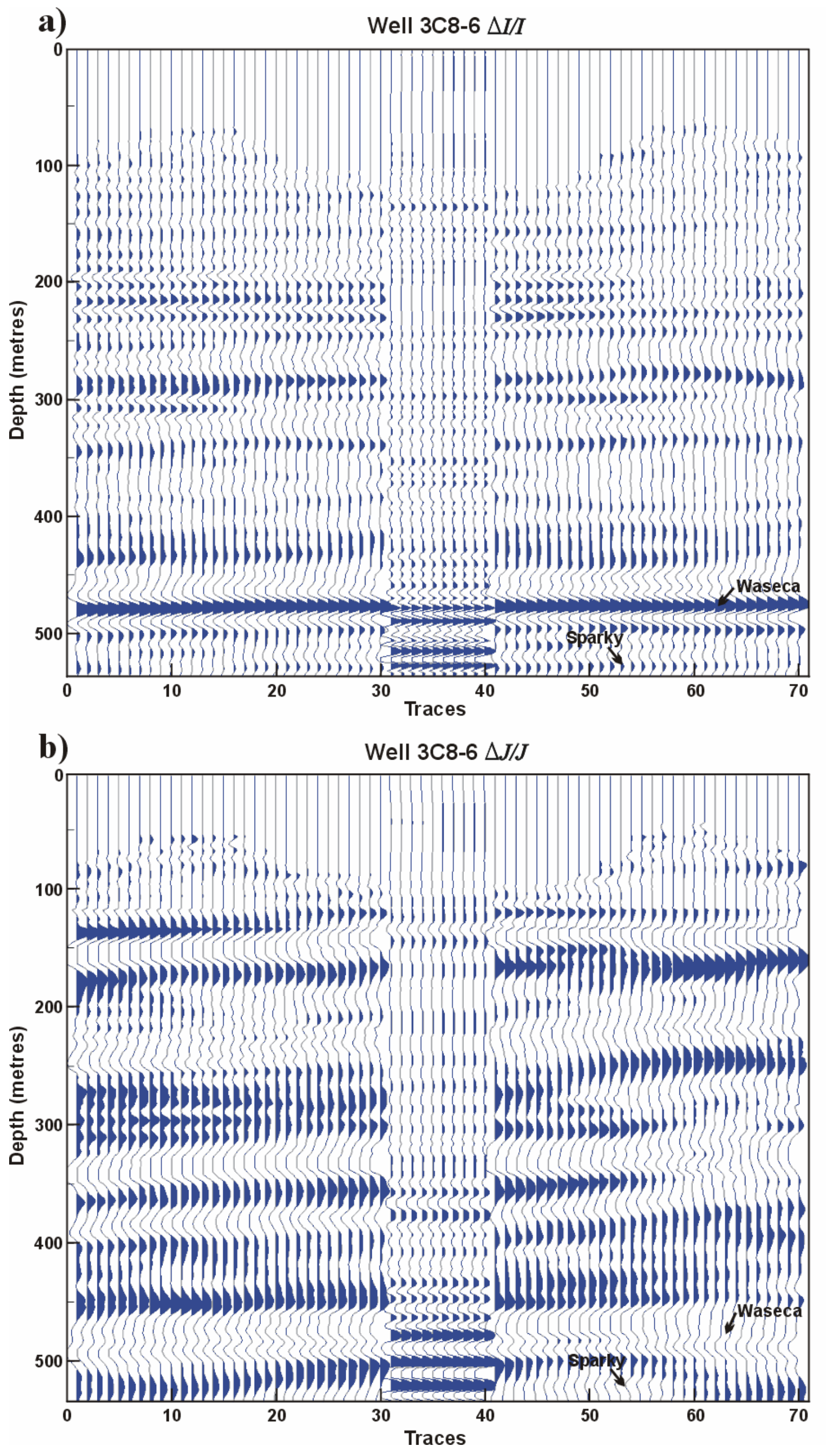

Figure 4.36: Comparison of a) $\Delta I/I$ and b) $\Delta J/J$ from 3C8-6 well-log computations with the simultaneous inversion. The seismic interval velocities were used in both the time-depth conversion and inversion.

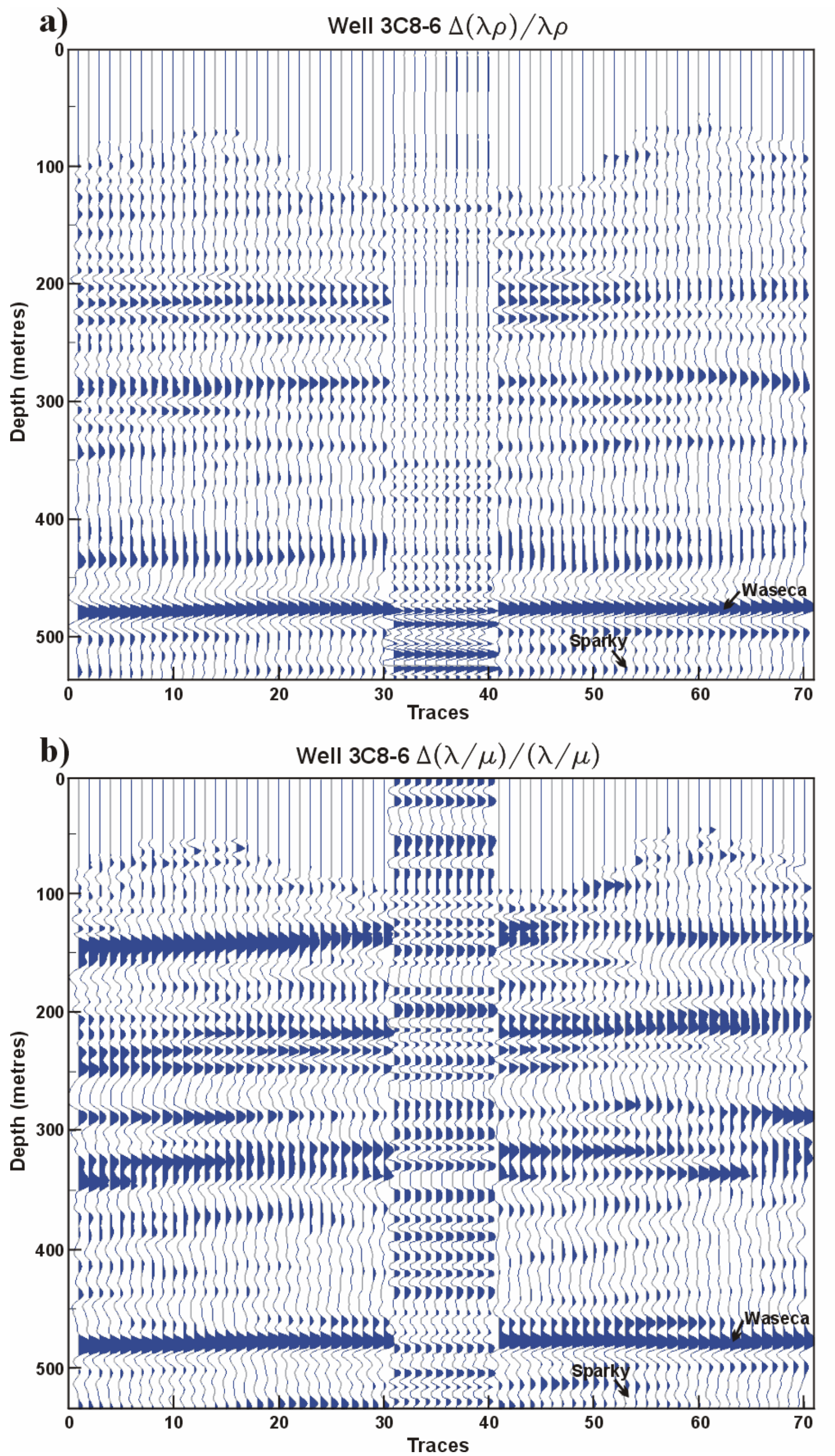

Figure 4.37: Comparison of a) $\Delta(\lambda\rho)/\lambda\rho$ and b) $\Delta(\lambda/\mu)/(\lambda/\mu)$ from 3C8-6 well-log computations with the simultaneous inversion. The seismic interval velocities were used in both the time-depth conversion and inversion.

This is a significant feature of the simultaneous inversion that makes it superior to the P-P stand-alone inversion. Figures 4.38-4.41 show how different depth shifts of P-S data affect the results of joint inversion, compared with the direct computation of the four attributes in well 1A15-6. For attributes $\Delta I/I$ and $\Delta(\lambda\rho)/(\lambda\rho)$, different depth shifts of P-S data give similar inversion results. But for attributes $\Delta J/J$ and $\Delta(\lambda/\mu)/(\lambda/\mu)$, different depth shifts of P-S data do lead to results of joint inversion with different imaging quality.

4.7 Comparison of PP-PS correlation with and without horizon flattening in the seismic section

In chapter 3, two methods of correlating P-P and P-S seismic data for the use of future inversion were discussed. One method utilizes an interpretive approach and matches P-P and P-S seismic data by V_P/V_S ratios in the time domain. The other method is to flatten the horizon that is right above the zone of interest in the P-P and P-S seismic data. This horizon is then shifted to the corresponding depth in the well, the calculated attributes of which will be compared with those resulting from the seismic inversion. Figures 4.42-4.45 show correlations of the direct well-log computations from wells 1A15-6 and 3C8-6 with the inverted four attributes with the Waseca top flattened. Figures 4.8a, 4.9a, 4.10a, 4.11a, 4.12a, 4.13a, 4.14a and 4.15a are the results of correlations without horizon flattening. Because of the simple geological structure, the results of the joint seismic inversion are good and correlate well with the well-log computations, regardless of whether the Waseca top is flattened or not.

4.8 Attribute analysis

Oil was found in all four wells. Except for well D15-6, they are good producing wells. In order to find out how the inverted attributes $\Delta I/I$, $\Delta J/J$, $\Delta(\lambda\rho)/(\lambda\rho)$ and $\Delta(\lambda/\mu)/(\lambda/\mu)$ from the joint inversion respond to changes in the lithology and porefluid, the average amplitude values of the seismic traces near the four wells on the $\Delta I/I$ and $\Delta J/J$ sections were drawn into the curves after correlating the results from the simultaneous inversion with well-log computations. In cases where there is obvious

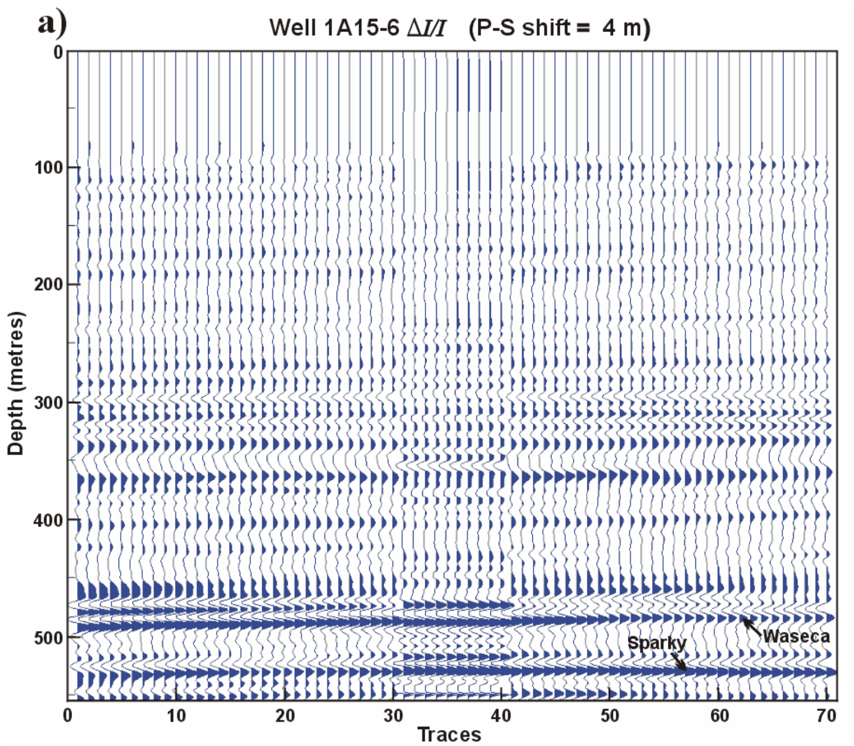

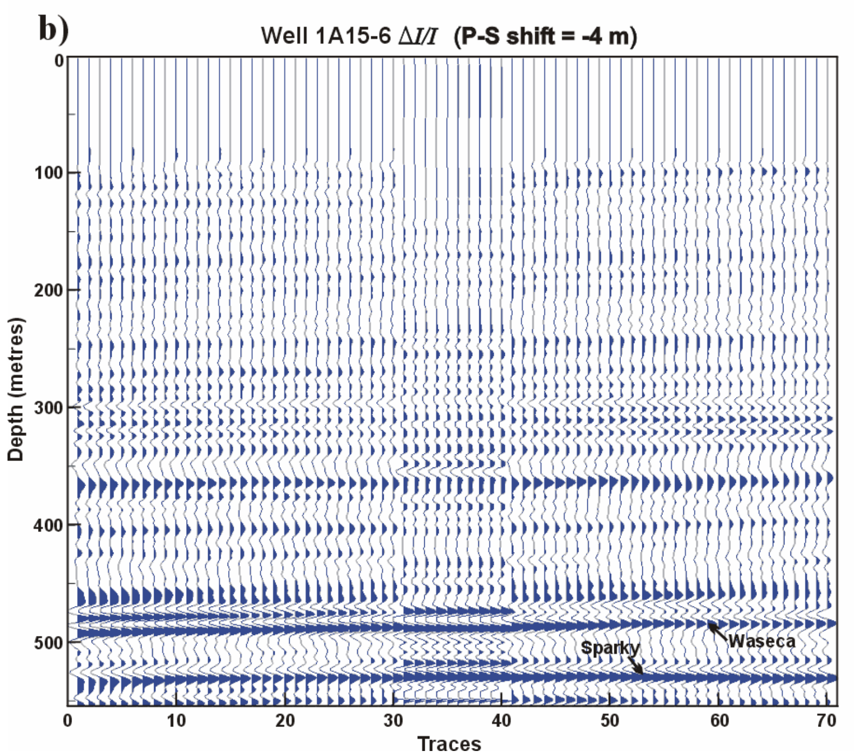

Figure 4.38: Comparison of $\Delta I/I$ from 1A15-6 well-log computation with $\Delta I/I$ from simultaneous inversion. In a) P-S data were shifted 4 m relative to the P-P data and in b) –4 m.

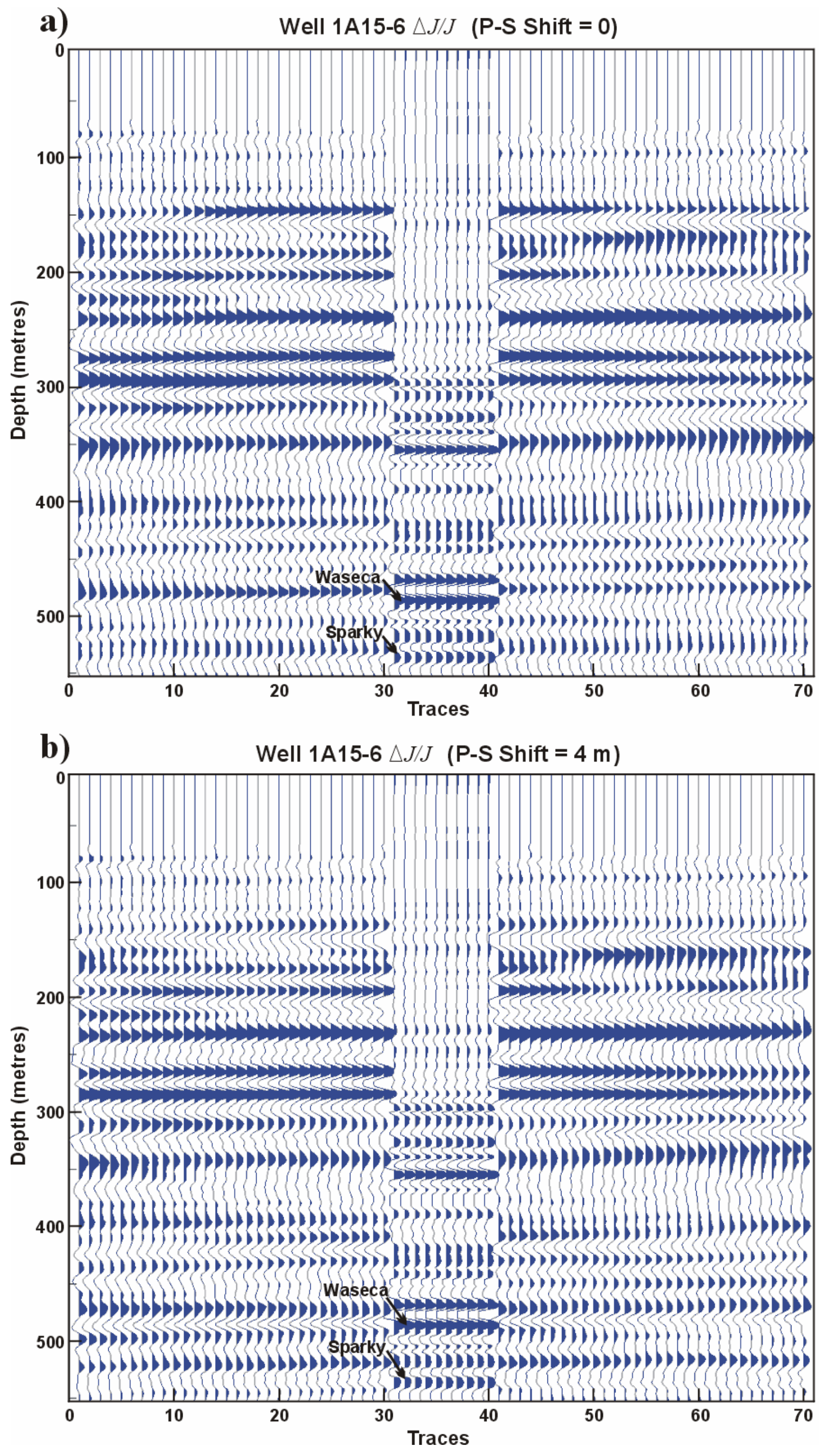

Figure 4.39: Comparison of $\Delta J/J$ from 1A15-6 well-log computation with $\Delta J/J$ from simultaneous inversion. In a) P-S data were shifted 0 m relative to the P-P data and in b) 4 m.

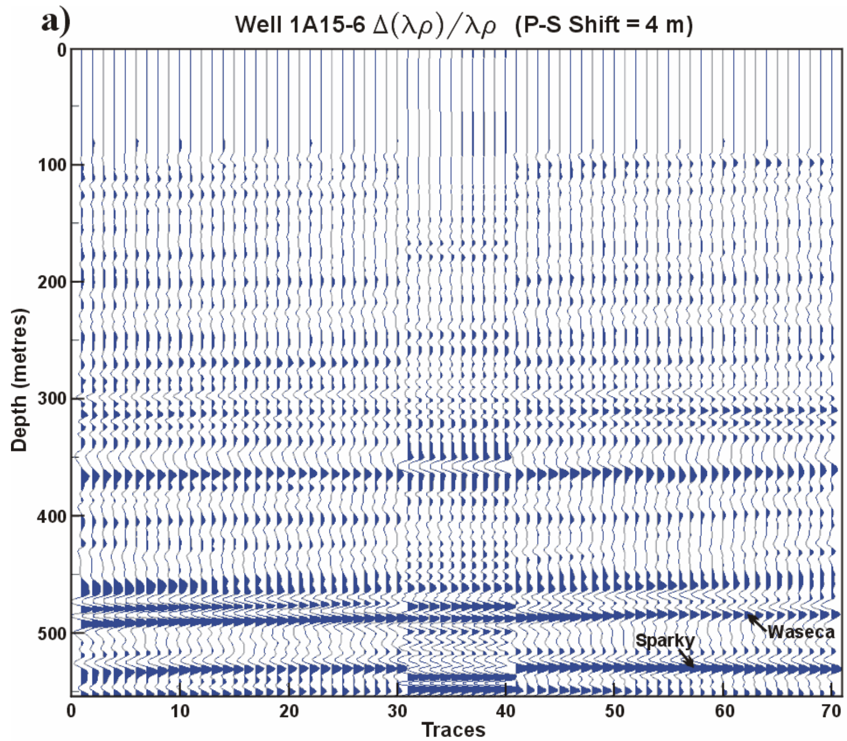

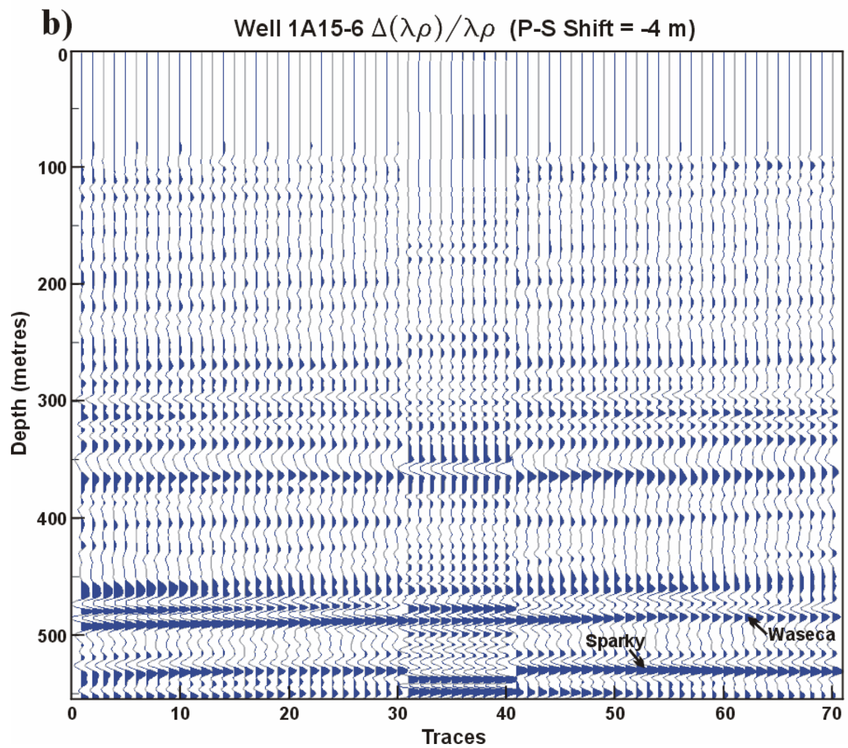

Figure 4.40: Comparison of $\Delta(\lambda\rho)/\lambda\rho$ from 1A15-6 well-log computation with $\Delta(\lambda\rho)/\lambda\rho$ from simultaneous inversion. In a) P-S data were shifted 4 m relative to the P-P data and in b) -4 m.

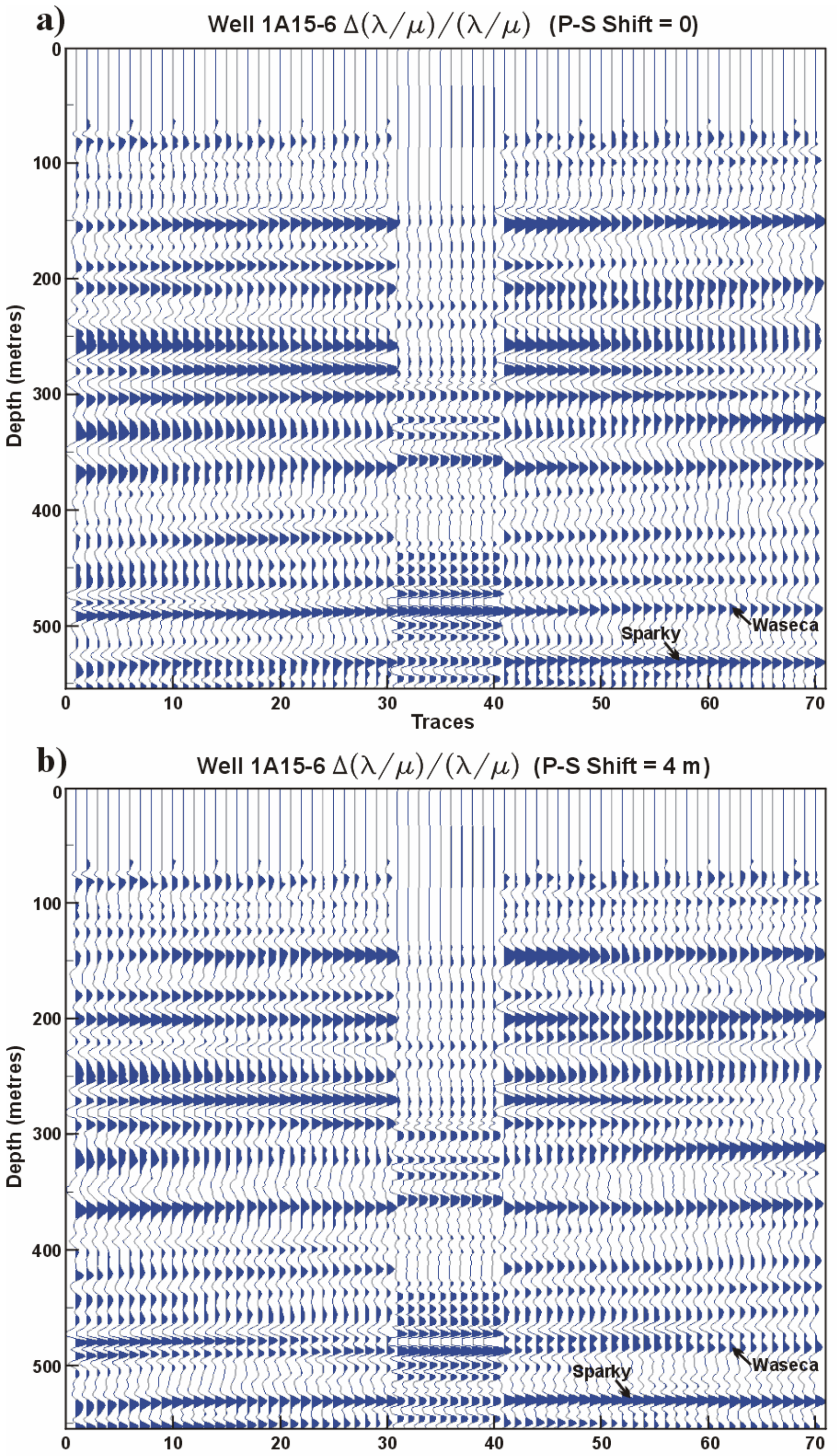

Figure 4.41: Comparison of $\Delta(\lambda/\mu)/(\lambda/\mu)$ from 1A15-6 well-log computation with $\Delta(\lambda/\mu)/(\lambda/\mu)$ from simultaneous inversion. In a) P-S data were shifted 0 m relative to the P-P data and in b) 4 m.

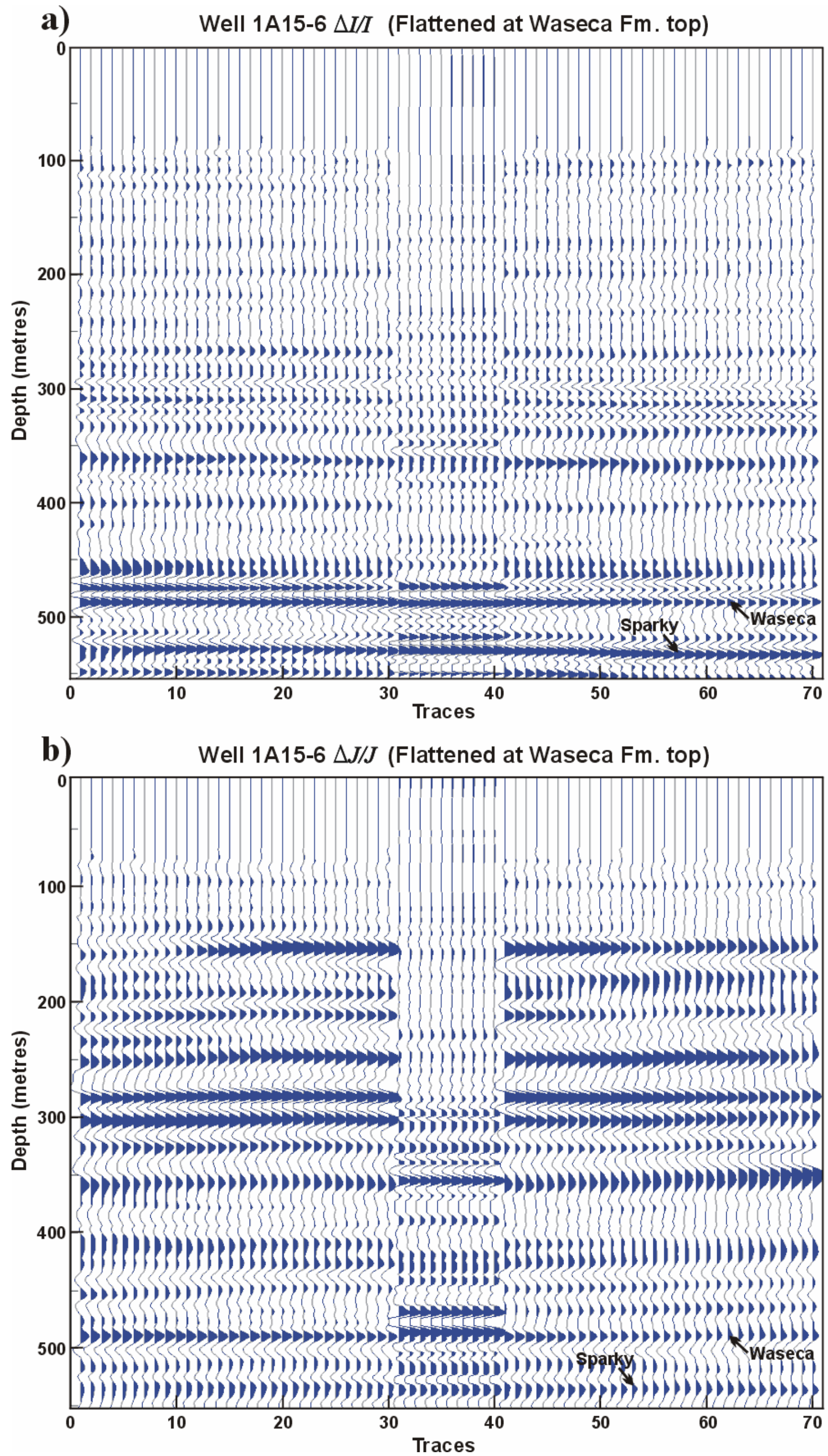

Figure 4.42: Comparison of a) $\Delta I/I$ and b) $\Delta J/J$ from 1A15-6 well-log computations with the same from simultaneous inversion. The Waseca top was flattened.

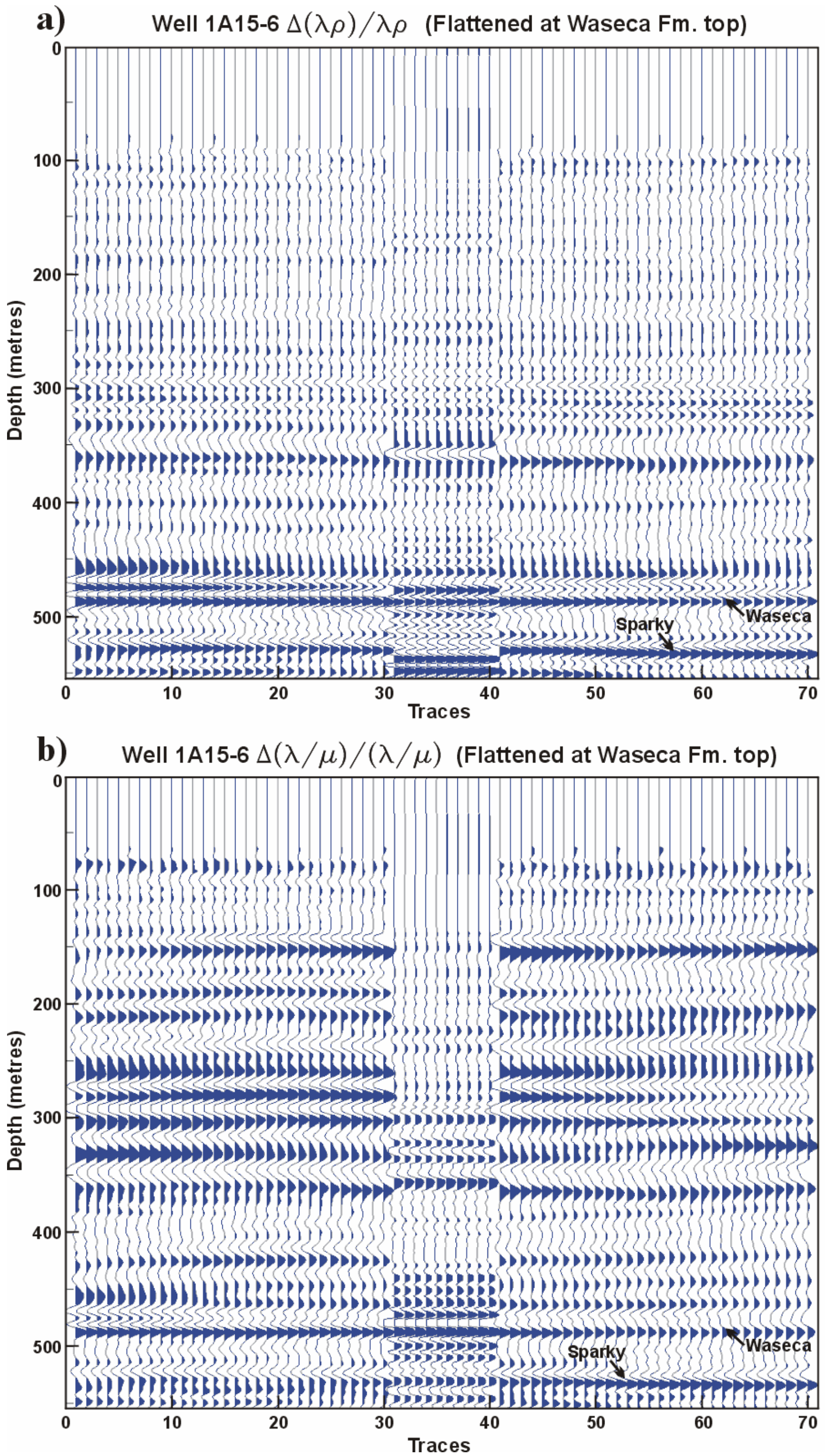

Figure 4.43: Comparison of a) $\Delta(\lambda\rho)/\lambda\rho$ and b) $\Delta(\lambda/\mu)/(\lambda/\mu)$ from 1A15-6 well-log computations with the same from simultaneous inversion. The Waseca top was flattened.

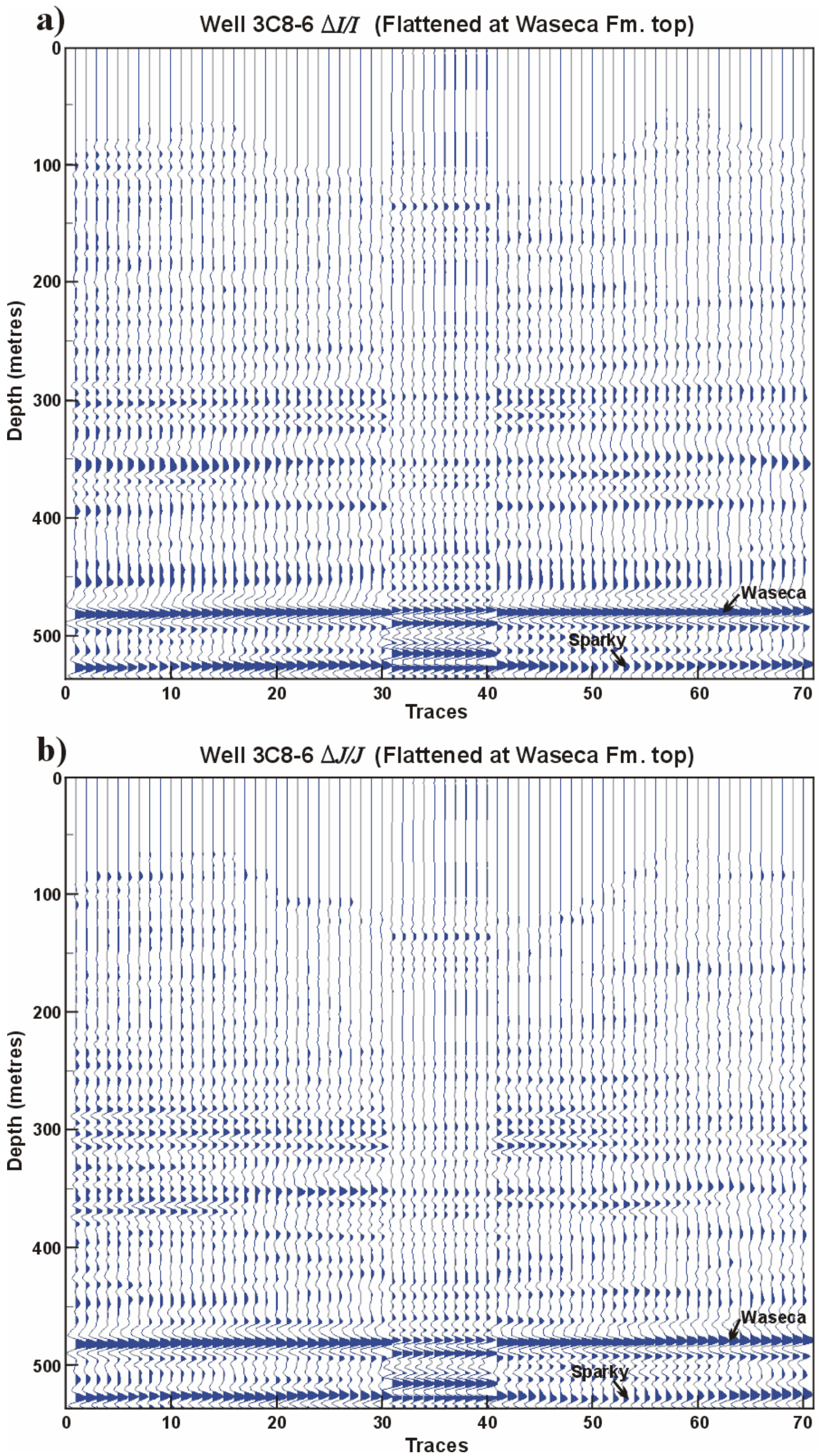

Figure 4.44: Comparison of a) $\Delta I/I$ and b) $\Delta J/J$ from 3C8-6 well-log computations with the same from simultaneous inversion. The Waseca top was flattened.

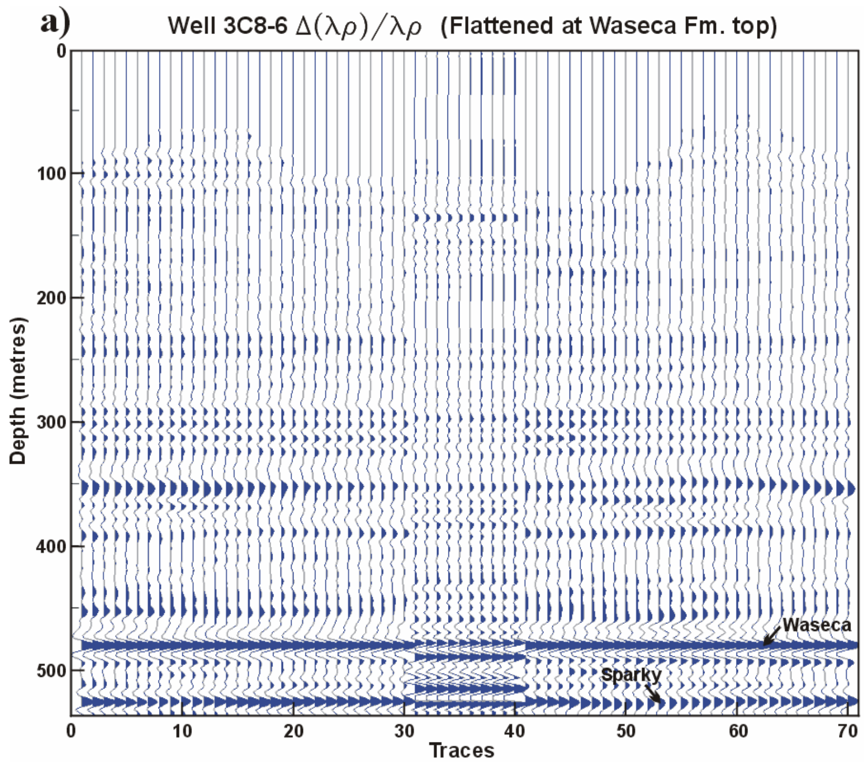

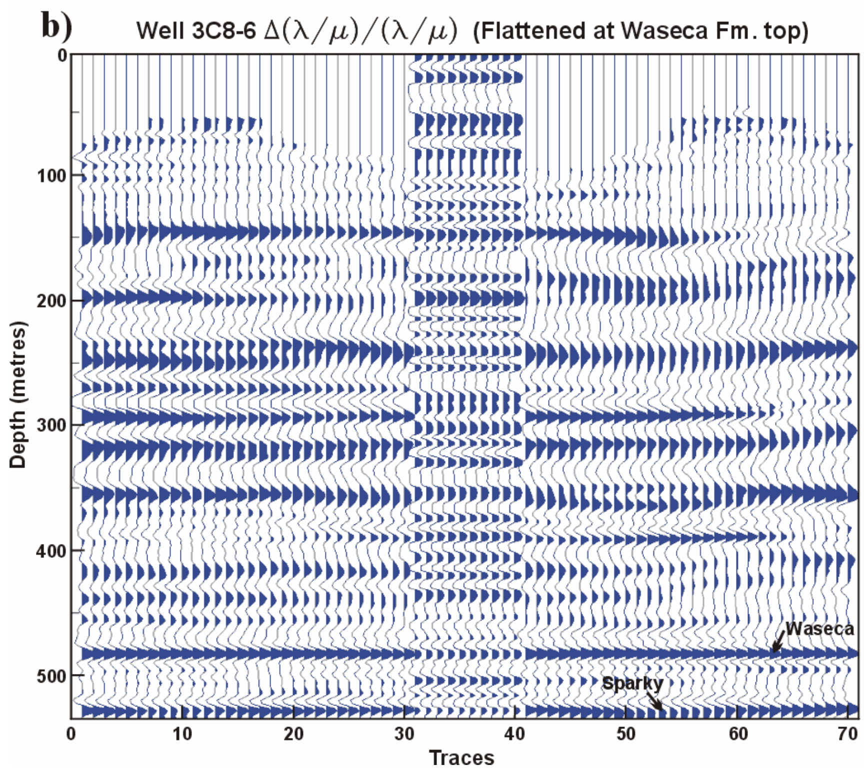

Figure 4.45: Comparison of a) $\Delta(\lambda\rho)/\lambda\rho$ and b) $\Delta(\lambda/\mu)/(\lambda/\mu)$ from 3C8-6 well-log computations with the same from simultaneous inversion. The Waseca top was flattened.

channel deposition, the seismic traces within the channel were averaged. The same procedure was carried out on $\Delta(\lambda\rho)/\lambda\rho$ and $\Delta(\lambda/\mu)/(\lambda/\mu)$ sections. The changes in the average amplitude values with the changes of lithology and porefluid were investigated.

In figures 4.46a and c and 4.47a and c, the solid red curves and the dashed blue curves are, respectively, the amplitude values of $\Delta I/I$ and $\Delta J/J$. In figures 4.46b and d and 4.47b and d, the solid pink curves and the dashed cyan curves are, respectively, $\Delta(\lambda\rho)/\lambda\rho$ and $\Delta(\lambda/\mu)/(\lambda/\mu)$. We notice that when the type of lithology is mainly shale, the amplitudes of $\Delta J/J$ are greater than those of $\Delta I/I$ because of smaller elastic acoustic impedance contrast. As we approach the zone of interest, the Waseca Fm, where the sideritic shale, coal and sandstone dominate, the amplitudes of these two attributes become very close because of the more dramatic increase in the amplitude of $\Delta I/I$ than $\Delta J/J$. The shear velocity increases more dramatically than P-wave velocity at the top of the McLaren Fm, where there is a thin coal layer, and decreases in places where there is pore liquid such as oil. P-wave velocity does not decrease as much in oil but it does change more dramatically in the zone of interest where there is sand, shale and oil. It is also possible that the much lower frequencies of the P-S reflectivity compromise the dramatic change in the shear velocity. That is why sometimes the amplitude values of $\Delta I/I$ appear to be similar or even greater than those of $\Delta J/J$. Generally, the response of $\Delta(\lambda\rho)/\lambda\rho$ and $\Delta(\lambda/\mu)/(\lambda/\mu)$ are similar to $\Delta I/I$ and $\Delta J/J$, respectively. The trend mentioned above is not exactly consistent with the direct well-log computations of these attributes (figure 4.48 and 4.49). But there is an obvious increase in the amplitude of $\Delta I/I$, $\Delta J/J$ and $\Delta(\lambda/\mu)/(\lambda/\mu)$ in all four wells when the dominating lithology changes from shale to sand and coal.

In figures 4.50-4.53, we zoom in on Waseca Fm on these curves. In places where the oil zones are, all the four inverted attributes appear as troughs. What is more, $\Delta I/I$ and $\Delta(\lambda/\mu)/(\lambda/\mu)$ change more dramatically than $\Delta J/J$ and $\Delta(\lambda\rho)/\lambda\rho$ when the oil zone appears in the homogeneous sand around wells 1A15-6, 3C8-6 and D2-6 that have

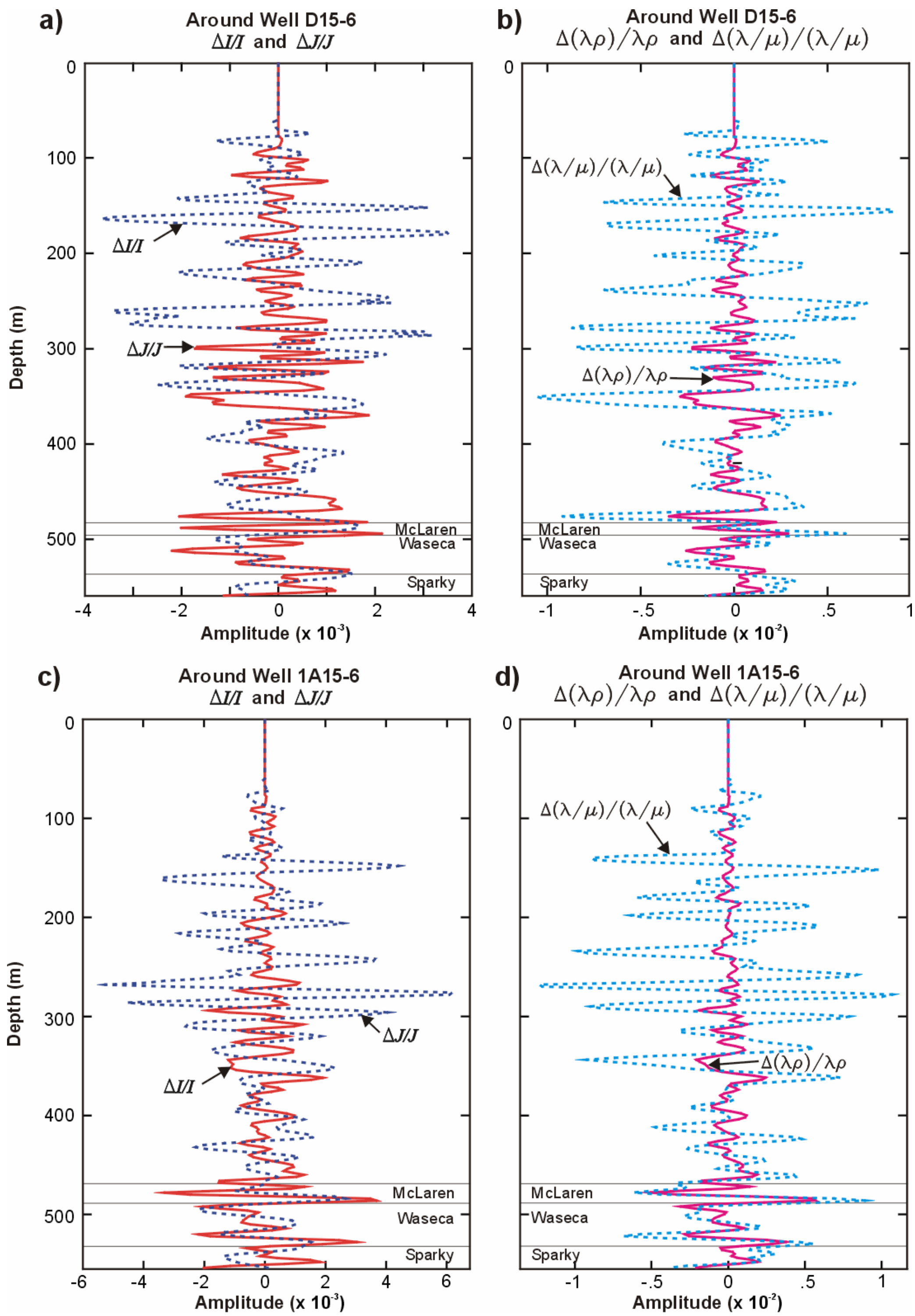

Figure 4.46: a) and c) are average amplitude values of $\Delta I/I$ and $\Delta J/J$ from traces around well D15-6 and 1A15-6; b) and d) are average amplitude values of $\Delta(\lambda\rho)/\lambda\rho$ and $\Delta(\lambda/\mu)/(\lambda/\mu)$ from traces around well D15-6 and 1A15-6.

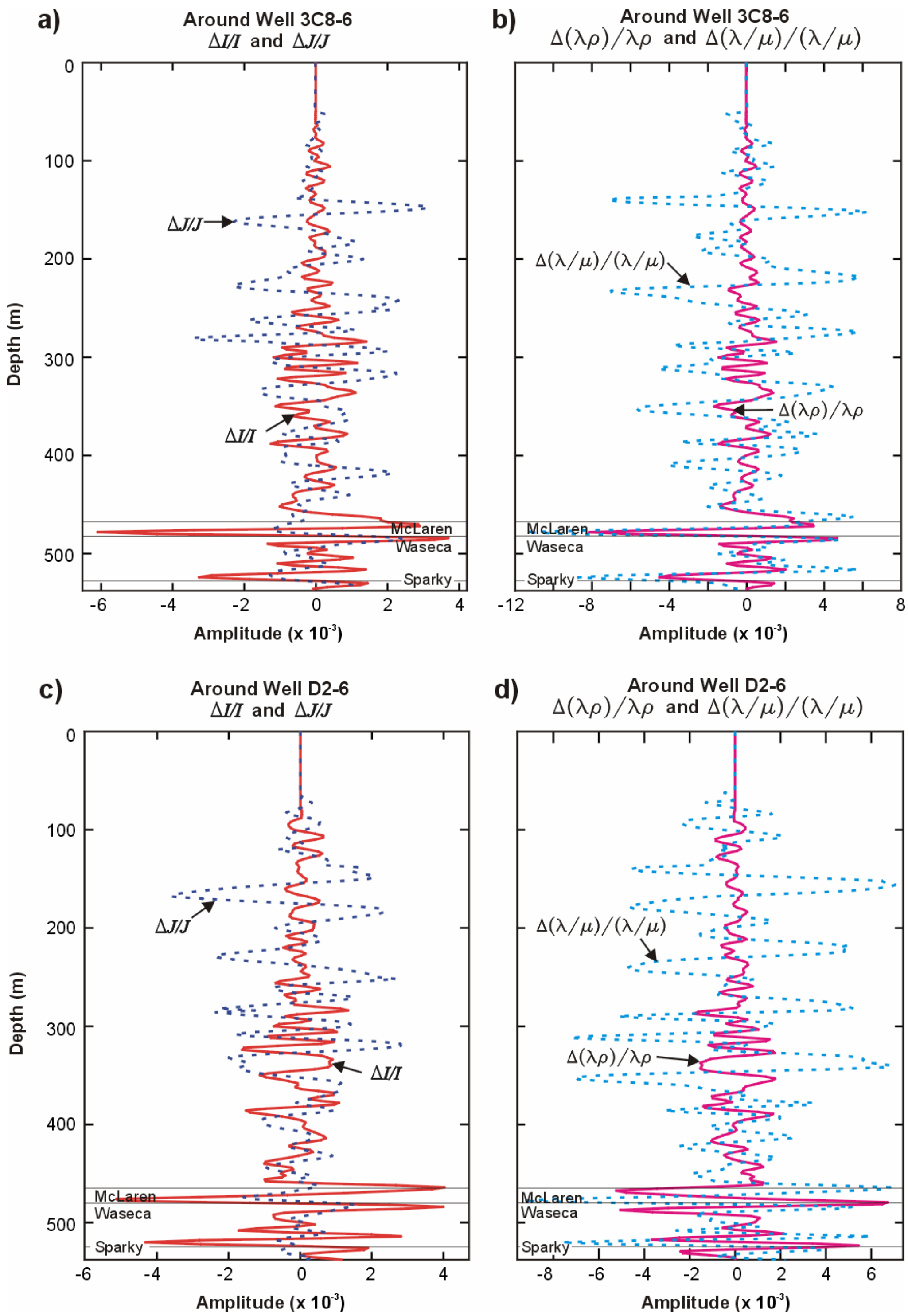

Figure 4.47: a) and c) are average amplitude values of $\Delta I/I$ and $\Delta J/J$ from traces around well 3C8-6 and D2-6; b) and d) are average amplitude values of $\Delta(\lambda\rho)/\lambda\rho$ and $\Delta(\lambda/\mu)/(\lambda/\mu)$ from traces around well 3C8-6 and D2-6.

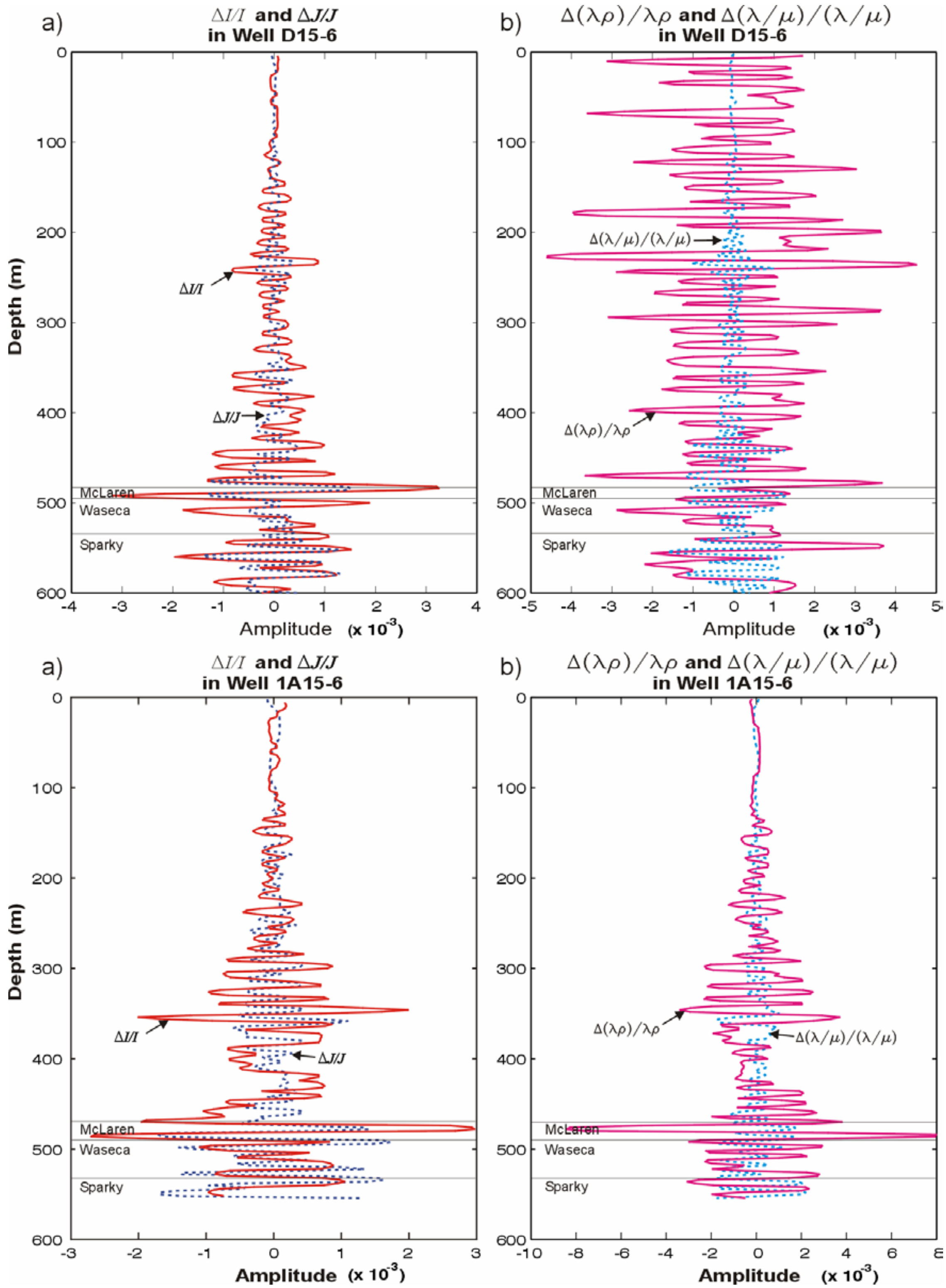

Figure 4.48: Attributes $\Delta I/I$, $\Delta J/J$, $\Delta(\lambda\rho)/\lambda\rho$, and $\Delta(\lambda/\mu)/(\lambda/\mu)$ resulting from direct well-log computations in a) and b) well D15-6, and in c) and d) well 1A15-6.

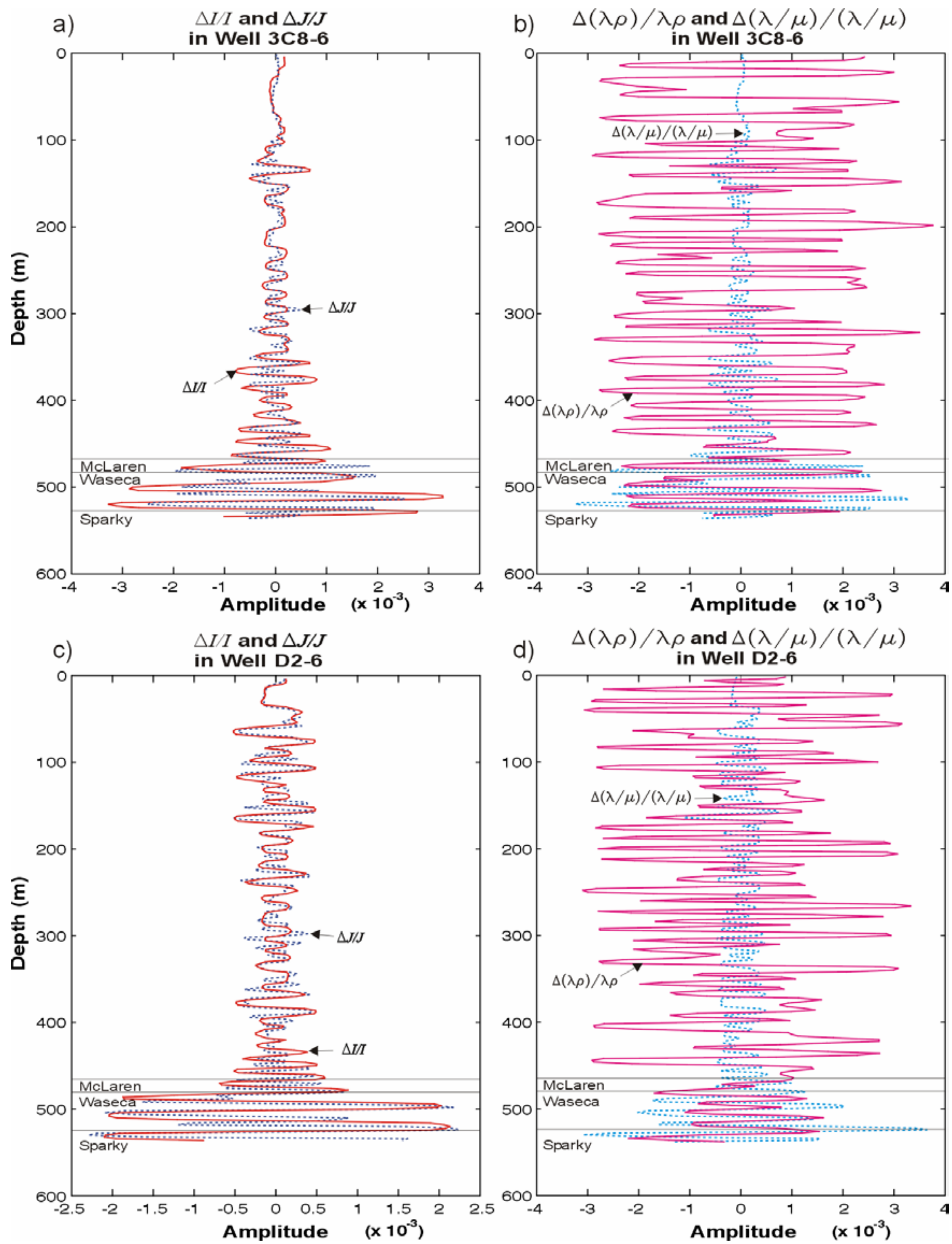

Figure 4.49: Attributes $\Delta I/I$, $\Delta J/J$, $\Delta(\lambda\rho)/\lambda\rho$, and $\Delta(\lambda/\mu)/(\lambda/\mu)$ resulting from direct well-log computations in a) and b) well 3C8-6, and in c) and d) well D2-6.

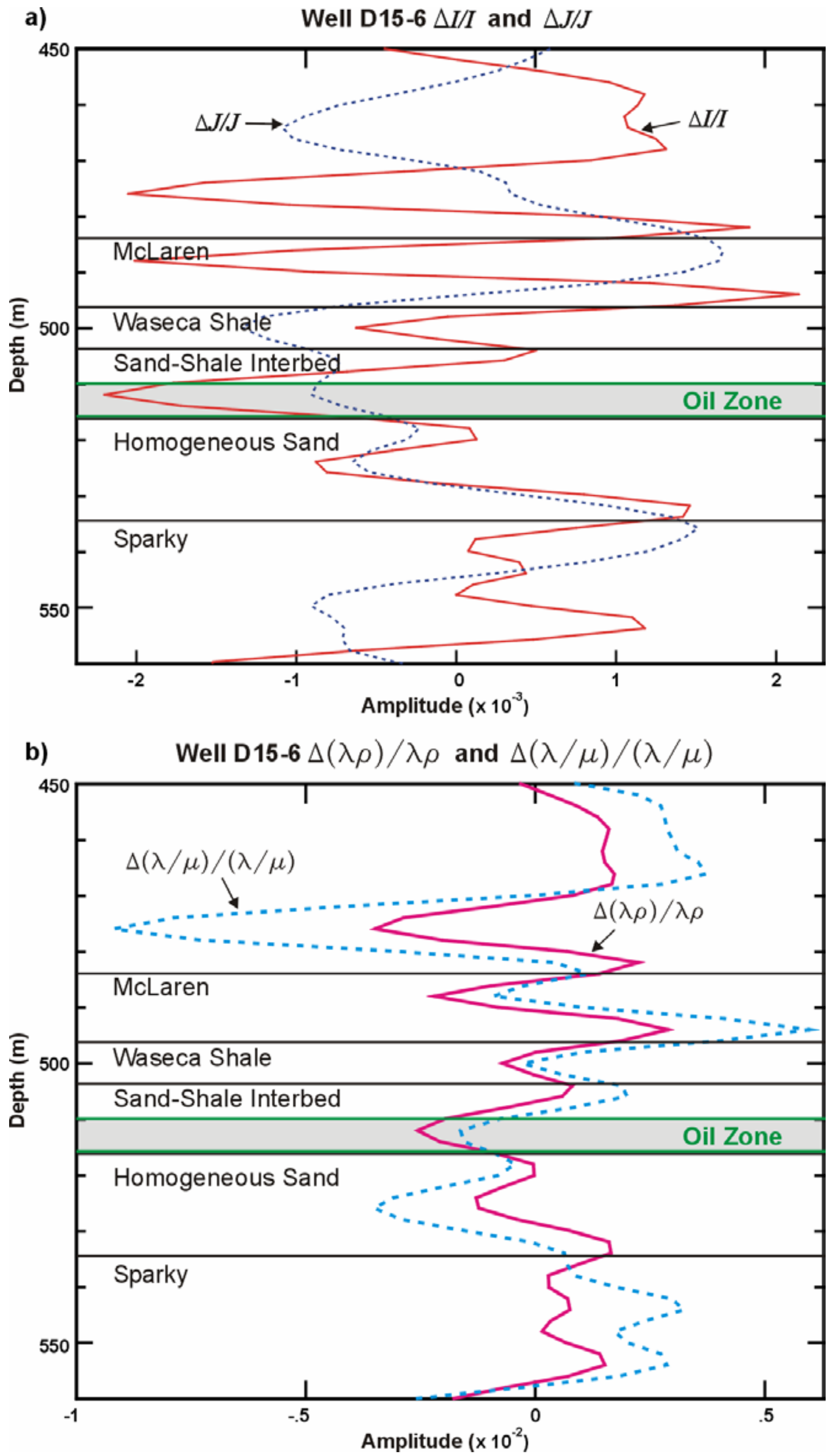

Figure 4.50: Expanded attribute curves of $\Delta I/I$, $\Delta J/J$, $\Delta(\lambda\rho)/\lambda\rho$, and $\Delta(\lambda/\mu)/(\lambda/\mu)$ in well D15-6.

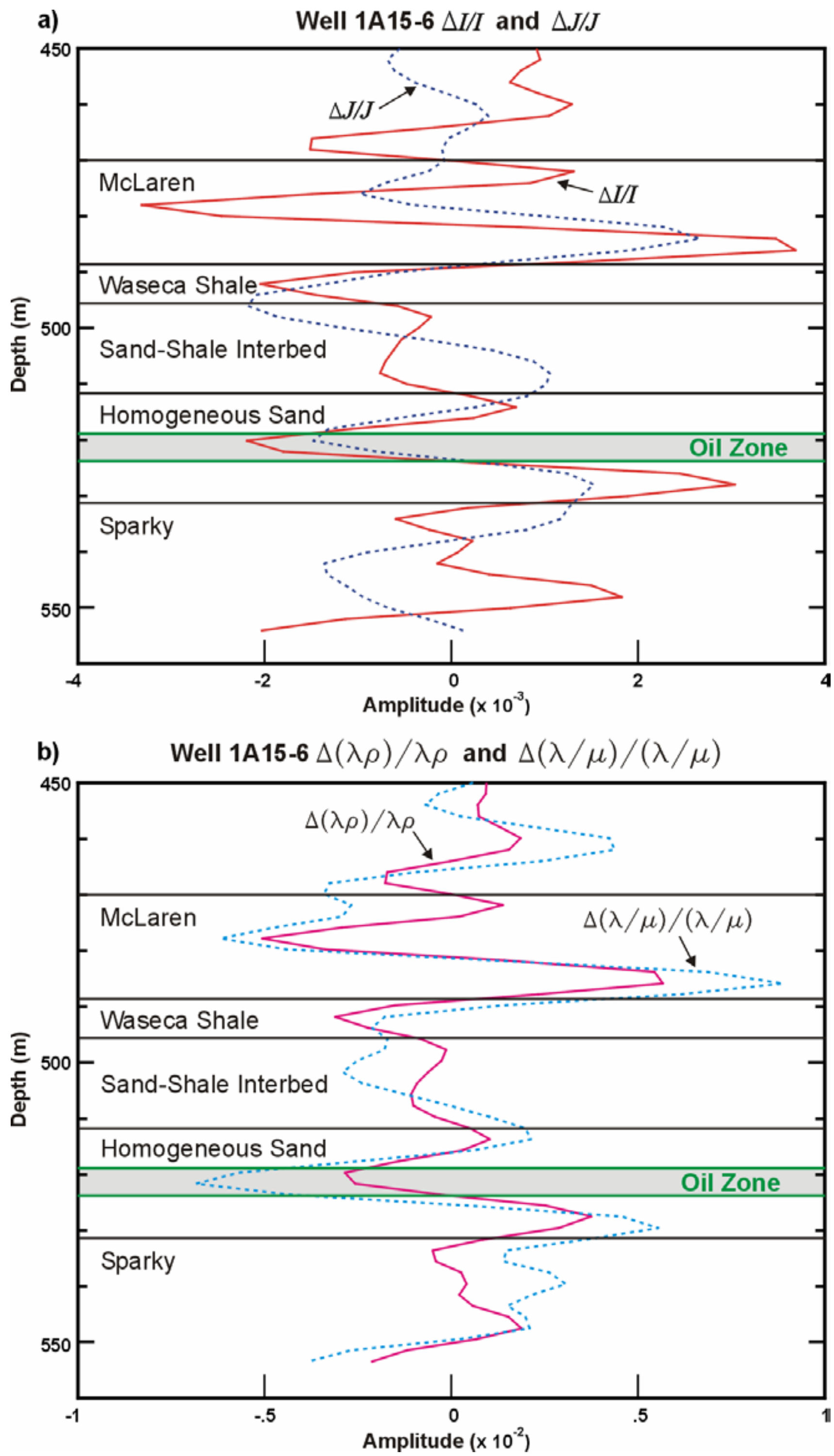

Figure 4.51: Expanded attribute curves of $\Delta I/I$, $\Delta J/J$, $\Delta(\lambda\rho)/\lambda\rho$, and $\Delta(\lambda/\mu)/(\lambda/\mu)$ in well 1A15-6.

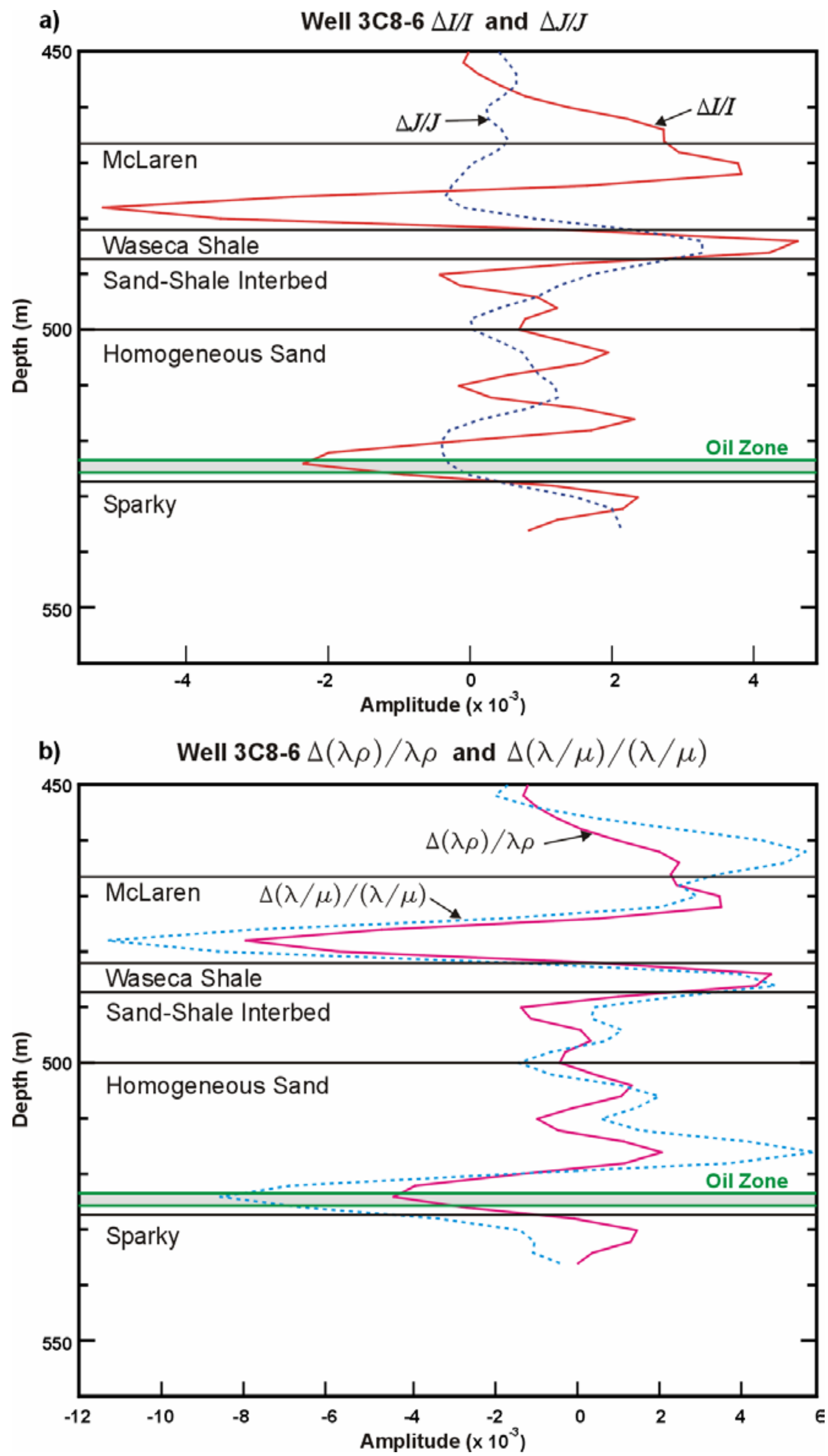

Figure 4.52: Expanded attribute curves of $\Delta I/I$, $\Delta J/J$, $\Delta(\lambda\rho)/\lambda\rho$, and $\Delta(\lambda/\mu)/(\lambda/\mu)$ in well 3C8-6.

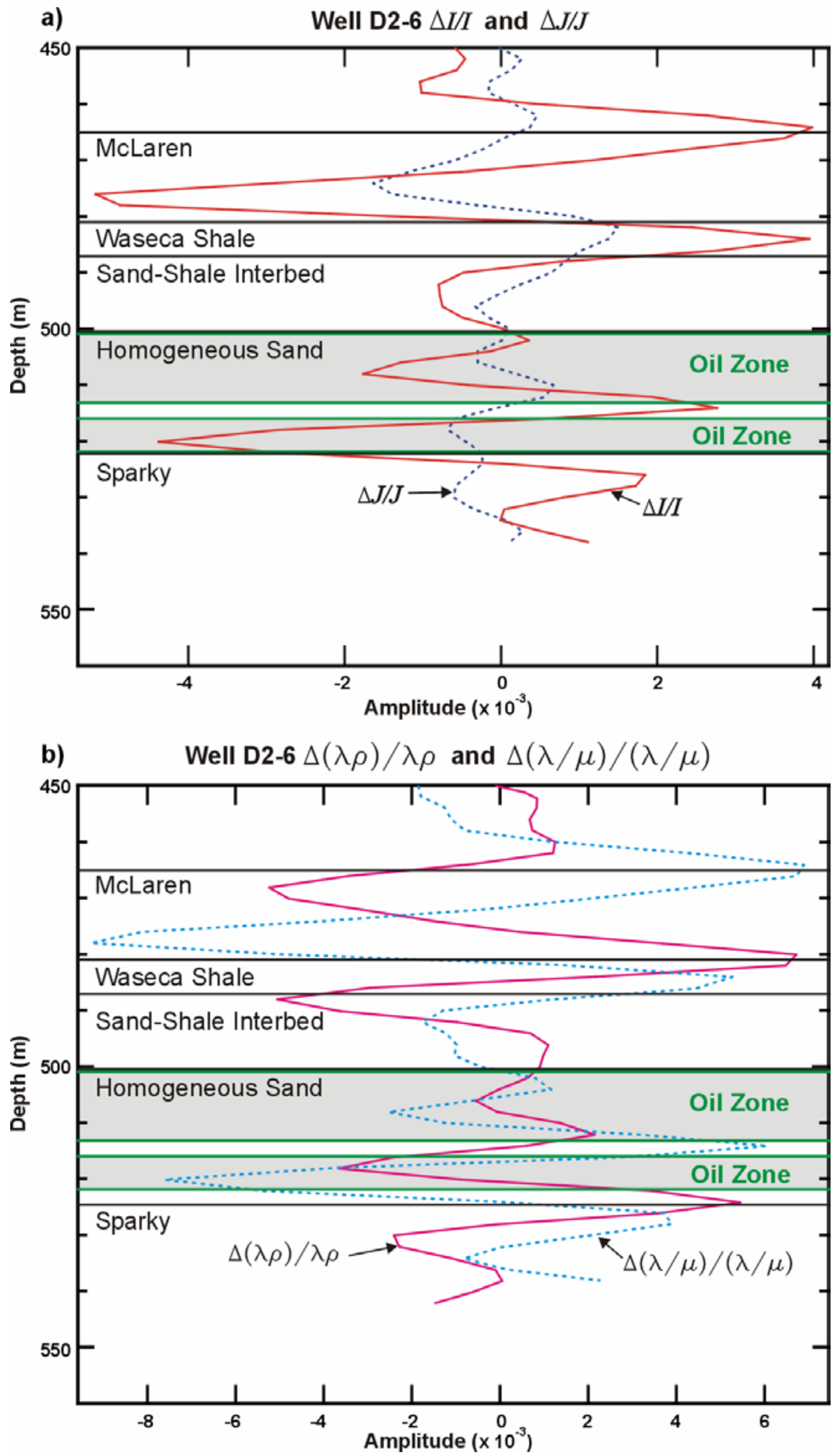

Figure 4.53: Expanded attribute curves of $\Delta I/I$, $\Delta J/J$, $\Delta(\lambda\rho)/\lambda\rho$, and $\Delta(\lambda/\mu)/(\lambda/\mu)$ in well D2-6.

higher producing rate. In comparison, the amplitude of $\Delta(\lambda\rho)/\lambda\rho$ is greater than $\Delta(\lambda/\mu)/(\lambda/\mu)$ when the oil zone appears in the sand-shale interbed around well D15-6.

4.9 Chapter summary

In order to judge how effective the joint PP-PS AVO inversion is, it is necessary to compare direct well-log computations with the attributes resulting from the joint inversion and P-wave-only inversion. The method of calculating the fractional impedance contrast from well logs was introduced. Despite the fact that the well logs were downsampled and smoothed before the calculation, the attributes still had to be bandpass-filtered according to the frequency band of the estimates from seismic inversion. By virtue of better and more coherent correlation between direct well-log computations and the joint inversion, it is concluded that the joint inversion works in this case and is superior to P-wave-only inversion.

The velocities derived from seismic and well logs were tested in the time-depth conversion and the inversion. The joint inversion using velocities from well logs ties to well control better. Accurate velocities for the joint inversion are important. Allowing the relative shift in depth until the optimal match between the seismic events on P-P and P-S data is achieved is another feature that makes the joint inversion superior to P-wave-only inversion. An approximate method to match the events within a small range of depth is to flatten a certain horizon on both P-P and P-S data and shift the two flattened horizon to the same depth. In the inversion of Pikes Peak data, no horizon flattening is needed because the structure is simple and the depth range for the inversion is from depth zero to about 600 m. Besides the fact that the joint inversion fits the interpretation better than P-wave-only inversion by providing more information, it can also be inferred that $\Delta I/I$ and $\Delta(\lambda/\mu)/(\lambda/\mu)$ are more sensitive to heavy oil than $\Delta J/J$ and $\Delta(\lambda\rho)/\lambda\rho$ by observing the amplitude values of the four inverted attributes.

CHAPTER 5

CONCLUSIONS AND DISCUSSION

5.1 Conclusions

I conducted a joint P-P and P-S inversion on a 3C-2D seismic line over the Pikes Peak field. The inversion required forming migrated, limited-offset sections for both P-P and P-S data and creating synthetic seismograms from well control.

Approximate regional amplitude restoration of the seismic data was accomplished by equalizing their RMS amplitudes with those of the synthetic seismograms for each offset. I then estimated fractional P and S impedance contrasts by forming weighted stacks of the migrated, limited-offset sections. The success of the inversion was judged by comparing the estimated fractional impedance contrasts with direct calculations from wells.

The module of joint PP-PS AVO inversion in ProMAX is designed to allow the P-S seismic data to be shifted in depth relative to the P-P data so that an optimal event correlation between P-P and P-S data can be achieved. Thus, an optimal result of inversion can be obtained. By virtue of good correlation between seismic inversion and well-log computation, it is concluded that the method of joint PP-PS AVO inversion worked reasonably well in this case. This is also proven helpful in indicating anomalous lithology and pore-fluid changes in the subsurface and, thereby, in oil and gas exploration, since information contained in both P-wave and S-wave seismic data is utilized in detecting these seismic anomalies.

In the estimation of such attributes as $\Delta J/J$ and $\Delta(\lambda/\mu)/(\lambda/\mu)$ that are more vulnerable to coherent noise, the simultaneous PP-PS AVO inversion method is significantly more accurate than the P-P stand-alone inversion method. This is probably because the data fold incorporated in the estimation of each attribute is doubled when both P-P and P-S seismic data are utilized in the joint inversion and the weighting method is modified to weight each offset more equally so that in effect, the data fold is increased further for each weighted attribute stack. Following the same logic, the addition of other seismic reflection modes such as S-S and S-P should improve the performance of the simultaneous inversion method even more in the presence of coherent noise.

The imaging of the channel sequence in the Waseca Fm has also been enhanced, especially in $\Delta I/I$ and $\Delta(\lambda\rho)/\lambda\rho$, as a result of performing simultaneous inversion as opposed to the P-P stand-alone inversion. In fact, this enhancement is welcome because the channel sequence feature is not obvious or complete in the same inverted attributes resulting from the P-P stand-alone inversion.

The strength mentioned above makes joint PP-PS AVO inversion a superior method in the oil and gas exploration and reservoir development. Meanwhile, there are weaknesses in this method. For example, it seems that joint PP-PS AVO inversion cannot add in the higher frequencies to the estimates $\Delta J/J$ and $\Delta(\lambda/\mu)/(\lambda/\mu)$ effectively according to the input P-P seismic data that usually have higher frequencies than P-S seismic data. In other words, $\Delta J/J$ and $\Delta(\lambda/\mu)/(\lambda/\mu)$ are excessively dependent upon P-S reflectivity. Hence, the detailed geological and sedimentary features in the subsurface are hardly seen on $\Delta J/J$ and $\Delta(\lambda/\mu)/(\lambda/\mu)$ stacked sections. 2-D or 3-D seismic data would not make a lot of difference. Because the technique of AVO inversion is mostly employed in the reservoir level, the low resolution of the inverted attributes could cause a waste of time and money to a certain degree. To solve this problem, we could try to obtain the P-S seismic data with higher frequencies and wider bandwidth during the acquisition and processing. We could also try to extract some higher frequencies from P-P seismic data and compensate for the P-S data.

Another possible weakness of joint PP-PS AVO inversion is that the data preparation takes a lot of time, especially arranging the limited-offset bins for creating limited-offset stacked section. This could be improved by providing the offset ranges of the zone of interest in P-P and P-S data in the joint inversion module and having the module create limited-offset bins and limited-offset stacked sections according to the geometry information in the database. So far, I think these are the major obstacles affecting the greater use of this technology and ways to remove them. The most important thing of all is that somebody or some company has to give this technology a chance to be tested in industry and on more field data.

To lower the cost, joint inversion and P-wave-only inversion do not have to be both run. According to the inversion carried out on the Pikes Peak data where part of the seismic line is dominated by the coherent noise and part is not, joint inversion provides better results than P-wave-only inversion in both parts.

5.2 New achievement of this thesis

The joint PP-PS AVO inversion and P-wave-only inversion were carried out on a 2-D dataset for the first time and the data preparation procedure was generated for inverting the 2-D dataset. Despite the fact that the P-S data is heavily affected by coherent noise (pump-jack noise), the joint inversion works well and it is more effective than P-wave-only inversion. Another feature of this inversion project is that the zone of interest is as shallow as around 500 m underneath the surface. It is difficult to have very accurate velocity analysis from the very shallow part of seismic data. Velocities derived from seismic and well logs were tested. Using the velocities from well logs in the time-depth conversion and inversion provided better results.

Both joint inversion and P-wave-only inversion were carried out within a range of depth that was from zero to about 600 m, instead of only around the zone of interest. The method of flattening a certain horizon around the zone of interest to correlate the seismic events within a small depth range was compared to the method of not flattening any horizons and correlating the events in a larger range of depth. It is noticed that when the geological structure is relatively simple, the latter works fine. It is also the result of relative shifts in depth being allowed between P-P and P-S seismic data.

5.3 Future Work and discussion

The dipole well from which the interval compressional and shear velocities were extracted and used in the course of data preparation and joint inversion was logged in 1999, which is quite close to the time when the seismic data were acquired. And because this dipole well is far away from the closest steam injection well, it is not really affected by the steam. It is also the well that was used in the part of the zone of interest where the steam injection had been proceeding for an extended period. So new dipole wells should be logged for better control on compressional and shear velocities in the steam-injected zone of interest. As a result, the cost of the data used in the simultaneous inversion will be increased. But once better well control is obtained, the accuracy of time-depth conversion and the estimate of attributes in the steam-injection zone should be improved.

The inversion accuracy with different levels of coherent noise (such as pump-jack noise) should be tested. The statics correction should be carried out more thoroughly over the area where it is seriously affected by the coherent noise. It would be helpful if the pump-jack for the steam injection had been turned off while the seismic data were being acquired.

The joint P-P and P-S, three-parameter ($\Delta I/I$, $\Delta J/J$ and $\Delta\rho/\rho$) linearized inversion method should be tested and, potentially, the density should be inverted. Because three parameters would be available, the changes in the lithology and pore-fluid content could be more extensively described. P-P stand-alone inversion was carried out. So it is possible to carry out a P-S stand-alone inversion. Following the same logic of P-P stand-alone inversion, P-S stand-alone inversion would simply examine the case of a P-S reflection and extract the lithology and pore-fluid parameters from P-S seismic data only. In this case, all the P-P weights should be set to zero. But the P-S weights for P-S stand-alone inversion should be different from those for the joint PP-PS inversion. If the frequencies of P-S seismic data are much lower than those of P-P data, $\Delta I/I$ and $\Delta(\lambda\rho)/\lambda\rho$ resulting from P-S stand-alone inversion could be less coherent and of much lower frequencies than the estimates from the joint inversion because of the lack of P-P data in the inversion. However, the estimates of $\Delta J/J$ and $\Delta(\lambda/\mu)/(\lambda/\mu)$ resulting from P-S stand-alone inversion might be quite similar to those from the joint inversion. Consequently, when the frequencies of P-S seismic data are very low, instead of executing the joint inversion or P-P stand-alone inversion, P-S stand-alone inversion could be just enough for estimating $\Delta J/J$ and $\Delta(\lambda/\mu)/(\lambda/\mu)$.

Right now, there is no precise quality control for matching the events on P-P and P-S seismic section in depth. A possible way to gain better control on the event matching is to carry out a cross-correlation between the seismic section and a pseudo-section created according to the formation tops in the well logs. Other events could be interpolated and projected onto the pseudo-section. The horizons on the pseudo-section could then be regarded as references.

REFERENCES

Aki, K., and Richards, P.G., 2002, Quantitative seismology: Theory and Methods: W.H. Freeman and Company, **1**.

Brown, R.J., Stewart, R.R., and Lawton, D.C., 2002, A proposed polarity standard for multicomponent seismic data: Geophysics, **67**, 1028-1037.

Castagna, J. P., and Backus, M. M., 1993, AVO analysis-tutorial and review: Offset-dependent reflectivity-theory and practice of AVO analysis, 3-37.

Chiburis, E. F., 1984, Analysis of amplitude versus offset to detect gas-oil contacts in Arabia Gulf: 54th Ann. Internat. Mtg., Soc. Expl. Geophys., Expanded Abstracts, 669-670.

de Haas, J.C., and Berkhout, A.J., 1989, Practical approach to nonlinear inversion of amplitude versus offset information: 59th Annual Internat. Mtg., Soc. Expl. Geophys., Expanded Abstracts, **2**, 839.

Domenico, S.N., 1977, Elastic Properties of unconsolidated porous sand reservoirs: Geophysics, **42**, 1339-1369.

Fatti, J.L., Smith, G.C., Vail, P. J., Strauss, P. J., and Levitt, P. R., 1994, Detection of gas in sandstone reservoirs using AVO analysis: a 3-D seismic case history using the Geostack technique: Geophysics, **59**, 1362-1376.

Ferguson, R.J., 1996, P-S Seismic Inversion: Modeling, Processing, and Field Examples: M.Sc. Thesis, University of Calgary.

Ferre, A., Fournier, F., and Lucel, N., 1999, Improving AVO attributes with robust regression and quality control: 69th Ann. Internat. Mtg., Soc. Expl. Geophys., Expanded Abstracts, **1**, 848-851.

Gardner, G.H.F., Gardner, L.W., and Gregory, A. R., 1974, Formation velocity and density: The diagnostic basis for stratigraphic traps: Geophysics, **39**, 770-780.

Goodway, B., Chen, T., and Downton, J., 1997, Improved AVO fluid detection and lithology discrimination using Lame petrophysical parameters: "$\lambda\rho$", "$\mu\rho$" and "$\lambda\mu$ fluid stack", from P and S inversions: CSEG Expanded Abstracts, 148-151.

Gray, S. H., 1997, True-amplitude seismic migration: A comparison of three approaches: Geophysics, **62**, 929-936.

Hampson, D., and Russell, B., 1990, AVO inversion: theory and practice: 60th Annual Internat. Mtg., Soc. Expl. Geophys., Expanded Abstracts, **2**, 1456-1458.

Henley, D.C., Margrave, G.F., and Zhang, H., 2002, Preparing input data for joint PP/PS inversion: CREWES Research Report, **14**, no. 53.

Hilterman, F., 1989, Is AVO the seismic signature of rock properties?: 59th Ann. Internat. Mtg., Soc. Expl. Geophys., Expanded Abstracts, **1**, 559.

Koefoed, O., 1955, On the effect of Poisson'sratios of rock strata on the reflection coefficients of plane waves: Geophys. Prosp., **3**, 381-387.

Krajewski, P., Krajewski, C., and Grummt, S., 1993, True-amplitude processing of P- and PS- (converted) -wave data for AVO-analysis: 55th, Mtg. Eur. Assoc. Expl. Geophys., Abstracts, Session: C013.

Larsen, J.A., Margrave, G.F., Lu, H., and Potter, C.C., 1998, Simultaneous P-P and P-S inversion by weighted stacking applied to the Blackfoot 3C-3D survey: The CREWES Project Research Report, **10**, 50, 1-23.

Larsen, J.A., 1999, AVO inversion by simultaneous P-P and P-S inversion: M.Sc. Thesis, University of Calgary.

Lawton, D.C., and Howell, T.C., 1992, P-P and P-SV synthetic stacks, Expanded Abstract, 62nd SEG Ann. Internat. Mtg., 1344-1347.

Leckie, D.A., Bhattacharaya, J.P., Bloch, J., Gilboy, C.F., and Norris, B., 1994, Cretaceous Colorado/Alberta Group of the Western Canadian Sedimentary Basin. In: Geological Atlas of the Western Canadian Sedimentary Basin. G.D. Mossop and I. Shetsen (Comps.). Calgary, Canadian Society of Petroleum Geologists and Alberta Research Council, 335-352.

Lindseth, R.O., 1979, Synthetic sonic logs – A process for stratigraphic interpretation: Geophysics, **44**, 3-26.

Lynch, F.C.C., 1939, Fort Pitt Sheet (73F West Half): Geological Survey of Canada Map 490A, scale 1: 253,440, 1 sheet.

Macdonald, C., Davis, P.M., and Jackson, D. D., 1987, Inversion of reflection traveltimes and amplitudes: Geophysics, **52**, 606-617.

Margrave, G.F., and Foltinek, D.F., 1995, Synthetic P-P and P-SV cross sections: The CREWES Project Research Report, **7**, Ch. 5.

Margrave, G.F., Lawton, D.C., and Stewart, R.R., 1998, Interpreting channel sands with 3C-3D seismic data: The Leading Edge, **17**, 509-513.

Margrave, G.F., Stewart, R.R., and Larsen, J.A., 2001, Joint PP and PS seismic inversion: The Leading Edge, **20**, 1048-1052.

Orr, R.D., Johnston, J.R., and Manko, E.M., 1977, Lower Cretaceous geology and heavy-oil potential of the Lloydminster area: Bulletin of Canadian Petroleum Geology, **25**, 1187-1221.

Ostrander, W.J., 1982, Plane wave reflection coefficients for gas sands at non-normal angles of incidence: 52nd Annual Internat. Mtg., Soc. Expl. Geophys., Expanded Abstracts, 216-218.

Ostrander, W.J., 1984, Plane-wave reflection coefficients for gas sands at non-normal angles of incidence: Geophysics, **49**, 1637-1648.

Pickett, G.R., 1963, Acoustic character logs and their application in formation evaluation: J. Petr. Tech., **15**, 650-667.

Ricker, N. and Lynn, R.D., 1950, Composite reflections: Geophysics, **15**, 30-49.

Ramos, A.C.B., Oliveira, A.S., and Tygel, M., 1999, the impact of true amplitude DMO on amplitude versus offset: 69th Ann. Internat. Mtg., Soc. Expl. Geophys., Expanded Abstracts, **1**, 832-835.

Russell, B.H., 1988, Introduction to seismic inversion methods: SEG Continuing Education Course Note Series, **2**, Soc. Expl. Geophys.

Rutherford, S.R., and Williams, R.H., 1989, Amplitude-versus-offset variations in gas sands: Geophysics, **54**, 680-688.

Schneider, J., and Krey, T., 1985, True amplitude migration using summation method: Some examples and practical aspects: 55th Annual Internat. Mtg., Soc. Expl. Geophys., Expanded Abstracts, 419-421.

Sheriff, R.E., 1991, Encyclopedic dictionary of exploration geophysics, Soc. Expl. Geophys.

Shuey, R.T., 1985, A simplification of the Zoeppritz equations: Geophysics, **50**, 609-614.

Smith, G.C., and Gidlow, P.M., 1987, Weighted stacking for rock property estimation and detection of gas: Geophys. Prosp., **35**, 993-1014.

Stewart, R.R., 1990, Joint P and P-SV inversion: The CREWES Project Research Report, **2**, 112-115.

Stewart, R.R., Zhang, Q., and Guthoff, F., 1995, Relationships among elastic-wave values: R_{PP}, R_{PS}, R_{SS}, V_P, V_S, κ, σ and ρ: The CREWES Project Research Report, **7**, 10, 1-9.

Stewart, R.R., and Lawton, D.C., 1996, P-S seismic exploration: A mid-term overview: The CREWES Project Research Report, **8,** 1.

Tessmer, G. and Behle, A., 1988, Common reflection point data-stacking technique for converted waves: Geophys. Prosp., **36**, 671-688.

Thomsen, L., 1990, Poisson was not a geophysicist: The Leading Edge, December 1990, **9**, 27-29.

Van Hulten, F.F.N., 1984, Petroleum geology of Pikes Peak heavy oil field, Waseca Formation, Lower Cretaceous, Saskatchewan, Canadian Society of Petroleum Geologists, Memoir 9, 441-454.

Van Rijssen, E.P.F., and Herman, G.C., 1991, Resolution analysis of band-limited and offset-limited seismic data for plane-layered subsurface models: Geophys. Prop., Eur. Assn. Geosci. Eng., **39**, 61-76.

Waters, K.H., 1992, Reflection Seismology: A tool for energy resource exploration: New York:Wiley.

Watson, I.A., Brittle, K.F., and Lines, L.R., 2001, Heavy-oil reservoir characterization using elastic wave properties: The CREWES Project Research Report, **13**, 777-784.

Wright, J., 1986, Reflection coefficients at pore-fluid contacts as a function of offset (short note): Geophysics, **51**, 1858-1860.

Zoeppritz, K., 1919, Erdbebenwellen VIIIB, On the reflection and propagation of seismic waves: Göttinger Nachrichten, I, 66-84.